Measurements of the neutron electric to magnetic form factor ratio G_{En}/G_{Mn} via the $^2\mathrm{H}(\vec{e}, e'\vec{n})^1\mathrm{H}$ reaction to $Q^2 = 1.45$ (GeV/c)^2

B. Plaster,[1,2,*] A. Yu. Semenov,[3,4,†] A. Aghalaryan,[5] E. Crouse,[6] G. MacLachlan,[7] S. Tajima,[8] W. Tireman,[3,9] A. Ahmidouch,[10] B. D. Anderson,[3] H. Arenhövel,[11] R. Asaturyan,[5] O. K. Baker,[12] A. R. Baldwin,[3] D. Barkhuff,[1,‡] H. Breuer,[13] R. Carlini,[14] E. Christy,[12] S. Churchwell,[8,§] L. Cole,[12] S. Danagoulian,[10,14] D. Day,[15] T. Eden,[3,12,‖] M. Elaasar,[16] R. Ent,[14] M. Farkhondeh,[1] H. Fenker,[14] J. M. Finn,[6] L. Gan,[12] A. Gasparian,[10,12] K. Garrow,[14] P. Gueye,[12] C. R. Howell,[8] B. Hu,[12] M. K. Jones,[14] J. J. Kelly,[13] C. Keppel,[12] M. Khandaker,[17] W.-Y. Kim,[18] S. Kowalski,[1] A. Lung,[14] D. Mack,[14] R. Madey,[3,6,14] D. M. Manley,[3] P. Markowitz,[19] J. Mitchell,[14] H. Mkrtchyan,[5] A. K. Opper,[7] C. Perdrisat,[6] V. Punjabi,[17] B. Raue,[19] T. Reichelt,[20] J. Reinhold,[19] J. Roche,[6] Y. Sato,[12] N. Savvinov,[13] I. A. Semenova,[3,4] W. Seo,[18] N. Simicevic,[21] G. Smith,[14] S. Stepanyan,[5] V. Tadevosyan,[5] L. Tang,[12] S. Taylor,[1] P. E. Ulmer,[22] W. Vulcan,[14] J. W. Watson,[3] S. Wells,[21] F. Wesselmann,[15] S. Wood,[14] Chen Yan,[14] Chenyu Yan,[3] S. Yang,[18] L. Yuan,[12] W.-M. Zhang,[3] H. Zhu,[15] and X. Zhu[12]

(Jefferson Laboratory E93-038 Collaboration)

[1]*Massachusetts Institute of Technology, Cambridge, Massachusetts 02139, USA*
[2]*California Institute of Technology, Pasadena, California 91125, USA*
[3]*Kent State University, Kent, Ohio 44242, USA*
[4]*Joint Institute for Nuclear Research, Dubna RU-141980, Russia*
[5]*Yerevan Physics Institute, Yerevan 375036, Armenia*
[6]*The College of William and Mary, Williamsburg, Virginia 23187, USA*
[7]*Ohio University, Athens, Ohio 45701, USA*
[8]*Duke University and TUNL, Durham, North Carolina 27708, USA*
[9]*Northern Michigan University, Marquette, Michigan 49855, USA*
[10]*North Carolina A&T State University, Greensboro, North Carolina 27411, USA*
[11]*Johannes Gutenberg-Universität, D-55099 Mainz, Germany*
[12]*Hampton University, Hampton, Virginia 23668, USA*
[13]*University of Maryland, College Park, Maryland 20742, USA*
[14]*Thomas Jefferson National Accelerator Facility, Newport News, Virginia 23606, USA*
[15]*University of Virginia, Charlottesville, Virginia 22904, USA*
[16]*Southern University at New Orleans, New Orleans, Louisiana 70126, USA*
[17]*Norfolk State University, Norfolk, Virginia 23504, USA*
[18]*Kyungpook National University, Taegu 702-701, Korea*
[19]*Florida International University, Miami, Florida 33199, USA*
[20]*Rheinische Friedrich-Wilhelms-Universität, D-53115 Bonn, Germany*
[21]*Louisiana Tech University, Ruston, Louisiana 71272, USA*
[22]*Old Dominion University, Norfolk, Virginia 23508, USA*

(Received 13 November 2005; published 27 February 2006)

We report values for the neutron electric to magnetic form factor ratio, G_{En}/G_{Mn}, deduced from measurements of the neutron's recoil polarization in the quasielastic $^2\mathrm{H}(\vec{e}, e'\vec{n})^1\mathrm{H}$ reaction, at three Q^2 values of 0.45, 1.13, and 1.45 (GeV/c)^2. The data at $Q^2 = 1.13$ and 1.45 (GeV/c)^2 are the first direct experimental measurements of G_{En} employing polarization degrees of freedom in the $Q^2 > 1$ (GeV/c)^2 region and stand as the most precise determinations of G_{En} for all values of Q^2.

DOI: 10.1103/PhysRevC.73.025205 PACS number(s): 14.20.Dh, 13.40.Gp, 25.30.Bf, 24.70.+s

I. INTRODUCTION

The nucleon electromagnetic form factors are fundamental quantities needed for an understanding of the nucleon's electromagnetic structure. The Sachs electric, G_E, and magnetic, G_M, form factors [1], defined in terms of linear combinations of the Dirac and Pauli form factors, are of particular physical interest, as their evolution with Q^2, the square of the four-momentum transfer, is related to the spatial distribution of charge and current within the nucleon. As such, precise measurements of these form factors over a wide range of Q^2 are needed for a quantitative understanding of the electromagnetic structure not only of the nucleon but also of nuclei (e.g., Refs. [2–4]). Further, in the low-energy regime of the nucleon ground state, the underlying theory of the strong interaction, quantum chromodynamics (QCD), cannot be solved perturbatively. A proper description of even the static properties of the nucleon, the lowest stable mass excitation of

*Electronic address: plaster@caltech.edu
†Electronic address: semenov@jlab.org
‡Now at Renaissance Technologies, East Setauket, New York 11733, USA.
§Now at University of Canterbury, Christchurch 8020, New Zealand.
‖Now at National Center for Atmospheric Research, Boulder, Colorado 80307, USA.

the QCD vacuum, in terms of the QCD quark and gluon degrees of freedom still stands as one of the outstanding challenges of hadronic physics. Indeed, one of the most stringent tests to which nonperturbative QCD (as formulated on the lattice or in a model of confinement) can be subjected is the requirement that the theory reproduce experimental data on the nucleon form factors (e.g., Refs. [5–7]).

Because of the lack of a free neutron target, the neutron form factors are known with less precision than are the proton form factors, and measurements have been restricted to smaller ranges of Q^2. A precise measurement of the neutron electric form factor, G_{En}, has proven to be especially elusive as the neutron's net charge is zero. Prior to the realization of experimental techniques utilizing polarization degrees of freedom, values for G_{En} were extracted from measurements of the unpolarized quasielastic $^2\mathrm{H}(e, e'n)^1\mathrm{H}$ cross section and the deuteron elastic structure function $A(Q^2)$. Those results for G_{En} deduced from measurements of the quasielastic $^2\mathrm{H}(e, e'n)^1\mathrm{H}$ cross section provided little information on G_{En}, as all results were consistent with zero over all ranges of Q^2 accessed, $0 < Q^2 < 4$ $(\mathrm{GeV}/c)^2$ (e.g., Ref. [8]). Similarly, results for G_{En} deduced from measurements of $A(Q^2)$, although establishing $G_{En} > 0$ for $0 < Q^2 < 0.7$ $(\mathrm{GeV}/c)^2$, were plagued with large theoretical uncertainties ($\sim\pm 40\%$) related to the choice of an appropriate *NN*-potential for the deuteron wave function (e.g., Ref. [9]).

With the advent of high duty-factor polarized electron beam facilities and state-of-the-art polarized nuclear targets and recoil nucleon polarimeters, experimental efforts over the past 15 years have now yielded the first precise determinations of G_{En}. In addition, recent theoretical efforts [10] have permitted an extraction of G_{En} from existing data on the deuteron quadrupole form factor with small theoretical uncertainties. Our experiment [11] was designed to extract the neutron electric to magnetic form factor ratio, G_{En}/G_{Mn}, from measurements of the neutron's recoil polarization in quasielastic $^2\mathrm{H}(\vec{e}, e'\vec{n})^1\mathrm{H}$ kinematics at three Q^2 values of 0.45, 1.13, and 1.45 $(\mathrm{GeV}/c)^2$. These results were published rapidly by Madey *et al.* [12]; here we provide a more detailed report of the experiment and analysis procedures.

The remainder of this article is organized as follows. We begin, in Sec. II, with a brief overview of the experimental techniques utilizing polarization degrees of freedom that have been employed for measurements of the neutron form factors. We continue with an overview of our experiment in Sec. III and then discuss our neutron polarimeter in Sec. IV. Details of the analysis procedure are discussed in Sec. V. Our final results are then presented in Sec. VI and compared with selected theoretical model calculations of the nucleon form factors. Finally, we conclude with a brief summary in Sec. VII. A more detailed account of the discussion that follows may be found in Ref. [13].

II. NEUTRON FORM FACTORS

A. Electron kinematics

We will use the following notation for the electron kinematics: $(E_e, \mathbf{p}_e)$ will denote the four-momentum of the initial electron, $(E_{e'}, \mathbf{p}_{e'})$ will denote the four-momentum of the scattered electron, $\theta_{e'}$ will denote the electron scattering angle, $\omega = E_e - E_{e'}$ will denote the energy transfer, $\mathbf{q} = \mathbf{p}_e - \mathbf{p}_{e'}$ will denote the three-momentum transfer, and $Q^2 = \mathbf{q}^2 - \omega^2 = 4E_eE_{e'}\sin^2(\theta_{e'}/2)$ will denote the square of the spacelike four-momentum transfer in the high-energy limit of massless electrons. The electron scattering plane is defined by $\mathbf{p}_e$ and $\mathbf{p}_{e'}$.

B. Measurements via polarized electron beams and recoil nucleon polarimetry

1. *Elastic $N(\vec{e}, e'\vec{N})$ scattering*

The polarization of the recoil nucleon, $\mathbf{P}$, in elastic polarized-electron, unpolarized-nucleon scattering is well-known to be of the form [14–17]

$$\frac{d\sigma}{d\Omega_{e'}}(\mathbf{P}) = \sigma_0(\mathbf{P}^{(0)} + h\mathbf{P}^{(h)}), \tag{1}$$

where σ_0 denotes the unpolarized cross section, $\mathbf{P}^{(0)}$ denotes the helicity-independent recoil polarization, $\mathbf{P}^{(h)}$ denotes the helicity-dependent recoil polarization, and $h = \pm 1$ denotes the electron helicity. The polarization is customarily projected onto a $(\hat{t}, \hat{n}, \hat{\ell})$ unit vector basis, with the longitudinal component, $\hat{\ell}$, along the recoil nucleon's momentum; the normal component, $\hat{n}$, perpendicular to the electron scattering plane; and the transverse component, $\hat{t}$, perpendicular to the $\hat{\ell}$ component in the scattering plane. In the one-photon exchange approximation, $\mathbf{P}^{(0)} = \mathbf{0}$, and $\mathbf{P}^{(h)}$ is confined to the scattering plane (i.e., $P_n^{(h)} = 0$). The transverse, $P_t^{(h)}$, and longitudinal, $P_\ell^{(h)}$, components are expressed in terms of kinematics and nucleon form factors as [14–17]

$$P_t^{(h)} = P_e \frac{-2G_EG_M\sqrt{\tau(1+\tau)}\tan\frac{\theta_{e'}}{2}}{G_E^2 + \left[\tau + 2\tau(1+\tau)\tan^2\frac{\theta_{e'}}{2}\right]G_M^2}, \tag{2a}$$

$$P_\ell^{(h)} = P_e \frac{2G_M^2\tau\sqrt{(1+\tau) + (1+\tau)^2\tan^2\frac{\theta_{e'}}{2}}\tan\frac{\theta_{e'}}{2}}{G_E^2 + \left[\tau + 2\tau(1+\tau)\tan^2\frac{\theta_{e'}}{2}\right]G_M^2}, \tag{2b}$$

where P_e denotes the electron beam polarization, $\tau = Q^2/4m^2$, and m denotes the nucleon mass.

Access to both $P_t^{(h)} \propto G_EG_M$ and $P_\ell^{(h)} \propto G_M^2$ via a secondary analyzing reaction in a polarimeter is highly advantageous, as the analyzing power of the polarimeter, denoted A_y, and P_e cancel in the $P_t^{(h)}/P_\ell^{(h)}$ ratio, yielding a measurement of G_E/G_M that is relatively insensitive to systematic uncertainties associated with these quantities. For the case of the neutron form factor ratio, as suggested by Arnold, Carlson, and Gross [17] and first implemented experimentally by Ostrick *et al.* [18], a vertical dipole field located ahead of a polarimeter configured to measure an up-down scattering asymmetry sensitive to the projection of the recoil polarization on the $\hat{t}$-axis permits access to both $P_t^{(h)}$ and $P_\ell^{(h)}$. During transport through the magnetic field, the recoil polarization vector will precess through some spin precession angle χ in the $\hat{t}$-$\hat{\ell}$ plane, leading to a scattering asymmetry, $\xi(\chi)$, which is sensitive to a mixing of $P_t^{(h)}$ and $P_\ell^{(h)}$,

$$\begin{aligned}\xi(\chi) &= A_y\left(P_t^{(h)}\cos\chi + P_\ell^{(h)}\sin\chi\right)\\ &= A_y|\mathbf{P}^{(h)}|\sin(\chi+\delta).\end{aligned} \tag{3}$$

In the above, $|\mathbf{P}^{(h)}| = [(P_t^{(h)})^2 + (P_\ell^{(h)})^2]^{1/2}$, and we define the phase-shift parameter δ according to

$$\tan\delta = \frac{P_t^{(h)}}{P_\ell^{(h)}} = -\frac{G_E}{G_M}\frac{\cos\dfrac{\theta_{e'}}{2}}{\sqrt{\tau+\tau^2\sin^2\dfrac{\theta_{e'}}{2}}}. \quad (4)$$

2. *Quasielastic* ^{2}H$(\vec{e}, e'\vec{n})^1$H *scattering*

The above formalism is directly applicable to an extraction of the proton form factor ratio, G_{Ep}/G_{Mp}, from measurements of the proton's recoil polarization in elastic $^1\vec{\mathrm{H}}(\vec{e}, e'\vec{p})$ scattering. An extraction of the neutron form factor ratio, G_{En}/G_{Mn}, from measurements of the neutron's recoil polarization in quasielastic ^{2}H$(\vec{e}, e'\vec{n})^1$H scattering is, however, complicated by nuclear physics effects, such as final-state interactions (FSI), meson exchange currents (MEC), isobar configurations (IC), and the structure of the deuteron. The pioneering study of the sensitivity of the quasielastic ^{2}H$(\vec{e}, e'\vec{n})^1$H reaction to the neutron form factors, reported by Arenhövel [19], revealed that for perfect quasifree emission of the neutron (i.e., neutron emission along the three-momentum transfer $\mathbf{q}$), $P_t^{(h)}$ is proportional to G_{En}, but is relatively insensitive to FSI, MEC, IC, and the choice of the *NN* potential for the deuteron wave function. A more detailed study of the ^{2}H$(\vec{e}, e'\vec{n})^1$H reaction reported by Arenhövel, Leidemann, and Tomusiak [20] found that these results also apply to $P_\ell^{(h)}$. Similar findings were subsequently reported by Refs. [21,22].

These theoretical investigations [20,22] indicated that in quasifree kinematics the influence of these nuclear physics effects on the neutron's recoil polarization are sizable for Q^2 values below 0.2 $(\mathrm{GeV}/c)^2$, but become small for $Q^2 \gtrsim 0.3\,(\mathrm{GeV}/c)^2$ and decrease with increasing Q^2. Indeed, in one recent ^{2}H$(\vec{e}, e'\vec{n})^1$H experiment [18,23], the corrections for FSI resulted in a 65 and 8% increase to the value of G_{En} at $Q^2 = 0.15$ and 0.34 $(\mathrm{GeV}/c)^2$, respectively. As will be seen later, the corrections for nuclear physics effects at our three Q^2 points were on the order of a few percentages and decreased with each increment in Q^2.

In Appendix A, we present a detailed discussion of the formalism for the kinematics and recoil polarization observables for the quasielastic ^{2}H$(\vec{e}, e'\vec{n})^1$H reaction. In particular, we provide there a definition for $\Theta_{np}^{\mathrm{c.m.}}$, the polar angle between the proton momentum and $\mathbf{q}$ in the recoiling neutron-proton center-of-mass frame (hereafter, n-p c.m. frame), a variable to which we refer frequently throughout this article. (Perfect quasifree emission of the neutron is defined by $\Theta_{np}^{\mathrm{c.m.}} = 180^\circ$.) We follow this, in Appendix B, with a discussion of the sensitivity of the recoil polarization components to FSI, MEC, IC, and the choice of the *NN* potential for the deuteron wave function at and away from perfect quasifree emission.

C. Measurements via polarized electron beams and polarized targets

1. *Elastic* $\vec{N}(\vec{e}, e'N)$ *scattering*

The cross section in the one-photon exchange approximation for elastic polarized-electron, polarized-nucleon scattering is well known to be of the form [14–16,24]

$$\frac{d\sigma}{d\Omega_{e'}} = \sigma_0[1 + hA_{eN}(\theta^*, \phi^*)]. \quad (5)$$

Here, θ^* and ϕ^* denote, respectively, the polar and azimuthal angle between the target nucleon polarization vector and $\mathbf{q}$, and $A_{eN}(\theta^*, \phi^*)$ denotes the polarized-electron, polarized-nucleon beam-target asymmetry, which is a function of kinematics and the nucleon form factors. The sensitivity of A_{eN} to the form factors is enhanced if the target polarization is oriented in the electron scattering plane either parallel or perpendicular to $\mathbf{q}$; in the former (latter) case, the expression for A_{eN} is identical to that for $-P_\ell^{(h)}$ ($P_t^{(h)}$) and will be denoted $A_\parallel$ ($A_\perp$). Similar to the recoil polarization technique, measurements of both $A_\perp$ and $A_\parallel$ are desirable as the target polarization (analog to the analyzing power) and beam polarization cancel in the $A_\perp/A_\parallel$ ratio, again yielding a measurement of G_E/G_M that is relatively free of systematic uncertainties.

2. *Quasielastic* $^2\vec{\mathrm{H}}(\vec{e}, e'n)^1$H *and* $^3\vec{\mathrm{He}}(\vec{e}, e'n)$ *scattering*

The above formalism is directly applicable to a measurement of G_{Ep}/G_{Mp} via the elastic $^1\vec{\mathrm{H}}(\vec{e}, e'p)$ reaction, but an extraction of G_{En}/G_{Mn} from either the quasielastic $^2\vec{\mathrm{H}}(\vec{e}, e'n)^1$H reaction or the quasielastic $^3\vec{\mathrm{He}}(\vec{e}, e'n)$ reaction is again complicated by nuclear physics effects. For the case of the $^2\vec{\mathrm{H}}(\vec{e}, e'n)^1$H reaction, Cheung and Woloshyn [25] were the first to show that the polarized-electron, vector-polarized-deuterium beam-target asymmetry, A_{ed}^V, is sensitive to G_{En}. More complete calculations of A_{ed}^V that accounted for nuclear physics effects were later reported by Tomusiak and Arenhövel [26] and others [20,22,27,28]. These calculations demonstrated that for quasifree neutron kinematics, A_{ed}^V is strongly sensitive to G_{En} but is relatively insensitive to FSI, MEC, IC, and the choice of the *NN* potential for the deuteron wave function.

For the case of quasielastic scattering from polarized ^{3}He, Blankleider and Woloshyn [29] were the first to study the sensitivity of the inclusive $^3\vec{\mathrm{He}}(\vec{e}, e')$ asymmetry to G_{En}. More detailed studies of the inclusive asymmetry carried out by others [30,31] suggested that a clean extraction of G_{En} from the inclusive asymmetry would be extremely difficult because of proton contamination of the inclusive asymmetry. Such difficulties for an extraction of G_{En} are, however, mitigated in a $^3\vec{\mathrm{He}}(\vec{e}, e'n)$ coincidence experiment; as further motivation, Laget [22] demonstrated that the exclusive $^3\vec{\mathrm{He}}(\vec{e}, e'n)$ asymmetry is relatively insensitive to the effects of FSI and MEC for $Q^2 \gtrsim 0.3\ (\mathrm{GeV}/c)^2$.

D. Analysis of the deuteron quadrupole form factor

The unpolarized elastic electron-deuteron cross section is generally expressed in terms of the elastic structure functions, $A(Q^2)$ and $B(Q^2)$. These are, in turn, functions of the deuteron's charge, G_C, quadrupole, G_Q, and magnetic, G_M, form factors. G_C and G_Q are of particular interest for an extraction of G_{En} as they are both proportional to $(G_{Ep} + G_{En})$.

An unambiguous extraction of G_C, G_Q, and G_M from a Rosenbluth separation of $A(Q^2)$ and $B(Q^2)$ requires some

TABLE I. Chronological summary of published data on the neutron form factors from experiments employing polarization degrees of freedom and a recent analysis combining data on the deuteron quadrupole form factor, G_Q, with data on t_{20} and T_{20}.

Reference	Facility	Published	Type	Q^2 [(GeV/c)^2]	Quantities	Note(s)
Jones-Woodward *et al.* [32]	MIT-Bates	1991	$^3\vec{\mathrm{He}}(\vec{e}, e')$	0.16	$A_\perp \rightarrow G_{En}$	a,b
Thompson *et al.* [33]	MIT-Bates	1992	$^3\vec{\mathrm{He}}(\vec{e}, e')$	0.2	$A_\perp, A_\parallel \rightarrow G_{En}$	a,b
Eden *et al.* [34]	MIT-Bates	1994	$^2\mathrm{H}(\vec{e}, e'\vec{n})$	0.255	$P_t^{(h)} \rightarrow G_{En}$	c,d
Gao *et al.* [36]	MIT-Bates	1994	$^3\vec{\mathrm{He}}(\vec{e}, e')$	0.19	$A_\parallel \rightarrow G_{Mn}$	a,e
Meyerhoff *et al.* [38]	MAMI	1994	$^3\vec{\mathrm{He}}(\vec{e}, e'n)$	0.31	$A_\perp, A_\parallel \rightarrow G_{En}$	a,b
Becker *et al.* [39]	MAMI	1999	$^3\vec{\mathrm{He}}(\vec{e}, e'n)$	0.40	$A_\perp, A_\parallel \rightarrow G_{En}$	b,f
Ostrick *et al.* [18], Herberg *et al.* [23]	MAMI	1999	$^2\mathrm{H}(\vec{e}, e'\vec{n})$	0.15, 0.34	$P_t^{(h)}, P_\ell^{(h)} \rightarrow G_{En}$	b,c
Passchier *et al.* [41]	NIKHEF	1999	$^2\vec{\mathrm{H}}(\vec{e}, e'n)$	0.21	$A_{ed}^V \rightarrow G_{En}$	b,c
Rohe *et al.* [42], Bermuth *et al.* [43]	MAMI	1999/2003	$^3\vec{\mathrm{He}}(\vec{e}, e'n)$	0.67	$A_\perp, A_\parallel \rightarrow G_{En}$	g,h
Xu *et al.* [46]	JLab	2000/2003	$^3\vec{\mathrm{He}}(\vec{e}, e')$	0.1–0.6	$A_\parallel \rightarrow G_{Mn}$	a,i
Schiavilla and Sick [10]	—	2001	Analysis	0.00–1.65	$G_Q \rightarrow G_{En}$	j
Zhu *et al.* [48]	JLab	2001	$^2\vec{\mathrm{H}}(\vec{e}, e'n)$	0.495	$A_{ed}^V \rightarrow G_{En}$	b,c
Madey *et al.* [12], this article	JLab	2003	$^2\mathrm{H}(\vec{e}, e'\vec{n})$	0.45, 1.13, 1.45	$P_t^{(h)}, P_\ell^{(h)} \rightarrow G_{En}$	c,k
Warren *et al.* [50]	JLab	2004	$^2\vec{\mathrm{H}}(\vec{e}, e'n)$	0.5, 1.0	$A_{ed}^V \rightarrow G_{En}$	c,g
Glazier *et al.* [51]	MAMI	2005	$^2\mathrm{H}(\vec{e}, e'\vec{n})$	0.30, 0.59, 0.79	$P_t^{(h)}, P_\ell^{(h)} \rightarrow G_{En}$	c,l

[a]Uncorrected for nuclear physics effects (i.e., for FSI, MEC, or IC).
[b]Used the dipole parametrization for G_{Mn}.
[c]Applied corrections for FSI, MEC, and IC by averaging calculations of Arenhövel *et al.* [19,20,26–28] over the acceptance.
[d]Used the value for G_{Mn} at $Q^2 = 0.255$ (GeV/c)^2 as measured by Markowitz *et al.* [35].
[e]Used the Galster parametrization [37] for G_{En}.
[f]Corrections for FSI and MEC calculated by Golak *et al.* [40].
[g]Used values for G_{Mn} taken from the parametrization of Kubon *et al.* [44].
[h]Estimated corrections for FSI by scaling calculations of Golak *et al.* [45] at $Q^2 = 0.37$ (GeV/c)^2 to $Q^2 = 0.67$ (GeV/c)^2.
[i]Used values for G_{En} taken from the parametrization of Höhler *et al.* [47].
[j]Theoretical analysis of data on the deuteron quadrupole form factor, G_Q, tensor moment, t_{20}, and tensor analyzing power, T_{20}.
[k]Used values for G_{Mn} taken from the parametrization of Kelly [49].
[l]Used values for G_{Mn} taken from the parametrization of Friedrich and Walcher [52].

third observable. The tensor moments, t_{2j} $(j = 0, 1, 2)$, extracted from recoil polarization measurements in elastic unpolarized-electron, unpolarized-deuteron scattering, and the tensor analyzing powers, T_{2j} $(j = 0, 1, 2)$, as measured in elastic unpolarized-electron, tensor polarized-deuteron scattering, are of particular interest as they are functions of G_C, G_Q, and G_M [17,24]. Indeed, after G_C, G_Q, and G_M have been separated from $A(Q^2)$, $B(Q^2)$, and the polarization-dependent observables, a value for G_{En} can be extracted from either G_C or G_Q; however, as was shown by Schiavilla and Sick [10], an extraction of G_{En} from data on G_Q is particularly advantageous as the contributions of theoretical uncertainties associated with short-range two-body exchange operators to G_Q are small.

E. Summary of results

In Table I, we have compiled a complete chronological summary of all published data on the neutron form factors from experiments employing polarization degrees of freedom and a recent analysis combining data on the deuteron quadrupole form factor with the polarization-dependent observables t_{20} and T_{20}. The current status of these results for G_{En} is shown in Fig. 1. We have omitted the results of Jones-Woodward *et al.* [32], Thompson *et al.* [33], and Meyerhoff *et al.* [38] from this plot as these results were not corrected for nuclear physics effects. It should be noted that the results of Herberg *et al.* [23] and Bermuth *et al.* [43] supersede those of Ostrick *et al.* [18] and Rohe *et al.* [42], respectively, as the former set reported the final results (corrected for nuclear physics effects) for their respective experiments.

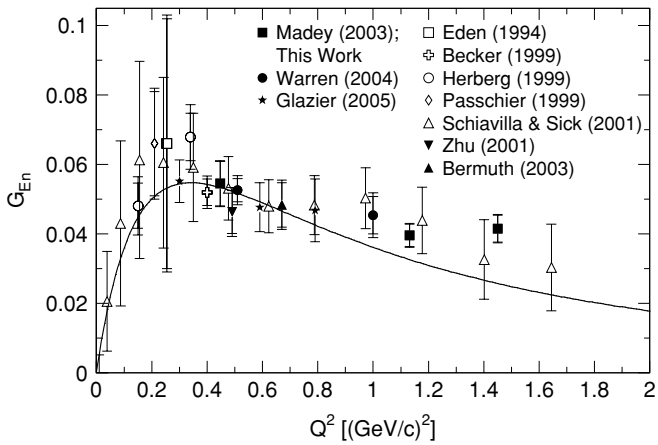

FIG. 1. Current status of results for G_{En} ([10,12,23,34,39,41,43, 48,50,51] and this work). The Galster parametrization [37] is shown as the solid curve. See Table I for the reaction types for the individual data points.

The Q^2 range of G_{En} is much more limited than those of the other three nucleon electromagnetic form factors, with only two results, those of Madey *et al*. [12] and the analysis results of Schiavilla and Sick [10], extending into the $Q^2 > 1$ (GeV/c)^2 region. The agreement between these modern data and the Galster parametrization [37] with its original fitted parameters can be judged only as fortuitous.

III. EXPERIMENT

A. Overview of experiment

Our experiment [11], E93-038, was conducted in Hall C of the Jefferson Laboratory (JLab) during a run period lasting from September 2000 to April 2001. Longitudinally polarized electrons extracted from the JLab electron accelerator [53] scattered from a liquid deuterium target mounted on the Hall C beamline. The scattered electrons were detected and momentum analyzed by the Hall C High Momentum Spectrometer (HMS) in coincidence with the recoil neutrons. A stand-alone neutron polarimeter (NPOL) [54], designed and installed in Hall C specifically for this experiment, was used to measure the up-down scattering asymmetry arising from the projection of the recoil neutrons' polarization on an axis perpendicular to their momentum and parallel to the floor of Hall C. A vertical dipole field located ahead of NPOL was used to precess the recoil neutrons' polarization vectors through some chosen spin precession angle to measure this up-down scattering asymmetry from different projections of the recoil polarization vector on the polarimeter's sensitive axis. This vertical dipole field also served as a sweeping field for the background flux of recoil protons from the deuteron target.

Data were taken at four central Q^2 values of 0.447, 1.136, 1.169, and 1.474 (GeV/c)^2 with associated electron beam energies of 0.884, 2.326, 2.415, and 3.395 GeV, respectively. The nominal (central) values of the quasielastic electron and neutron kinematics and the neutron spin precession angles, χ, for each of these central Q^2 points are summarized in Table II. We note that the data acquired at the separate central Q^2 values of 1.136 and 1.169 (GeV/c)^2 were combined in our final analysis. Beam polarizations of 70%–80% at currents of 20–70 μA were typical throughout the duration of the experiment. The central axis of the neutron polarimeter was fixed at a scattering angle of 46.0° relative to the incident electron beamline for the duration of the experiment. The scattering asymmetries measured in our polarimeter were on the order of a few percentages.

TABLE II. Nominal (central) values of the quasielastic electron and neutron kinematics and neutron spin precession angles for each Q^2 setting in the experiment. The data from the central Q^2 values of 1.136 and 1.169 (GeV/c)^2 were combined in our final analysis.

Q^2 [(GeV/c)^2]	E_e (GeV)	$E_{e'}$ (GeV)	$\theta_{e'}$	T_n (MeV)	Precession angles χ
0.447	0.884	0.643	52.65°	239	±40°
1.136	2.326	1.718	30.93°	606	0°, ±90°
1.169	2.415	1.789	30.15°	624	±40°
1.474	3.395	2.606	23.55°	786	0°, ±40°, ±90°

B. Polarized electron source

Polarized electrons were produced at the accelerator source via optical illumination of a strained GaAs photocathode (GaAs on GaAsP [55]) with circularly polarized laser light from a ∼500 mW Ti-sapphire laser [55,56]; the linearly polarized light from the laser was circularly polarized with a Pockels cell. The helicity of the circularly polarized light emerging from the Pockels cell was flipped at a frequency of 30 Hz (by switching the polarity of the high voltage applied to the Pockels cell) according to a pseudorandom scheme in which the helicity of one 33.3-ms window was randomly chosen, and the helicity of the following 33.3-ms window required to be that of the opposite helicity (i.e., a sequence of such "helicity pairs" could have been $+-$, $-+$, $-+$, $+-$, etc.). A $\lambda/2$ plate was intermittently placed in the optics path upstream of the Pockels cell. This $\lambda/2$ plate reversed the helicity of the electron beam that would otherwise have been induced by the Pockels cell, thereby providing the means for important systematic checks of any possible helicity-correlated differences.

C. Hall C beamline

Beam of the desired energy was extracted from the accelerator and then transported along the Hall C arc (series of steering/bending magnets) and beamline. A number of superharps [57] were used to monitor the beam profile, and four beam position monitors (cavities with four antennas oriented at angles of ±45° relative to the horizontal and vertical directions) provided absolute determinations of the beam position. The beam current was monitored with two monitors (cylindrical wave guides with wire loop antennas coupling to resonant modes of the beam cavity, yielding signals proportional to the current).

D. Beam polarization measurements

The beam polarization was measured periodically with a Møller polarimeter [58] located along the Hall C beamline approximately 30 m upstream of the cryotarget. We measured the beam polarization approximately every 1 to 2 days during stable accelerator operations. Measurements were also typically conducted following the insertion or removal of the $\lambda/2$ plate at the polarized source or other major accelerator changes. A statistical precision of <1% was typically achieved after ∼15–20 min of data taking. Details of the results of our beam polarization measurements are discussed later, where it will be seen that the details of the analysis are relatively insensitive to the exact values of the beam polarization. Instead, the beam polarization information was primarily used to assess systematic uncertainties associated with temporal fluctuations in the polarization.

It should be noted that although our production scattering asymmetry data were taken with beam currents as high as 70 μA, the Møller polarimeter was designed only for currents up to ∼8 μA (because of the heating and subsequent depolarization of the iron target foil); therefore, it was necessary to assume that our beam polarization measurements conducted at currents of 1–2 μA were valid for the higher beam currents

of our production running. The validity of this assumption has been verified for operations in Hall A at JLab where the results from beam polarization measurements conducted at low currents (Møller polarimeter) and high currents (Compton polarimeter) were found to agree to ∼3% [59].

E. Scattering chamber and cryotargets

The scattering chamber consisted of a vertically standing cylindrical aluminum chamber vacuum coupled to the incoming beamline. Two exit windows (made of beryllium) faced the HMS and NPOL, whereas an exit port faced the downstream beamline leading to the beam dump. During our experiment, the scattering chamber housed only one target ladder divided into a cryogenic target section and a solid target section. The cryogenic target section consisted of three cryogenic target "loops." Each of these loops consisted of 4- and 15-cm long aluminum target "cans," heat exchangers (heat loads from the electron beam were typically several hundred watts), high- and low-power heaters (used to maintain the cryotargets at their specified temperatures and to correct for fluctuations in the beam current), and various sensors. Liquid deuterium and liquid hydrogen, maintained at (nominal) operating temperatures of 22 and 19 K, respectively, circulated through two of these loops; the third loop was filled with gaseous helium. Solid (carbon) targets and 4- and 15-cm long "dummy targets," composed of two aluminum foils spaced 4 and 15 cm apart, were mounted on the solid target section of the target ladder. As discussed in more detail later, data were taken with the dummy targets to assess the level of contamination because of scattering from the target cell windows. The thicknesses of the liquid deuterium and liquid hydrogen target cell windows were on the order of 4–6 mils, whereas those of the dummy targets were much thicker and on the order of 36–37 mils.

To mitigate the effects of local boiling, the beam was rastered over a 2×2 mm^2 spot on the cryotargets using a fast raster system [60] located ∼21 m upstream of the cryotargets. Target conditions (e.g., temperatures, heater power levels, etc.) were monitored continuously throughout the duration of the experiment using the standard Hall C cryotarget control system.

F. High momentum spectrometer

Scattered electrons were detected in the HMS, a three-quadrupole, single-dipole (QQQD) spectrometer (all magnets are superconducting) with a solid angle acceptance of 6 msr (defined by an octogonally shaped flared collimator), a maximum central momentum of 7.5 GeV/c, a ±18% momentum acceptance, and a ∼27 m flight path from the target to the detector package.

1. Magnets

The three quadrupole magnets and the dipole magnet are mounted on a common carriage that rotates on a rail system about the target. The quadrupoles are 1.50 T maximum 20-ton (first, Q_1) and 1.56 T maximum 30-ton (second, Q_2, and third, Q_3) superconducting coils with magnetic lengths of 1.89 and 2.10 m, respectively. Q_1 and Q_3 are used for focusing in the dispersive direction, whereas Q_2 provides transverse focusing. The dipole is a 1.66 T maximum 470-ton superconducting magnet with a magnetic length of 5.26 m, a bend angle of 25°, and a bend radius of 12.06 m.

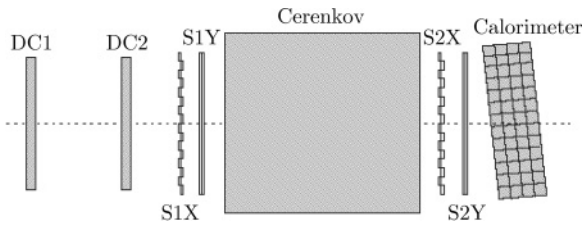

FIG. 2. Schematic diagram of the ordering of the HMS detector package elements. Shown are the two drift chambers (DC1 and DC2), the two x-y hodoscopes (S1X/S1Y and S2X/S2Y), the gas Cerenkov counter, and the lead-glass calorimeter.

The magnets were operated in their standard point-to-point tune in both the dispersive and nondispersive directions. For our central Q^2 points of 0.447, 1.136, 1.169, and 1.474 (GeV/c)^2, the nominal field strengths of Q_1 were 0.11, 0.31, 0.32, and 0.46 T; those of Q_2 were 0.13, 0.37, 0.38, and 0.55 T; those of Q_3 were 0.06, 0.17, 0.18, and 0.26 T; and, finally, those of the dipole were 0.18, 0.47, 0.49, and 0.71 T.

2. Detector package

The detector package is enclosed within a concrete shielding hut and includes two drift chambers, two sets of hodoscopes, a gas Cerenkov counter, and a lead-glass calorimeter. A schematic diagram depicting the ordering of the detector package elements is shown in Fig. 2.

a. Drift chambers. The two multiwire drift chambers [61], used for tracking, each consist of six wire planes: (1) the X and X' planes, which provide position information on the x coordinate (dispersive direction); (2) the Y and Y' planes, which provide position information on the y coordinate (nondispersive direction); and (3) the U and V planes, which are inclined at ±15° angles relative to the orientation of the X and X' planes. As seen by incoming particles, the ordering of these planes is $XYUVY'X'$. The active area of each plane is 113 (x) × 52 (y) cm^2 with an alternating sequence of anode wires (25 μm gold-plated tungsten) and cathode wires (150 μm gold-plated copper-beryllium) spaced ∼1 cm apart. The individual wire planes are separated by 1.8 cm, and the two drift chambers are separated by 81.2 cm. The chambers were filled with equal mixtures (by weight) of argon and ethane and maintained at a pressure slightly above atmospheric pressure. The signals from the anodes were read out in groups of 16 by multihit time-to-digital convertors (TDCs). The fast branch of the signals from the hodoscope TDCs (to be described shortly) defined the TDC start for the electron arm trigger, whereas the delayed signals from the drift chamber TDCs formed the TDC stop.

b. Hodoscopes. The x (y) planes of the two hodoscopes, denoted S1X/S2X (S1Y/S2Y), consist of 16 (10) 75.5-cm (120.5-cm) long Bicron BC404 plastic scintillator bars with a thickness of 1.0 cm and a width of 8.0 cm. UVT lucite light guides and Philips XP2282B photomultiplier tubes (PMTs)

are coupled to both ends of each scintillator bar. The S1X/S1Y and S2X/S2Y planes are separated by ∼2.2 m. The fast branch of the PMT signals was routed to leading-edge discriminators. The discriminated signals were then split, with one set of outputs directed to logic delay modules, TDCs, and scalers, and the other set directed to a logic module. The overall logic signaling a hit in any one of the hodoscope planes required a signal above threshold in at least one of the 16 (10) PMTs mounted on the $x > 0$ ($y > 0$) side of the bars and at least one of the 16 (10) PMTs mounted on the opposite $x < 0$ ($y < 0$) side. The slow branch of the PMT signals was directed to analog-to-digital convertors (ADCs).

c. Cerenkov detector. The Cerenkov detector is a cylindrical tank (165-cm length and 150-cm inner diameter) filled with Perfluorobutane (C_4F_{10}, index of refraction $n = 1.00143$ at STP). The pressure and temperature in the tank were monitored on an (approximately) daily basis and were observed to be highly stable. Pressures were typically ∼0.401–0.415 atm (indices of refraction ∼1.00057–1.00059), translating into energy thresholds of ∼21 MeV (∼5.6 GeV) for pions (electrons). The tank is viewed by two mirrors, located at the rear of the tank, which focus the resulting Cerenkov light into two Burle 8854 PMTs. The signals from these PMTs were directed to ADCs. During this experiment, information from the Cerenkov detector was used only for electron-hadron discrimination and not for HMS trigger logic purposes.

d. Lead-glass calorimeter. The calorimeter consists of 52 TF1 lead-glass blocks stacked into four vertical layers of 13 blocks each. Each block has dimensions of $70 \times 10 \times 10\,\mathrm{cm}^3$, corresponding to ∼16 radiation lengths for the total four-layer-thickness of 40 cm. As is indicated in Fig. 2, the four layers of the calorimeter are tilted at an angle of 5° relative to the central axis of the detector package to eliminate losses in the gaps between the individual blocks. Philips XP3462B PMTs are coupled to one end of each block, and the signals from these PMTs were routed to ADCs. Again, information from the lead-glass calorimeter was not used for HMS trigger logic purposes during this experiment.

IV. NEUTRON POLARIMETER

A. Overview

A schematic diagram of the experimental arrangement with an isometric view of the neutron polarimeter is shown in Fig. 3. The first element in the NPOL flight path was a dipole magnet (Charybdis) with a vertically oriented field that was used to precess the neutrons' spins through an angle χ in a horizontal plane. As a by-product, protons and other charged particles were swept from the acceptance during asymmetry measurements conducted with the field energized. The next item in the flight path was a 10.16-cm-thick lead curtain, located directly in front of a steel collimator (not shown in this figure). The lead curtain served to attenuate the flux of electromagnetic radiation and to degrade in energy the flux of charged particles incident on the polarimeter's detectors.

The polarimeter consisted of 70 plastic scintillation detectors enclosed within a steel-and-concrete shielding hut. The front array of the polarimeter functioned as the polarization analyzer (via spin-dependent scattering from unpolarized protons in hydrogen and carbon nuclei), whereas the top and bottom rear arrays, shielded by the collimator from a direct line-of-sight to the target, were configured for sensitivity to an up-down scattering asymmetry proportional to the projection of the recoil polarization on a horizontally oriented "sideways" axis (see next subsection). Double layers of thin-width "veto/tagger" detectors located directly ahead of and behind the front array tagged incoming and scattered charged particles. The flight path from the center of the target to the center of the front array was 7.0 m, and the distance from the center of the front array to the center of the rear array (along the polarimeter's central axis) was ∼2.5 m.

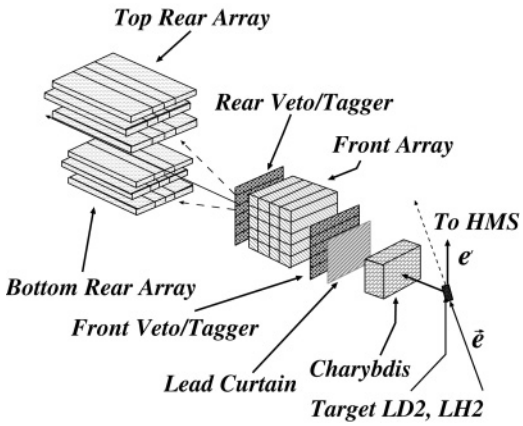

FIG. 3. Isometric view of the NPOL flight path showing the Charybdis dipole magnet, the lead curtain, the front veto/tagger array, the front array, the rear veto/tagger array, and the top and bottom rear arrays.

B. Polarimetry

1. Coordinate systems

Here we establish some necessary notation for a number of different coordinate systems to which we refer throughout the remainder of this article.

First, calculations of recoil polarization for the quasielastic $^2\mathrm{H}(\vec{e}, e'\vec{n})^1\mathrm{H}$ reaction are usually referred to a $(\hat{t}, \hat{n}, \hat{\ell})$ *reaction basis*, defined on an *event-by-event basis* in the n-p c.m. frame according to

$$\hat{\ell} \| \mathbf{p}_n^{\mathrm{c.m.}}, \quad \hat{n} \| \mathbf{q}^{\mathrm{c.m.}} \times \mathbf{p}_n^{\mathrm{c.m.}}, \quad \hat{t} = \hat{n} \times \hat{\ell}, \tag{6}$$

where $\mathbf{p}_n^{\mathrm{c.m.}}$ and $\mathbf{q}^{\mathrm{c.m.}}$ denote, respectively, the incident neutron's momentum and the momentum transfer in the n-p c.m. frame. The reaction basis can best be visualized by referring to the schematic diagram of the kinematics in the n-p c.m. frame shown in Fig. 30 of Appendix A.

Second, we define a *polarimeter basis*, $(\hat{x}_{\mathrm{NPOL}}, \hat{y}_{\mathrm{NPOL}}, \hat{z}_{\mathrm{NPOL}})$, *fixed for all events*, defined in the laboratory frame according to

$$\hat{z}_{\mathrm{NPOL}} \parallel \text{NPOL central axis}, \tag{7a}$$

$$\hat{y}_{\mathrm{NPOL}} \perp \text{Hall C floor}, \tag{7b}$$

$$\hat{x}_{\mathrm{NPOL}} = \hat{y}_{\mathrm{NPOL}} \times \hat{z}_{\mathrm{NPOL}}, \tag{7c}$$

with the center of the target defined to be the origin of this coordinate system.

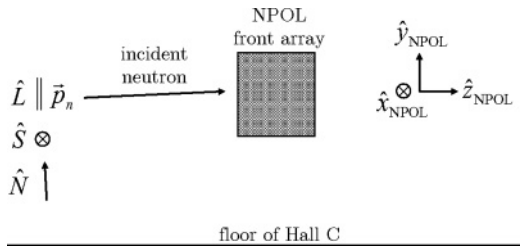

FIG. 4. Schematic diagram of the $(\hat{x}_{\rm NPOL}, \hat{y}_{\rm NPOL}, \hat{z}_{\rm NPOL})$ polarimeter basis (fixed for all events) and the $(\hat{S}, \hat{N}, \hat{L})$ polarimeter momentum basis (defined on an event-by-event basis). Note that as $\mathbf{p}_n$ is not, in general, restricted to the $\hat{y}_{\rm NPOL}$-$\hat{z}_{\rm NPOL}$ plane, $\hat{S}$ is not, in general, parallel to $\hat{x}_{\rm NPOL}$.

Third, the symmetric geometric configuration of the polarimeter's top/bottom rear arrays suggests the introduction of a *polarimeter momentum basis*, $(\hat{S}, \hat{N}, \hat{L})$, which we again define on an *event-by-event basis* in the laboratory frame according to

$$\hat{L} \parallel \hat{p}_n, \quad \hat{S} \parallel \hat{y}_{\rm NPOL} \times \hat{p}_n, \quad \hat{N} = \hat{L} \times \hat{S}, \tag{8}$$

where $\hat{p}_n$ denotes a unit vector along the incident neutron's momentum in the laboratory frame. We will henceforth refer to the $\hat{S}$ and $\hat{L}$ axes as the polarimeter's "sideways" and "longitudinal" axes of sensitivity, respectively. We express the recoil polarization in terms of the polarimeter momentum basis as $\mathbf{P} = P_S\hat{S} + P_N\hat{N} + P_L\hat{L}$.

A schematic diagram showing the orientation of the polarimeter basis and polarimeter momentum basis coordinate systems is shown in Fig. 4.

2. Detected scattering asymmetry

We define NPOL polar and azimuthal scattering angles, denoted $\theta_{\rm scat}$ and $\phi_{\rm scat}$, according to

$$\sin\theta_{\rm scat} = |\hat{p}_n \times \hat{p}'_n|, \tag{9a}$$

$$\cos\phi_{\rm scat} = \hat{S} \cdot \hat{u}, \tag{9b}$$

where $\hat{p}'_n$ is a unit vector along the scattered neutron's three-momentum, and the unit vector $\hat{u}$ is defined according to $\hat{u} = (\hat{p}_n \times \hat{p}'_n)/|\hat{p}_n \times \hat{p}'_n|$.

The cross section for elastic polarized-nucleon, unpolarized-nucleon scattering, denoted $\sigma(\theta_{\rm scat}, \phi_{\rm scat})$ for short, is of the form [62]

$$\begin{aligned}\sigma(\theta_{\rm scat}, \phi_{\rm scat}) &= \sigma_0(\theta_{\rm scat})[1 + A_y(\theta_{\rm scat})\mathbf{P} \cdot \hat{u}] \\ &\approx \sigma_0(\theta_{\rm scat})[1 + A_y(\theta_{\rm scat})P_S \cos\phi_{\rm scat}],\end{aligned} \tag{10}$$

where $\sigma_0(\theta_{\rm scat})$ and $A_y(\theta_{\rm scat})$ denote the unpolarized cross section and the analyzing power, respectively. The above approximation is valid in the limit that P_N is small. It is then clear that the asymmetry, $\xi(\theta_{\rm scat}, \phi_{\rm scat})$, between scattering "up" ($\hat{S} \cdot \hat{u} < 0 \Rightarrow \cos\phi_{\rm scat} < 0$) and scattering "down" ($\hat{S} \cdot \hat{u} > 0 \Rightarrow \cos\phi_{\rm scat} > 0$) into infinitesimal solid angles $(\theta_{\rm scat}, \phi_{\rm scat})$ and $(\theta_{\rm scat}, \phi_{\rm scat} + \pi)$, respectively, for a particular value of P_S is

$$\begin{aligned}\xi(\theta_{\rm scat}, \phi_{\rm scat}) &= \frac{\sigma(\theta_{\rm scat}, \phi_{\rm scat}) - \sigma(\theta_{\rm scat}, \phi_{\rm scat} + \pi)}{\sigma(\theta_{\rm scat}, \phi_{\rm scat}) + \sigma(\theta_{\rm scat}, \phi_{\rm scat} + \pi)} \\ &= A_y(\theta_{\rm scat})P_S \cos\phi_{\rm scat}.\end{aligned} \tag{11}$$

A single value of P_S is not, of course, presented to the polarimeter. Also, the top and the bottom rear arrays have a finite geometry; therefore, if the polarimeter is geometrically symmetric in $\phi_{\rm scat}$ (i.e., geometrically symmetric top and bottom rear arrays), the detected scattering asymmetry (i.e., averaged over kinematics and the top/bottom finite geometry), $\langle\xi\rangle$, is

$$\langle\xi\rangle = \langle P_S\rangle A_y^{\rm eff}, \tag{12}$$

where $\langle P_S\rangle$ and $A_y^{\rm eff}$ denote, respectively, the acceptance-averaged value of the sideways component of the polarization and the polarimeter's effective analyzing power averaged over its geometric acceptance (i.e., over $\cos\phi_{\rm scat}$). Henceforth, when we refer to the analyzing power A_y, it should be understood that we are referring to $A_y^{\rm eff}$.

C. Charybdis dipole magnet and spin precession

The Charybdis magnet was a water-cooled, 38-ton, 1.5-m-tall, 2.3-m-wide, and 1.7-m-long iron dipole magnet installed in Hall C specifically for this experiment. The magnet was configured such that the gap between the pole pieces was 8.25 inches, and the geometric center of the magnet was located a distance of 2.107 m from the center of the target. The two poles were wired in parallel and powered with a 160-V 1000-A power supply. Two-inch-thick iron field clamps with apertures machined to match the 8.25-inch pole gap were placed at the entrance and exit apertures, resulting in an effective magnetic length of $\sim$1.7 m.

Calculations of the Charybdis field profile were performed with the TOSCA program [63] for various currents, and values for the field integral, $\int |\mathbf{B}| d\ell$, along the central axis were derived from these calculations. The currents were tuned for the various spin precession angles, χ, according to the relation

$$\chi = \frac{\mu_N g}{\beta_n} \int |\mathbf{B}| d\ell, \tag{13}$$

where μ_N is the nuclear magneton, $g/2 = -1.913$ for the neutron, and β_n denotes the neutron's velocity in units of c. The field integrals for the precession angles at each of our Q^2 points are tabulated in Table III.

The field along the central axis was mapped [64] at the conclusion of the experiment. We found that the values for the field integrals derived from our mapping results and the TOSCA calculations agreed to better than 0.76% for

TABLE III. Summary of the nominal values of the field integrals (along the central axis) for the spin precession angles at each Q^2 setting. β_n denotes the neutron velocity in units of c for the nominal (central) kinematics.

Central Q^2 [(GeV/c)^2]	β_n	Precession angle χ	$\int \lvert\mathbf{B}\rvert d\ell$ (T-m)
0.447	0.604	$\pm 40^\circ$	0.6884
1.136	0.794	$\pm 90^\circ$	2.0394
1.169	0.799	$\pm 40^\circ$	0.9123
1.474	0.839	$\pm 40^\circ$	0.9576
1.474	0.839	$\pm 90^\circ$	2.1547

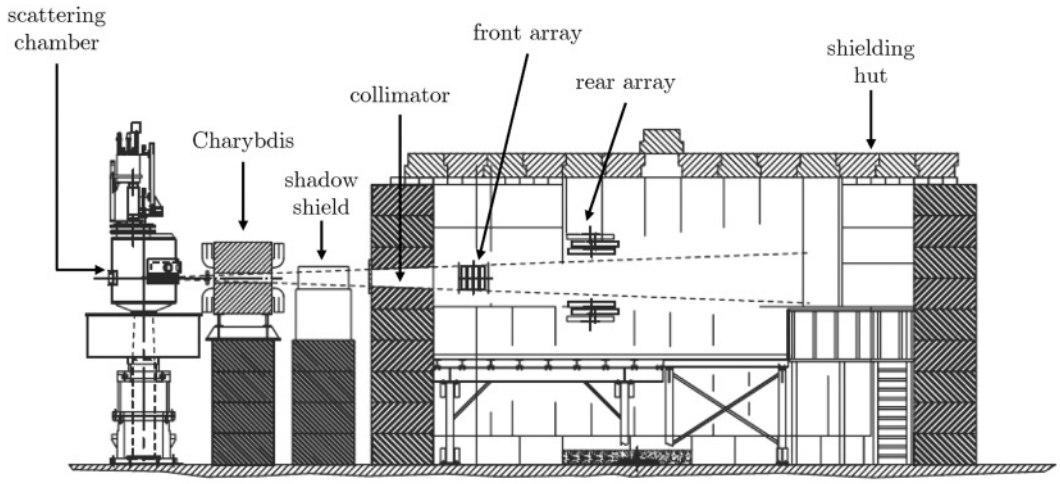

FIG. 5. Schematic diagram (side view) of the NPOL shielding hut. The physical acceptance of the polarimeter, as defined by the collimator, is indicated by the dashed lines originating in the target. The rear array detectors were shielded from a direct line-of-sight to the target. The shadow shield, when inserted, was used to assess the room background rates.

$\chi = \pm 40^\circ$ precession at $Q^2 = 0.447$ (GeV/c)^2, 0.21% for $\chi = +40^\circ$ precession at $Q^2 = 1.169$ (GeV/c)^2, and 0.35% for $\chi = +40^\circ$ precession at $Q^2 = 1.474$ (GeV/c)^2. Small differences in the measured field integrals for the two magnet polarities (corresponding to a $\pm 0.3^\circ$ spread) were observed for $\chi = \pm 40^\circ$ precession at $Q^2 = 0.447$ (GeV/c)^2. Although we did not conduct field measurements for both polarities at the other Q^2 points, it is reasonable to assume that the magnet behaved similarly for other current settings.

D. Neutron polarimeter physical acceptance

The physical acceptance of the polarimeter was defined by a steel collimator with entrance and exit apertures located 483.92 and 616.00 cm, respectively, from the center of the target. The collimator was tapered, with the entrance (exit) port spanning a width of 72.6 cm (92.4 cm) and a height of 37.3 cm (47.5 cm). The 10.16-cm-thick lead curtain was located immediately upstream of the collimator's entrance port.

A schematic diagram of the polarimeter's shielding hut showing the shielding of the rear array detectors by the collimator from a direct line-of-sight to the target appears in Fig. 5.

E. Neutron polarimeter detectors

The polarimeter consisted of a total of 70 mean-timed BICRON-400 plastic scintillation detectors subdivided into a front veto/tagger array, a front array, a rear veto/tagger array, and symmetric top and bottom rear arrays. The front wall of the polarimeter's shielding hut was composed of 132.08-cm-thick steel blocks; the only opening in this wall was the lead-shielded collimator. A schematic diagram of the polarimeter's detector configuration is shown in Fig. 6.

1. Front veto/tagger array

The function of the first series of detectors in the neutron flight path, the front veto/tagger array, was to identify charged

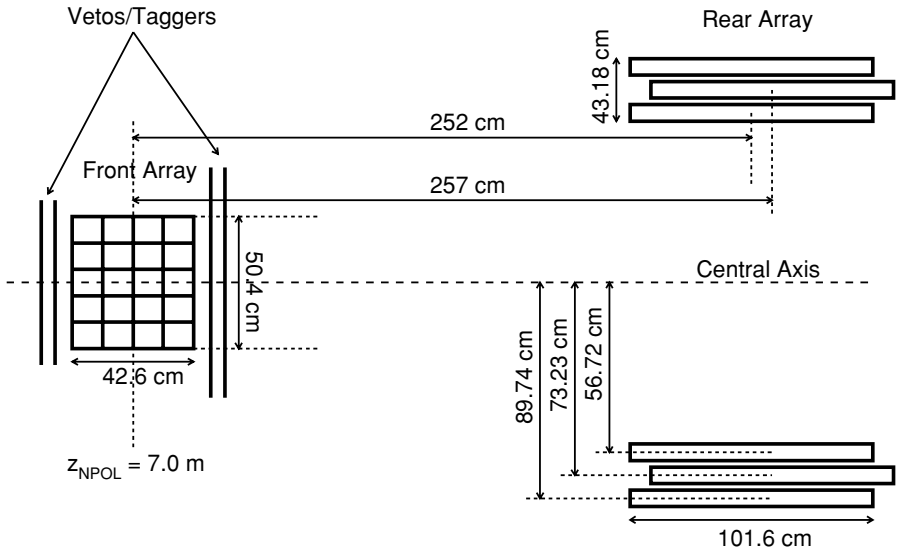

FIG. 6. Schematic diagram (side view) of the NPOL detector configuration showing the top and bottom rear subarrays for measurement of an up-down scattering asymmetry.

particles incident on the polarimeter. This veto array consisted of two vertically stacked layers of five $160.0 \times 11.0 \times 0.635$ cm^3 scintillators stacked with their long (160.0 cm) axes oriented horizontally and perpendicular to the central flight path and the thin (0.635 cm) dimension oriented along the flight path. The vertical spacing between the detectors in each layer was $\sim$1 mm; therefore, to eliminate charged particle leakage, the two layers were offset from each other in the vertical direction by $\sim$1 cm. Each scintillator bar was coupled to two Philips XP2262 2-inch PMTs via Plexiglas light guides.

2. Front array

The front array was segmented into 20 $100 \times 10 \times 10$ cm^3 scintillators; segmentation of the front array permitted us to run with luminosities as high as 3×10^{38} cm^{-2} s^{-1} (70 μA current on a 15-cm liquid deuterium target). The long (100 cm) axes of these detectors were oriented horizontally and perpendicular to the central flight path and were stacked vertically into four layers of five detectors. The long ends of each scintillator were coupled via Plexiglas light guides to 2-inch Hamamatsu R1828-01 PMTs powered by bases designed specifically for this experiment for purposes of high gain and highly linear output under conditions of high rate [65].

3. Rear veto/tagger array

Similar to the front veto/tagger array, the purpose of the rear veto/tagger array was to identify charged particles (e.g., recoil protons from *np* interactions in the front array) exiting the front array. The detectors in this array were identical to those in the front veto/tagger array and were vertically stacked in a similar fashion into two layers of eight detectors each. [We note that only one layer of eight detectors existed for the early part of the experiment during our $Q^2 = 1.136$ (GeV/c)^2 run.] As in the front veto/tagger array, each scintillator was coupled to two 2-inch Philips XP2262 PMTs.

4. Rear array

The top and bottom rear arrays each consisted of 12 detectors stacked into 3 layers of 4 detectors each. Each layer contained two "10-inch" $25.4 \times 10.16 \times 101.6$ cm^3 detectors sandwiched in between two larger "20-inch" $50.8 \times 10.16 \times 101.6$ cm^3 detectors. These detectors were oriented with their long (101.6 cm) axes parallel to the central flight path and their 50.8 or 25.4 cm dimensions oriented horizontally. The centers of the inner, middle, and outer layers were located a vertical distance of 56.72, 73.23, and 89.74 cm, respectively, above or below the central axis of the polarimeter and a horizontal distance of 2.52, 2.57, and 2.52 m, respectively, from the front-array geometric center (see Fig. 6). The long ends of each scintillator were coupled via Plexiglas light guides to 5-inch Hamamatsu R1250 PMTs powered by the same bases built for the front array.

The vertical positions of the top and bottom arrays relative to the polarimeter's central axis were optimized for front-to-rear scattering angles near the peak of the analyzing power for *np* scattering ($\sim$15°–20° for our range of neutron energies). This configuration with scattering angles in the vicinity of $\sim$15°–20° also guaranteed, for our kinematics, that only one of the nucleons (for elastic *np* interactions in the front array and assuming straight-line trajectories for the recoil proton through the front array) scattered into either the top or bottom array. We also note that the horizontal position of the middle detector plane was staggered relative to those of the inner and outer layers so that the majority of the front-to-rear tracks passed through at least two of the three horizontal planes, reducing the dependence of the rear array detection efficiency on the scattering angle.

F. Electronics, event logic, and data acquisition

1. Electronics

The signals from the 140 NPOL PMTs were processed with electronics sited in two locations: (1) one set, located inside the shielding hut, was used to form the timing logic signal for each PMT (past experience with neutron time-of-flight and polarimetry experiments [66] revealed that locating the discriminators as close to the PMTs as practical yielded the best timing resolution); and (2) another set, located in the counting house, was used to define the logic for the various event types.

A schematic diagram of the configuration of the electronics in the shielding hut for each scintillator bar in the front and rear arrays is shown in Fig. 7. High voltage was applied to each PMT remotely by an EPICS-controlled 64-channel high-voltage CAEN mainframe crate located in the counting house. Modest levels of high voltage were applied to the PMTs for the front array detectors, as deterioration in the performance of these PMTs was of concern because of the high count rates in these scintillators; however, no deterioriation in their performance was observed during the experiment (instead, gains were stable to within $\sim$10%). To compensate for the resulting lower levels of gain obtained directly from these PMTs, the anode signals were preamplified by fast preamplifiers with a gain of eight, custom-designed and assembled for this experiment. The anode signals from the PMTs in the rear array and the front and rear veto/tagger arrays were not preamplified.

The anode signals from the front and rear arrays were then directed to an LED driver and pulse height monitor. When desired, this device was used to assess the response of each PMT to a flashing blue LED mounted on its light guide. The centroid channels of the LED spectra were monitored periodically, and any necessary changes to the high voltage levels were performed remotely. The gains of the front and rear veto/tagger array PMTs were not monitored with this system.

The anode signals from all four detector arrays were then split. The signals in the fast branch (for the event trigger and timing measurements) were directed to either constant-fraction discriminators (front and rear arrays) or leading-edge discriminators (front and rear veto/tagger arrays) located inside the shielding hut and then sent to the electronics in the counting house. We did not employ constant-fraction discrimination for the veto/tagger array detectors for the following reasons: (1) the dynamic range of energy deposition in these detectors was small for those events of interest, so the time-walk was tolerable; and (2) the timing measurements from these detectors were not used for energy determinations,

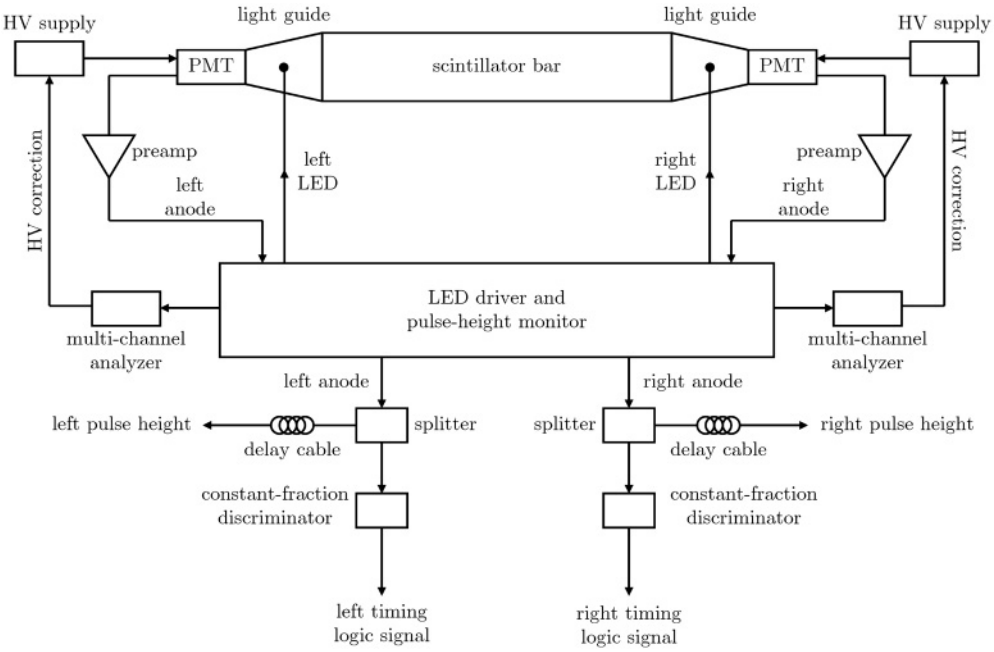

FIG. 7. Schematic diagram of the configuration of the electronics in the shielding hut for the front and rear array detectors. Note that the anode signals from the rear array detectors were not preamplified.

so resolutions of a few ns were sufficient for charged particle tagging. Those signals diverted to the slow branch were routed through delays located inside the shielding hut and then sent to the counting house.

Upon arrival in the counting house, both the analog and timing signals were directed through filters/transformers designed to eliminate low-frequency noise. The analog signals were then sent directly to ADCs, whereas the timing signals were first sent to discriminators and then routed to two branches of a timing circuit. In one branch, the output from these discriminators were directed through level translators, delays, discriminators, and then further split and directed to TDCs and scalers. In the other branch of this timing circuit (used to form the event triggers), the timing signals from the PMTs on all of the detectors, except those in the rear veto/tagger array, were first sent to logic modules that were used to generate logic signals for coincidences between the timing signals for the two PMTs on each detector. Logical ORs were generated for each of the 20 front array detector two-PMT coincidences. These signals were then sent to a fan-in with one set of outputs directed to scalers and the other through a discriminator; the output from this discriminator was then directed to the trigger circuit. The logical ORs for the rear array detectors and the front veto/tagger-array detectors were routed through a fan-in and then directed to the trigger circuit. The timing signals from the rear veto/tagger-array detectors were not used for trigger purposes.

2. *Event logic and triggers*

All event trigger logic was performed by two LeCroy 8LM 2365 Octal Logic Matrix modules. Pretrigger logic signals from the HMS (coincident hits in at least three of the four hodoscope planes), the NPOL front array, the NPOL rear array, and the NPOL front veto/tagger array were routed to the 8LM modules. In addition to these logic signals, triggers from the polarized electron source were also input to these modules. As previously discussed, the helicity of the electron beam was flipped pseudorandomly at 30 Hz. Electronics at the polarized source generated a logic signal for readout of helicity-gated scalers for each 33.3-ms helicity window. Further, these modules also generated a helicity-transition logic signal that was used to veto otherwise valid data triggers that occured during transitions at the polarized source from one helicity state to another. The duration of this helicity-transition logic pulse was $\sim$600 μs, resulting in an effective data-taking helicity window of $\sim$32.7 ms.

An electronic module known as the trigger supervisor (TS) functioned as the interface between the 8LM logic modules and the data acquisition system (DAQ). The TS generated a logic signal indicating the status of the DAQ (e.g., busy or not busy) that was input to the logic modules. The logic modules then determined whether the logic for any of the eight possible physics triggers (e.g., electron singles, electron/front array coincidences, electron/front array/rear array coincidences, etc.) was satisfied. If the logic for any particular trigger was satisfied, the TS generated an accept signal leading to generation of the appropriate ADC gate and TDC common signals. The ADCs, TDCs, and scalers were then read out with real-time UNIX-based processors.

The event triggers of interest were threefold coincidences between hits in the electron arm, the front array, and the rear array. These events constituted $\sim$80–85% of the event triggers, as the higher rate events, such as electron singles or twofold coincidences between the electron arm and the front array, were prescaled.

3. Data acquisition

The DAQ was controlled by the CEBAF Online Data Acquisition System (CODA) [67]. CODA includes an event-builder subsystem programed to assemble the individual ADC channel, TDC channel, and scaler read-out data fragments into an event. The data for the events were then written to disk in CODA format by another subsystem.

Typical data acquisition rates were one million events in $\sim$1.0 ($\sim$0.5) hr with the Charybdis dipole field energized (deenergized).

V. DATA ANALYSIS

A. Electron reconstruction and tracking

1. Overview of analysis code

The raw ADC, TDC, and scaler data written to disk and encoded by the DAQ in CODA format were decoded with a modified version of the standard Hall C ENGINE analysis code (see, e.g., Ref. [68] for a discussion of the standard version) employed for the analysis of nearly all experiments conducted in Hall C. Modifications to the standard version were necessary to accommodate the raw data stream from the 70 NPOL detectors; hereafter, whenever we refer to the ENGINE analysis code, it should be assumed that we are referring to our modified version of this code.

For each event, the scattered electron's track through the HMS was reconstructed, and various kinematic quantities (e.g., momentum, energy, focal plane distributions, etc.) were computed. ENGINE was not configured to reconstruct the track of the nucleon through the polarimeter; instead, the NPOL detector data were simply written to new data files for later processing by other analysis tools.

2. Extraction of electron information

a. Tracking. The overall strategy of the tracking algorithm [68] was to use the hit information from the drift chambers and reference start times provided by TDC information from the scintillators in the hodoscope planes to reconstruct the trajectory of the particle through the drift chambers. TDC information from those scintillators in the hodoscope planes recording hits was used to establish reference start times. This information, coupled with TDC information from the drift chambers, was then used to determine the location of the hit in the drift chamber planes. "Left-right ambiguities" in the drift chambers (i.e., whether a particle passed to the left or right of any given wire) were resolved by fitting a (straight-line) track to each left-right hit combination in the six planes of each drift chamber. The full track through both drift chambers with the overall smallest track reconstruction χ^2 was defined to be the final reconstructed track through the drift chamber planes.

b. Transport. Engine then attempted to relate the positions and angles at the focal plane (determined from the track through the drift chambers) to target quantities. In standard coordinate notation for transport through a spectrometer, $\hat{z}_{\rm fp}$ is taken to point along the central ray of the spectrometer, $\hat{x}_{\rm fp}$ in the dispersive direction (by convention, taken to point "downwards"), and $\hat{y}_{\rm fp} = \hat{z}_{\rm fp} \times \hat{x}_{\rm fp}$. It should be noted that HMS focal-plane variables are traditionally referred to the detector focal plane, defined to be perpendicular to the central ray (i.e., parallel to the drift chamber planes) with the origin of the $x_{\rm fp}$-$y_{\rm fp}$ plane defined to be that point in space where the central ray of the spectrometer intersects the true (magnetic) focal plane. In addition to the dispersive and nondispersive variables, two other standard transport variables, $x'_{\rm fp}$ and $y'_{\rm fp}$, are defined to be the slopes of the rays at the focal plane, $x'_{\rm fp} \equiv dx_{\rm fp}/dz$ and $y'_{\rm fp} \equiv dy_{\rm fp}/dz$, respectively. The focal plane variables $x_{\rm fp}$, $y_{\rm fp}$, $x'_{\rm fp}$, and $y'_{\rm fp}$ were converted to target quantities $x'_{\rm tar} \equiv dx_{\rm tar}/dz$, $y_{\rm tar}$, $y'_{\rm tar} \equiv dy_{\rm tar}/dz$, and $\delta \equiv (|\mathbf{p}_{e'}| - |\overline{\mathbf{p}_{e'}}|)/|\overline{\mathbf{p}_{e'}}|$, where $|\overline{\mathbf{p}_{e'}}|$ denotes the central momentum setting, via computation of transport matrix elements derived from optics studies. For this choice of target coordinates, $x_{\rm tar}$ was not reconstructed but was, instead, defined to be $x_{\rm tar} = 0$ for all events.

3. Sample electron reconstruction results

Sample histograms of the reconstructed δ distribution, hereafter referred to as the "$\Delta p/p$ distribution," at our lowest and highest Q^2 points are shown in Fig. 8. The quasielastic peak is clearly visible in both spectra, but a large accompanying background of inelastic events associated with pion production in the target is present in the $Q^2 = 1.474$ (GeV/c)^2 spectrum. Inelastic peaks were also clearly visible in the $Q^2 = 1.136$ and 1.169 (GeV/c)^2 spectra but are not shown here. A sample two-dimensional histogram of $\Delta p/p$ plotted versus the

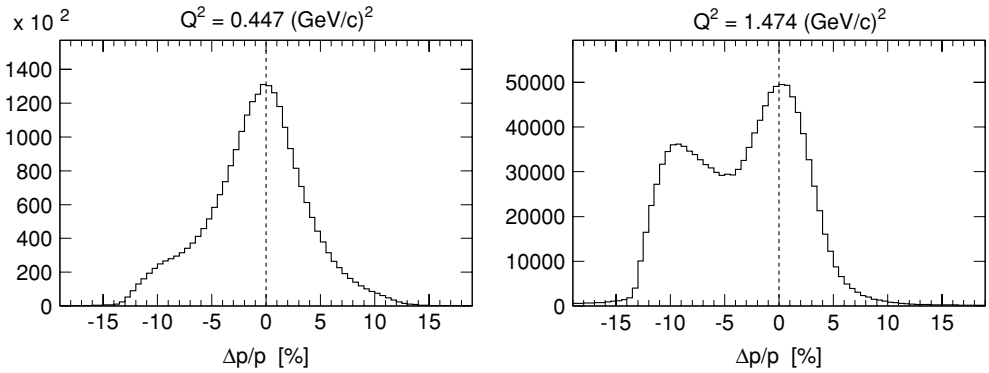

FIG. 8. Distributions of $\Delta p/p$ for the full HMS acceptance at $Q^2 = 0.447$ and 1.474 (GeV/c)^2.

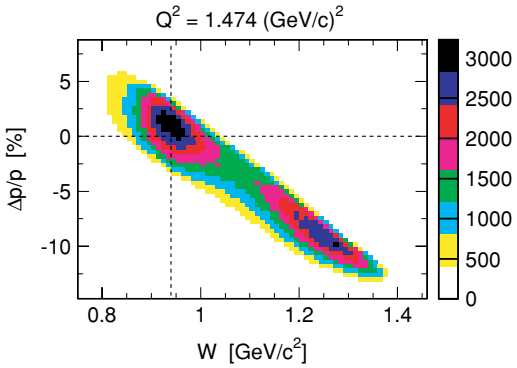

FIG. 9. (Color online) Correlation plot of $\Delta p/p$ versus W for the full HMS acceptance at $Q^2 = 1.474$ (GeV/c)^2.

invariant mass, W, calculated from the electron kinematics according to

$$W = \sqrt{(\omega + m_N)^2 - |\mathbf{q}|^2}, \tag{14}$$

where m_N is the nucleon mass, is shown in Fig. 9 for our $Q^2 = 1.474$ (GeV/c)^2 point. The $\Delta(1232)$ resonance is prominent in this distribution.

Hadrons in the HMS were identified via examination of the Cerenkov photoelectron spectrum. As expected, a hadron peak was not visible in the $Q^2 = 0.447$ (GeV/c)^2 spectrum; however, prominent hadron peaks (at zero photoelectrons) were observed at the three higher Q^2 settings. An example of such a photoelectron spectrum from our $Q^2 = 1.474$ (GeV/c)^2 data is shown in Fig. 10. Cuts on the number of photoelectrons, coupled with cuts on the energy deposition in the calorimeter, were sufficient for electron-hadron discrimination.

B. Neutron polarimeter energy calibration

The (charge-integrating) ADCs for the front and rear array detector PMTs were calibrated with the Compton spectra from a ^{228}Th source (2.61 MeV γ rays); the front and rear veto/tagger array detectors were not calibrated as ADC information was not used for charged particle tagging. These calibrations were parametrized in terms of an equivalent electron energy (denoted "eVee"), where the relation between

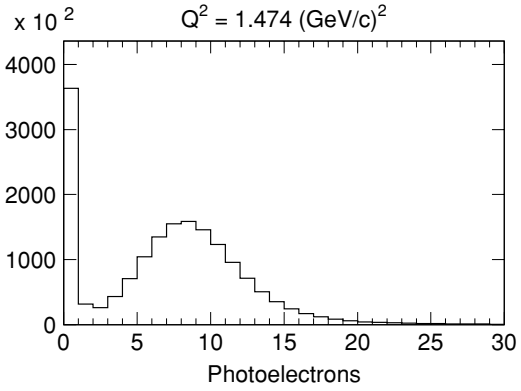

FIG. 10. Cerenkov photoelectron spectrum for the full HMS acceptance at $Q^2 = 1.474$ (GeV/c)^2. A prominent hadron peak appears at zero photoelectrons.

the light output of recoil protons and Compton-scattered electrons in organic scintillator was found by Madey *et al.* [69] to be well described by the parametrization

$$T_e = a_1[1 - \exp(-a_2(T_p)^{a_3}] + a_4 T_p. \tag{15}$$

Here, T_p denotes the energy deposition of a recoil proton, T_e denotes the energy deposition of an electron that yields the equivalent light output, and the a_i are empirically determined parameters.

Unfortunately, the range of electron energies (2.38 MeV Compton edge) was not sufficient, as typical energy depositions for the recoil protons were estimated to be approximately greater than several MeV [13]; further, the hardware thresholds for the front- (rear-) array detectors were set at 4 (10) MeVee. To remedy these shortcomings, a custom-designed linear amplifier with a gain of 10 was placed in the timing circuit during calibration runs. The resulting ADC spectra were fitted to the sum of the Klein-Nishina distribution (smeared by a Gaussian resolution function) and an exponential background tail. Pulse-height calibrations were performed at three different times during the experiment (roughly at the start, middle, and conclusion); minor differences ($\sim$10%) in the extracted calibration parameters were observed but were deemed to be relatively unimportant as the selection of quasielastic ^{2}H$(e, e'n)^1$H events did not rely heavily on pulse height information.

C. Neutron polarimeter timing calibration

To optimize track reconstruction and background rejection in the neutron polarimeter, the relative timing relationships between the NPOL detectors and the HMS were carefully calibrated with a series of algorithms designed to (1) generate position calibrations for each detector, (2) generate relative timing calibrations for each detector in the front array and discern the relationship between the mean time for each front array detector and the trigger mean time, (3) calibrate the timing between the HMS and the front array (yielding a coincidence time-of-flight), (4) generate relative timing calibrations for each detector in the rear array and calibrate the time-of-flight between the front array and the rear array, and (5) generate position and timing calibrations for the front and rear veto/tagger detectors.

1. Front- and rear-array position calibrations

The position calibration algorithm for the front- and rear-array detectors employed data acquired with the Charybdis magnet deenergized, such that charged particles illuminated the front array almost uniformly. The relationship between the hit position and the difference (in channels) between the TDCs from the PMTs mounted on the two ends of each scintillator was parametrized in a linear form with an unknown slope and offset. Histograms of these TDC channel differences were accumulated for each detector and then boxcar smoothed. The algorithm identified the channel of maximum content and then scanned away in both directions until channels with 10% of the maximum content were identified. Slope and offset parameters were then chosen such that these 10%-content channels were aligned with the physical edges of each detector; the resulting

calibrated position spectra displayed sharp edges near the physical detector edges.

2. Front-array timing and trigger calibrations

The first goal of the front-array timing calibration was to align the mean times of all the detectors in the front array using events with a single hit in the front array. Data acquired with the Charybdis magnet energized (for suppression of background processes) were employed for this step of the timing calibration, and events with >0 (>1) hits in the front veto/tagger array (front array) were discarded. An offset was chosen for each detector such that the mean value of its mean-time spectrum was aligned on zero.

The second goal of the front array timing calibration was to construct a variable that could be used to identify which hit generated the trigger (for events with multiple front array hits), as the trigger circuit did not identify the triggering hit. Proper identification of the triggering hit via examination of the correlation between the TDC channels for the two PMTs on each detector and the position dependence of the mean times yielded self-timing spectra with FWHM of $\sim$0.4 ns.

3. Coincidence time-of-flight calibrations

To maximize our signal-to-noise ratio, we constructed a coincidence time-of-flight variable that accounted for the quasielastic ^{2}H$(e, e'n)^1$H kinematics, path-length variations through the HMS and NPOL, and variations in the delay between an interaction in a detector and the arrival of its timing signal at the TDC. For this step of the calibration, a minimal set of cuts were applied to the data for purposes of (loose) quasielastic event selection (e.g., cuts on the calorimeter energy deposition, $\Delta p/p$, etc.). Again, front array single-hit events (with no hits in the front veto/tagger array) acquired with the Charybdis magnet energized were used for this step of the calibration.

The algorithm first predicted the neutron time-of-flight from the target to the front array using only position information (i.e., the reconstructed vertex information for the primary scattering event in the target cell and the position of the front array hit) and electron kinematics. For a three-body final state (i.e., no pion production), four-momentum conservation demands

$$m_d + \omega = \sqrt{|\mathbf{p}_n|^2 + m_n^2} + \sqrt{|\mathbf{p}_p|^2 + m_p^2}, \tag{16a}$$

$$\mathbf{q} = \mathbf{p}_n + \mathbf{p}_p. \tag{16b}$$

From this, it follows that a value for $|\mathbf{p}_n|$ (and, then, the predicted neutron time-of-flight) can be derived from the solution to the quadratic equation $A|\mathbf{p}_n|^2 + B|\mathbf{p}_n| + C = 0$, where

$$A = (m_d + \omega)^2 - (\mathbf{q} \cdot \hat{p}_n)^2, \tag{17a}$$

$$B = -2(\mathbf{q} \cdot \hat{p}_n)D, \tag{17b}$$

$$C = m_n^2(m_d + \omega)^2 - D^2, \tag{17c}$$

$$2D = m_d^2 + m_n^2 - m_p^2 - Q^2 + 2m_d\omega. \tag{17d}$$

A value for the actual measured time-of-flight was then extracted from information in the signal output of a TDC started by a signal generated by the NPOL trigger and stopped by the HMS trigger, a correction for path-length variations and delays between interactions and signals in the HMS computed by ENGINE, and the mean time of the front-array detector recording the hit. This measured time-of-flight was then compared with the predicted time-of-flight, and the resulting difference, the coincidence time-of-flight (hereafter, referred to as cTOF), was computed for each event. The resulting cTOF spectra were fairly narrow with FWHM of $\sim$1.25 ns and signal-to-noise ratios of $\sim$6:1–10:1. Sample cTOF spectra are shown later in this article.

4. Rear-array timing calibrations

The algorithm for the rear-array timing calibration selected single-hit events (with no hits in both the front and rear veto/tagger arrays) acquired with the Charybdis magnet energized and then filtered these hits according to a set of cuts designed to select quasielastic events. In addition, a $|\text{cTOF}| \leqslant 2$ ns cut was enforced.

In the first step, the algorithm aligned the mean time spectra of the rear array detectors relative to each other. As for the front array, histograms of mean times were accumulated for each detector. The channel of maximum content was identified, and an offset parameter for each detector was then chosen such that the peak channel was aligned on zero.

In the second step, the algorithm performed an absolute timing calibration of the rear-array detectors relative to the front-array detectors via a front-to-rear velocity calibration. The scattering angle for the front-to-rear track was computed using the incident neutron's three-momentum and the position information for the hits in the front and rear array. The algorithm then predicted the front-to-rear velocity for elastic *np* scattering in the front array via computation of the scattered neutron's kinetic energy, T_{np}, where

$$T_{np} = \frac{2T_n \cos^2\theta_{\text{scat}}}{(\gamma_n + 1) - (\gamma_n - 1)\cos^2\theta_{\text{scat}}}. \tag{18}$$

Here, T_n denotes the incident neutron's kinetic energy, θ_{scat} denotes the neutron scattering angle in the polarimeter, γ_n is the usual Lorentz factor for the incident neutron, and the proton and neutron masses are assumed to be equal. Relative time-of-flight (hereafter, referred to as rTOF) histograms, defined to be the difference between the predicted and measured values of the front-to-rear time-of-flight, were accumulated, and offsets were then chosen for each detector such that the peak channel was aligned on zero. Again, sample rTOF spectra are shown later in this article.

5. Front and rear veto/tagger array calibrations

The position and timing calibration of the front and rear veto/tagger array detectors consisted of three steps. Data for charged particle tracks acquired with the Charybdis magnet deenergized were employed for this calibration; hits were required in each layer of the front veto/tagger array, the front array, and the rear veto/tagger array.

First, as leading-edge discrimination was employed for these detectors, the algorithm began by computing corrections for walk. The relationship between the observed TDC and ADC channels, TDC_{obs} and ADC_{obs}, was parametrized

as $\mathrm{TDC_{obs}} = \mathrm{TDC} + \gamma \log(\mathrm{ADC_{obs}}/\mathrm{ADC_{peak}})$, where TDC denotes the TDC channel in the absence of walk effects, γ is an empirical parameter, and $\mathrm{ADC_{peak}}$ denotes the peak ADC channel. A value for γ was then computed via the method of least squares.

Second, the veto/tagger array detectors were position calibrated using a different algorithm than that employed for the position calibration of the front and rear array detectors because of the facts that the collimator partly obscured the edges of the front veto/tagger array detectors and that the outer rear veto/tagger array detectors did not receive adequate illumination from front-to-rear charged tracks. (The front and rear veto/tagger arrays were designed to provide more than adequate coverage of target-to-front and front-to-rear charged tracks.) As such, position calibration parameters for these detectors were deduced via a comparison of the recorded hit position with the nearest hit position in the front array, and offset parameters were determined via a χ^2 minimization of the difference between the predicted and recorded hit positions. To improve the statistics for the outer rear array veto/tagger detectors, the algorithm searched for (n, p) charge-exchange events in the front array. Tracks from these events were used to predict hit locations in the rear veto/tagger array detectors, and position calibration parameters were then deduced from another χ^2 minimization of the difference between the predicted and recorded hit positions. The resulting calibrated position spectra were well aligned about the physical center of each detector with somewhat more rounded spectra than observed in the front and rear array spectra because of the use of leading-edge discrimination.

Last, the mean times were aligned relative to each other via the same procedure employed for the mean-time calibration of all the other detectors.

D. Nucleon reconstruction and tracking

1. Overview of analysis code

The algorithm we developed for reconstruction and tracking in the neutron polarimeter began by translating the raw NPOL detector data decoded by ENGINE into hit positions and times. The code then attempted to determine which hit in the front array generated the trigger. All hits were then filtered according to a number of different selection criteria, with the surviving hits grouped into recognizable patterns. The code then attempted to determine the primary hits in the front and rear arrays and the charges of the incident particle and the particle detected in the rear array. Finally, kinematic quantities and time-of-flight variables were then computed for those events satisfying all tracking criteria.

2. Trigger selection and hit filtering

The algorithm assigned the location of the triggering front array hit to the detector with the smallest absolute self-timing value. All hits were then filtered according to a number of selection criteria designed to discard hits with unphysical reconstructed detector positions or mean times falling outside of specified windows. These mean-time windows were chosen sufficiently wide for purposes of quasielastic event selection, elastic/quasielastic scattering in the front array, and charged particle tagging in the veto/tagger arrays. In particular, the mean-time windows for both the front and rear veto/tagger arrays safely bracketed the entire peak regions with the borders extending into the regions of flat background.

3. Pattern grouping and track reconstruction

a. Incomplete and simple events. The algorithm began by identifying incomplete and simple events. First, events with either no surviving hits in the front and/or rear array or events with hits in both the top and bottom rear array were discarded. Second, simple events with exactly one hit in the front array, one hit in the rear array, and no hits in both the front and rear veto/tagger arrays were identified. For these events, the incident particle and the particle detected in the rear array were, obviously, designated neutral particles, and reconstruction of the track was deemed complete.

b. Multiple hit events. The majority of the events were more complicated than these simple events because of propagation of the recoil protons through adjacent scintillator bars or multiple scattering of the neutron. For these more complicated events, the code began by identifying which layer in the front array (i.e., first, second, third, or fourth) was hit first; henceforth, we refer to the hit(s) in this layer as the "first cluster." If the first cluster contained more than one hit, the (vertically) highest and lowest hits were identified; such hit patterns were assumed to be the result of an *np* or *pp* interaction in one detector followed by the penetration of the recoil proton into a vertically adjacent detector. Accordingly, if the hits occurred in noncontiguous detectors within the same vertical layer (i.e., existence of a vertical "gap"), the event was discarded.

The code then searched for evidence of one or more "missing layers" in the front array (e.g., an event with hits in the first layer and the fourth layer); a missing layer was taken to be evidence for multiple scattering of the incident neutron. If such a "second cluster" of hits was not found, the location of the front array scattering vertex was assigned to the highest (lowest) hit in the first cluster if the top (bottom) rear array recorded one or more hits. If, instead, a second cluster of hits was found, the code determined whether the second cluster contained a gap; again, events with gaps in the second cluster were discarded. The algorithm then attempted to discern whether the second cluster was located above or below the first cluster; if the second cluster was above (below) the first cluster, the location of the first cluster scattering vertex was assigned to the highest (lowest) hit in the first cluster. Then, if the top (bottom) rear array was hit, the location of the second cluster scattering vertex was assigned to the highest (lowest) hit in the second cluster. Finally, if more than one hit was recorded in either the top or bottom rear array, the rear array scattering vertex was assigned to that hit closest in distance to the final front array scattering vertex.

Illustrative examples of two possible types of reconstructed tracks are shown in Fig. 11. We note here, and discuss later in Sec. VE2, that events with a "second cluster" were reconstructed but were not used in our extraction of scattering asymmetries.

4. Charge identification

After the track through the front and rear arrays was reconstructed, the code then checked for hits in the veto/tagger

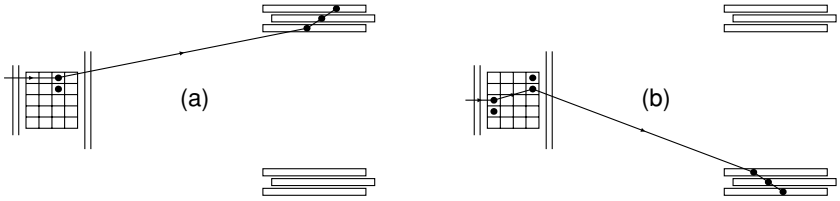

FIG. 11. Examples of reconstructed tracks for (a) an event with a single cluster in the front array, no missing layers, and multiple hits in the top rear array and (b) an event with two clusters in the front array (separated by two missing layers) and multiple hits in the bottom rear array.

arrays. The charge of the incident particle was determined via the following algorithm. (1) If there were no hits in any of the front veto/tagger detectors, the particle was designated a neutral particle. (2) If there were hits in the front veto/tagger detectors, the radial distance between the location of the veto/tagger hit and the location of the first scattering vertex was computed according to $d = \sqrt{(x_{\rm vt} - x_{\rm fr})^2 + (y_{\rm vt} - y_{\rm fr})^2}$, where the coordinates refer to the polarimeter basis, defined in Eq. (7). If at least one hit in each veto/tagger layer satisfied $d \leqslant 30$ cm, the incident particle was designated a charged particle. If no hits in either veto/tagger layer satisfied $d \leqslant 30$ cm, the incident particle was designated a neutral particle. Finally, if a hit in one of the front/veto tagger layers satisfied this distance requirement but no hits in the other layer satisfied this condition, the charge of the incident particle was declared to be ambiguous.

The algorithm for the determination of the charge of the particle detected in the rear array was essentially identical to that described above. The only difference was that the code predicted where the hits in the rear veto/tagger arrays should have occurred assuming a straight-line trajectory from the final front-array scattering vertex to the rear-array scattering vertex. The computed value of the radial distance between the location of the actual hit and the predicted hit was then used, in an identical manner, for rear-array neutral/charged tagging.

The choice of the 30-cm radial track-distance threshold was based on an examination of track-distance spectra for the front and rear veto/tagger arrays. The spectra for the front veto/tagger array were found to be relatively narrow with an abrupt change in slope around 30 cm, believed to be related to these scintillators' position resolution. The spectra for the rear veto/tagger array did not contain such a feature as the recoil protons arising from interactions in the front array were widely distributed in angle; nevertheless, the same 30-cm condition was employed as the position resolutions for these detectors were similar to those in the front veto/tagger array.

5. *Kinematic distributions and time-of-flight variables*

Following reconstruction of the track through the polarimeter, kinematic and time-of-flight quantities were computed for fully reconstructed events. First, the incident particle's momentum was computed using only position information for the reconstructed target vertex, position information for the first scattering vertex in the front array, and the four-momentum transfer $(\omega, \mathbf{q})$, via solution of the quadratic equation for $|\mathbf{p}_n|$ given previously in Eq. (17). The momentum was then used to predict the target-to-front array time-of-flight; the difference between the predicted and measured time-of-flight was then stored as the cTOF variable. Laboratory frame polar and azimuthal neutron scattering angles with respect to $\mathbf{q}$, θ_{nq} and ϕ_{nq}, were computed from information on $\mathbf{q}$ and $\mathbf{p}_n$. Second, front-to-rear polar and azimuthal scattering angles, $\theta_{\rm scat}$ and $\phi_{\rm scat}$, were computed using information on $\mathbf{p}_n$ and the scattering vertices in the front and rear arrays. This information was used to compute a value for T_{np}, Eq. (18), which was then used to predict the front-to-rear time-of-flight; the difference between the predicted and measured time-of-flight was then stored as the rTOF variable. Finally, the missing momentum, $\mathbf{p}_{\rm miss}$, missing energy, $E_{\rm miss}$, and missing mass, $m_{\rm miss}$, were computed according to

$$\mathbf{p}_{\rm miss} = \mathbf{q} - \mathbf{p}_n, \tag{19a}$$

$$E_{\rm miss} = (m_d + \omega) - (T_n + m_n), \tag{19b}$$

$$m_{\rm miss} = \sqrt{E_{\rm miss}^2 - |\mathbf{p}_{\rm miss}|^2}. \tag{19c}$$

6. *Sample nucleon reconstruction results*

To illustrate the full range of the polarimeter's acceptance, sample two-dimensional histograms of $|\mathbf{p}_{\rm miss}|$ plotted versus the invariant mass W at our $Q^2 = 1.136$ and 1.474 $(\mathrm{GeV}/c)^2$ points are shown in Fig. 12. A minimal set of cuts designed to eliminate scattering from the target cell walls, hadrons

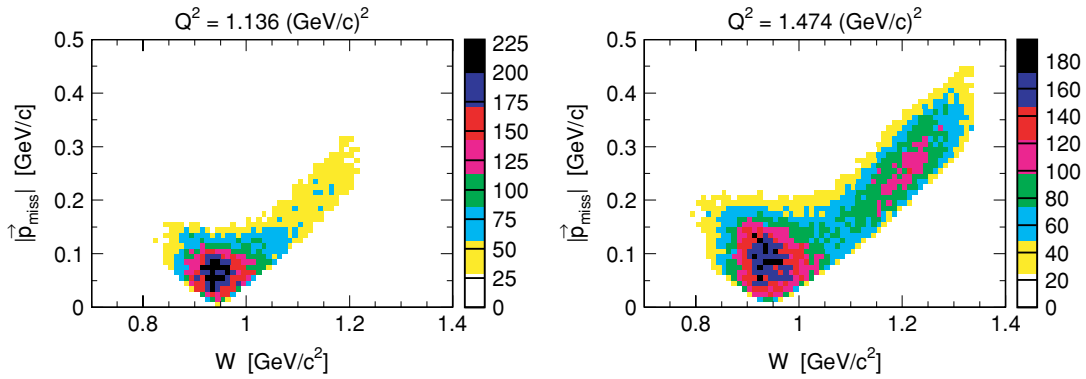

FIG. 12. (Color online) Correlation plot of $|\mathbf{p}_{\rm miss}|$ versus W for the full NPOL acceptance at $Q^2 = 1.136$ and 1.474 $(\mathrm{GeV}/c)^2$.

in the HMS, and protons incident on NPOL were applied to these spectra. Our acceptance was sensitive to missing momenta ranging up to ∼450 MeV/c at our highest Q^2 point. As can clearly be seen in these correlation plots, quasielastic events were associated with missing momenta in the range $\lesssim$150 MeV/c. Larger values of $|\mathbf{p}_{\rm miss}|$ are, of course, seen to correspond to inelastic events, with the $\Delta(1232)$ resonance prominent at large missing momenta in the $Q^2 = 1.474$ (GeV/c)^2 spectrum. The correlation plot for $Q^2 = 1.169$ (GeV/c)^2 was essentially identical to that at $Q^2 = 1.136$ (GeV/c)^2, whereas the $Q^2 = 0.447$ (GeV/c)^2 distribution was restricted to considerably smaller ranges of $|\mathbf{p}_{\rm miss}|$ ($\lesssim$100 MeV/c).

E. Data selection criteria, data sets, and cuts

1. Data selection criteria and data sets

Only those data runs satisfying the following criteria were employed for the final production data analysis: (1) no problems with the HMS equipment (e.g., magnet trips, detector failures, etc.), (2) no problems with delivery of the electron beam (e.g., unstable beam parameters), (3) no problems with the DAQ, (4) no problems with the cryogenic target (e.g., large temperature fluctuations, monitoring system failures, etc.), and (5) no problems with the Charybdis magnet or the NPOL detectors (e.g., fluctuations in the magnet current, detector high-voltage trips, etc.). We note that additional problems may have resulted in the designation of a run as unsuitable for the production analysis.

The quantity of data satisfying the above selection criteria is summarized in Table IV. There, we list the accumulated charge for each of the individual Q^2 points and neutron spin precession angles.

2. Cuts for extraction of time-of-flight spectra

A summary of the final set of cuts applied to the production data sets for extraction of the cTOF and rTOF time-of-flight spectra is as follows.

TABLE IV. Quantity of data (accumulated charge) employed for the final production analysis. A total of 194 Coulombs of charge was delivered to the experiment for production running with the deuterium target.

Central Q^2 [(GeV/c)^2]	Precession angle χ	Charge (Coulombs)
0.447	−40°	25.122
0.447	+40°	14.569
1.136	0°	27.587
1.136	−90°	4.701
1.136	+90°	4.158
1.169	−40°	7.006
1.169	+40°	6.321
1.474	0°	26.239
1.474	−90°	4.097
1.474	+90°	4.098
1.474	−40°	20.803
1.474	+40°	16.762
Total		161.463

(a) Target variables. Scattering from the target cell windows was suppresed via the requirement that the reconstructed target vertex lie within ±7 cm of the center of the target (for the 15-cm target) along the incident beamline. Further, events with unreasonable reconstructed values for $x'_{\rm tar}$ and $y'_{\rm tar}$ were discarded.

(b) HMS variables. The reconstructed electron track was required to fall within the the collimator acceptance, and events with unreasonably large track reconstruction χ^2 values were discarded. Hadrons in the HMS were suppressed via cuts on the number of Cerenkov photoelectrons and the energy deposition in the calorimeter. Events away from the quasielastic peak were suppressed via a tight $\Delta p/p \in [-3\%, +5\%]$ cut.

(c) NPOL variables. Software thresholds of 8 (20) MeVee designed to suppress low-energy backgrounds were applied to the front- (rear-) array pulse height distributions. Also, to suppress lower-energy neutrons originating from charge-exchange Pb(p, n) reactions in the lead curtain (discussed in more detail later), the mean times for front array hits were required to lie within a $[-5, 5]$ ns window, because of the expected degradation in the energy of the incident protons prior to the charge-exchange reaction. Events with more than one scattering vertex in the front array (i.e., existence of a second cluster) were discarded to eliminate the effects of depolarization following the first interaction in the front array.

The front-to-rear polarimeter scattering angle, $\theta_{\rm scat}$, was required to satisfy $\theta_{\rm scat} \in [5^\circ, 35^\circ]$ at $Q^2 = 0.447$ (GeV/c)^2 and $\in [5^\circ, 30^\circ]$ for the other Q^2 points. The lower cut of 5° eliminated unreasonably small scattering angles, whereas the upper cut of 30° or 35° was used to suppress zero (or negative) values of the analyzing power at larger scattering angles (as predicted by SAID [70]).

(d) $^2H(e, e'n)^1H$ reaction variables. Pion-production events were suppressed via tight cuts on the missing momentum and invariant mass of $|\mathbf{p}_{\rm miss}| \leqslant 100$ MeV/c and $W \leqslant 1.04$ GeV/c^2.

F. Extraction of time-of-flight spectra and scattering asymmetries

1. Polarimeter event types

An analysis code developed to extract the physical scattering asymmetries subjected each event to the cuts discussed previously. In addition, each event was also subjected to a more stringent test for the determination of the incident particle's charge. As we used single-hit TDCs, an early accidental hit in a front veto/tagger detector falling outside the mean-time window for the front veto/tagger array would have prevented that TDC from recording any later (on-time) hits, leading to the incorrect tagging of a charged particle as a neutral particle.

Histograms of cTOF were accumulated for two types of front-array scattering events, (n, n) and (n, p) events, corresponding (for a neutral particle incident on the polarimeter) to the detection of a neutral and charged particle, respectively, in the rear array. We identified (n, n) events with the scattering of the neutron from the front array to the rear array, whereas we identified (n, p) events with forward scattering of the recoil proton with sufficient energy for penetration of the front array. It should be noted that for the incident neutron kinetic energies

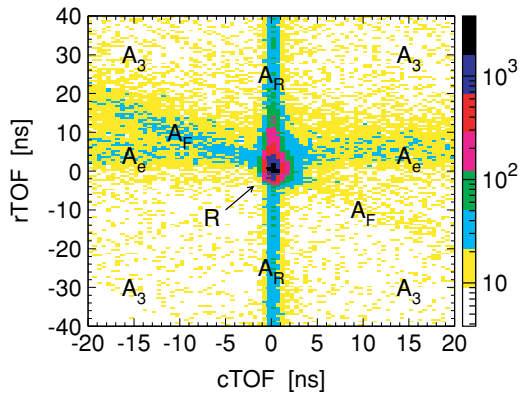

FIG. 13. (Color online) Correlation between cTOF and rTOF at $Q^2 = 1.474$ (GeV/c)^2 with the various event types (see text) identified.

of interest, the analyzing power for elastic np scattering becomes negative for neutron scattering angles greater than $\sim 40^\circ$; therefore, the signs of the detected asymmetries for (n, n) and (n, p) events were the same. Events with charges deemed ambiguous in either the front or rear array were rejected.

Histograms of rTOF summed over all front-to-rear tracks were accumulated for those events falling within a prescribed cTOF window. To compensate for variations in the flight path between the front array and the rear array, the rTOF values were normalized to a nominal 250-cm flight path. The accumulated rTOF spectra were decomposed into the following event types: (1) "RU events" (positive beam helicity and scattering from the front array to the top rear array), (2) "LU events" (negative beam helicity, top rear array), (3) "RD events" (positive beam helicity, bottom rear array), and (4) "LD events" (negative beam helicity, bottom rear array). The scattering asymmetries were then extracted from the yields in these four spectra.

2. HMS-NPOL coincidence event types

A two-dimensional histogram of the correlation between cTOF and rTOF summed over (n, n) and (n, p) events at $Q^2 = 1.474$ (GeV/c)^2 is shown in Fig. 13.

Five different event types can readily be identified in this correlation plot. (1) Real threefold HMS/front-array/rear-array coincidence events are denoted with R and form the peak centered at cTOF = rTOF = 0 ns. (2) Threefold accidental coincidences, denoted with A_3, require a random electron in the HMS, a random neutral particle in the front array, and a random particle in the rear array, and are distributed uniformly over the entire plot area. (3) Real twofold front-array/rear-array coincidences with an accidental electron are denoted with A_e and are associated with the "horizontal band" defined by rTOF = 0 ns. (4) Real twofold electron/front-array coincidences with an accidental rear array particle are denoted with A_R and are identified with the "vertical band" defined by cTOF = 0 ns. (5) Real twofold electron/rear-array coincidences with an accidental front-array particle are denoted with A_F. These events are located along a diagonal band defined (approximately) by cTOF = $-$rTOF. Such events are attributed to the corruption of an otherwise R-type event by an accidental front array hit occuring some time Δt_A before or after the true interaction. The values of cTOF and rTOF extracted from the data will then be $\text{cTOF} = \text{cTOF}_{\text{uncorr}} - \Delta t_A$ and $\text{rTOF} = \text{rTOF}_{\text{uncorr}} + \Delta t_A$, where the subscript "uncorr" denotes the (true) uncorrupted values. For uncorrupted values centered on zero, it then follows that cTOF = $-$rTOF, in accordance with the observed result.

3. Quasielastic event selection

Real R-type coincidence events were selected via tight cTOF $\in [-1, 1]$ ns and rTOF $\in [-1, 8]$ ns cuts. As evidence our cuts selected quasielastic $^2\text{H}(e, e'n)^1\text{H}$ events, comparisons of invariant mass spectra, W, obtained before and after cuts on $\Delta p/p$, $|\mathbf{p}_{\text{miss}}|$, and cTOF are shown in Fig. 14 for our $Q^2 = 1.136$ and 1.474 (GeV/c)^2 points. After all cuts (except for the additional cut on $W < 1.04$ GeV/c^2 itself), these distributions converged to fairly narrow peaks centered on the neutron mass.

4. Extraction of asymmetries from time-of-flight spectra

One-dimensional projections of cTOF are shown in Fig. 15 for our lowest and highest Q^2 points. Histograms of rTOF were accumulated for those events falling within the $[-1, 1]$ ns peak cTOF window. In addition, histograms of rTOF

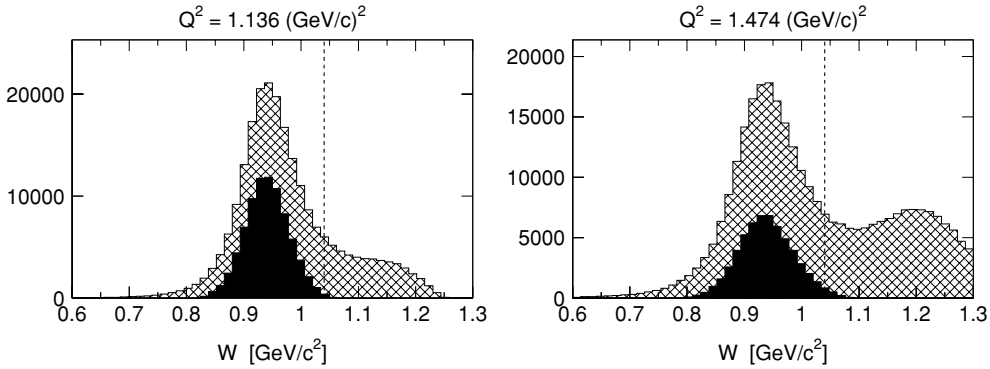

FIG. 14. Distributions of the invariant mass W before (cross-hatched) and after (solid) all cuts except for those on $\Delta p/p$, $|\mathbf{p}_{\text{miss}}|$, and cTOF at $Q^2 = 1.136$ and 1.474 (GeV/c)^2. The vertical dashed lines denote the final $W < 1.04$ GeV/c^2 cut.

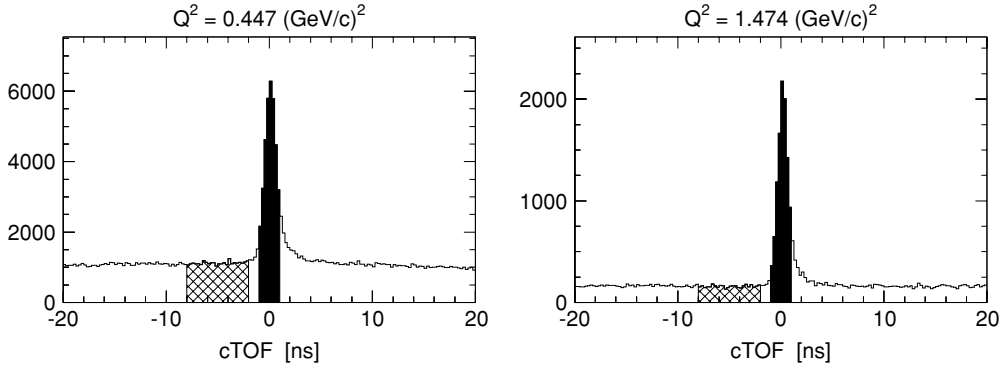

FIG. 15. Distributions of cTOF after application of the final set of cuts at $Q^2 = 0.447$ and 1.474 (GeV/c)^2. The dark shaded regions indicate the selected peak window, whereas the cross-hatched regions indicate the sampled background region.

were accumulated also for a sampled background region of $[-8, -2]$ ns in the cTOF spectrum. The signal-to-noise ratios were independent of the state of the Charybdis magnet at each of our Q^2 points.

Sample rTOF spectra summed over all RU, LU, RD, and LD events for cTOF peak events at our lowest and highest Q^2 points are shown in Fig. 16. The asymmetric tails on the slow sides are because of scattering from protons bound in carbon nuclei and other nuclear reactions, and the small satellite peak observed in the $Q^2 = 1.474$ (GeV/c)^2 spectrum on the fast side at ~ -2.5 ns is attributed to quasifree π^0 production in the scintillators, followed by decay and detection of a photon in the rear array. Indeed, front-to-rear velocity spectra for these events are centered on c. This π^0-production peak was observed in the $Q^2 = 1.136$, 1.169, and 1.474 (GeV/c)^2 rTOF spectra but was absent in the $Q^2 = 0.447$ (GeV/c)^2 spectrum, as the energies of those neutrons were below threshold.

The yields for those events falling within the $[-1, 8]$ ns rTOF window were obtained via peak fitting, with contributions from the π^0-production peak and the flat background excluded. These yields were then further corrected for the contents of the rTOF spectra accumulated for the sampled cTOF background region. The desired quantities, the physical scattering asymmetries, ξ, were extracted from the final background-subtracted yields in the four decomposed rTOF spectra via the cross-ratio technique [71]. In obvious notation, the cross ratio, r, is defined to be the ratio of two geometric means,

$$r = \sqrt{\frac{N_{RU} N_{LD}}{N_{RD} N_{LU}}}, \tag{20}$$

and is related to the asymmetry ξ via

$$\xi = \frac{r-1}{r+1} = \frac{\sqrt{N_{RU} N_{LD}} - \sqrt{N_{RD} N_{LU}}}{\sqrt{N_{RU} N_{LD}} + \sqrt{N_{RD} N_{LU}}}. \tag{21}$$

The merit of the cross-ratio technique is that ξ is insensitive to [71] (1) the number of particles incident on the polarimeter (i.e., target luminosities) for the two beam helicity states and (2) the relative efficiencies and acceptances of the polarimeter's top and bottom rear arrays.

G. Asymmetry results

1. Electron beam polarization normalization

Unlike recoil polarization measurements in which both polarization components, $P_t^{(h)}$ and $P_\ell^{(h)}$, can be extracted simultaneously from the data (e.g., recoil polarization experiments with focal-plane polarimeters), our polarimeter was sensitive to only one of these components (or a combination thereof). As such, it was necessary to normalize our run-by-run

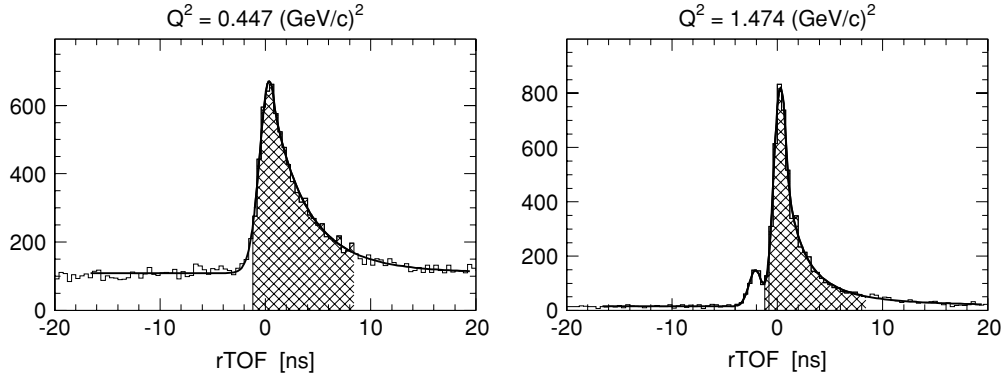

FIG. 16. Distributions of rTOF for cTOF peak events at $Q^2 = 0.447$ and 1.474 (GeV/c)^2. The cross-hatched regions indicate the accepted window. The solid curves are the results of our fits to these spectra.

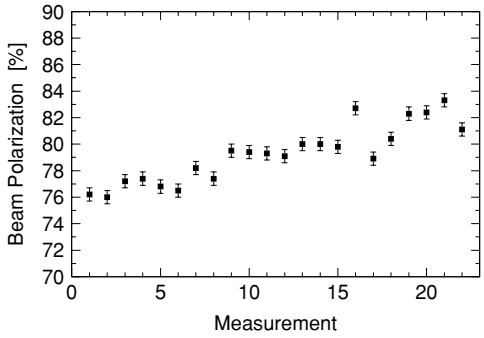

FIG. 17. Results of 23 successive Møller beam-polarization measurements conducted during the $Q^2 = 1.474\ (\mathrm{GeV}/c)^2\ \chi = \pm 40^\circ$ running period spanning the days of February 20, 2001, through March 5, 2001. The errors shown are statistical.

scattering asymmetries to some common value of the beam polarization.

Our normalization procedure was as follows. As the beam polarization was measured only periodically with the Møller polarimeter, we defined the beam polarization for a run to be the result of the most recent prior Møller measurement (if the accelerator parameters were unchanged in the interim). All of our run-by-run scattering asymmetries and their statistical errors were then normalized to a common value of 80%.

We found that the beam polarization was fairly stable, with small (few percentages) fluctuations observed in successive measurements during periods of continuous beam delivery to our experiment. To illustrate, the results of 23 successive Møller measurements conducted during our $Q^2 = 1.474\ (\mathrm{GeV}/c)^2\ \chi = \pm 40^\circ$ running period spanning the days of February 20, 2001, through March 5, 2001, are shown in Fig. 17.

2. Corrections for charge-exchange in the lead curtain

Contamination from the two-step $^2\mathrm{H}(\vec{e}, e'\vec{p})$+Pb$(\vec{p}, \vec{n})$ charge-exchange reaction in the lead curtain could either dilute the "real" $^2\mathrm{H}(\vec{e}, e'\vec{n})$ asymmetry or contribute to a false asymmetry if the flux of charge-exchange neutrons was unpolarized or polarized, respectively. A significant advantage of our neutron flight path setup in which the lead curtain was located downstream of the Charybdis dipole field was that the majority of the quasielastic protons were swept from the front face of the lead curtain.

Accounting for such nuclear reactions, the measured asymmetry, ξ_M, can be parametrized as

$$\xi_M = f_R \xi_R + f_B \xi_B, \tag{22}$$

where f_B denotes the contamination level from the two-step charge-exchange process, ξ_B denotes the asymmetry for charge-exchange neutrons, $f_R = 1 - f_B$ denotes the fraction of $^2\mathrm{H}(\vec{e}, e'\vec{n})$ neutrons, and ξ_R denotes the asymmetry for the $^2\mathrm{H}(\vec{e}, e'\vec{n})$ reaction. The asymmetry for the background process can further be written as

$$\xi_B = \left(P_S^p \cos\chi_p + P_L^p \sin\chi_p\right) D_{SS}^{\mathrm{Pb}} A_y, \tag{23}$$

where P_S^p and P_L^p denote, respectively, the projections of the $^2\mathrm{H}(\vec{e}, e'\vec{p})$ recoil proton's polarization on the polarimeter momentum basis $\hat{S}$ and $\hat{L}$ axis; χ_p is the proton spin precession angle in the Charybdis field; and D_{SS}^{Pb} denotes the polarization transfer coefficient for the Pb$(\vec{p}, \vec{n})$ reaction. It then follows that if f_B, P_S^p, P_L^p, χ_p, D_{SS}^{Pb}, and A_y are all known or measured, ξ_R can be determined.

To estimate the contamination levels, f_B, we took data with a liquid hydrogen target. The rates for (n, n) and (n, p) events extracted from these data were compared with those extracted from our liquid deuterium data and corrected for differences in the two targets' densities and atomic numbers. We found that the contamination levels were negligible ($\lesssim 0.3\%$) at all of our Q^2 points when the Charybdis field was energized for $\chi = \pm 40^\circ$ and $\pm 90^\circ$ precession and also when the field was deenergized at $Q^2 = 1.136\ (\mathrm{GeV}/c)^2$ for $\chi = 0^\circ$ precession; therefore, we did not apply corrections to any of these asymmetries. Nonnegligible event rates were observed when the Charybdis field was deenergized for $\chi = 0^\circ$ precession at $Q^2 = 1.474\ (\mathrm{GeV}/c)^2$, with observed contamination levels of $\sim 2.2\%$ and $\sim 4.2\%$ for (n, n) and (n, p) events, respectively. Corrections were applied to these asymmetries assuming $D_{SS}^{\mathrm{Pb}} = 0$ for our kinematics of $T_p \sim 786$ MeV. D_{SS}^{Pb} was measured at $T_p = 795$ MeV and found to be consistent with zero (0.014 ± 0.013) [72].

3. Summary of asymmetry results

Our final asymmetry data for (n, n) and (n, p) events at each of our Q^2 points and precession angles are tabulated in Table V. To illustrate the quality of our asymmetry data, a histogram of the (n, n) asymmetries for the $Q^2 = 1.136\ (\mathrm{GeV}/c)^2\ \chi = 0^\circ$ data set is shown in Fig. 18; the distribution is of an appropriate Gaussian shape.

H. Extraction of uncorrected values for G_{En}/G_{Mn}

We extracted values for G_{En}/G_{Mn} from our asymmetry data assuming elastic scattering from a free neutron and infinitesimal pointlike HMS and NPOL acceptances and

TABLE V. Final (n, n) and (n, p) asymmetry data normalized to a beam polarization of 80%. The $Q^2 = 1.474\ (\mathrm{GeV}/c)^2\ \chi = 0^\circ$ asymmetries were corrected for contamination from charge-exchange in the lead curtain.

Central Q^2 $[(\mathrm{GeV}/c)^2]$	Precession angle χ	(n, n) ξ [%]	(n, p) ξ [%]
0.447	-40°	-4.51 ± 0.22	-2.97 ± 0.19
0.447	$+40^\circ$	6.38 ± 0.28	4.98 ± 0.29
1.136	0°	1.20 ± 0.13	0.57 ± 0.10
1.136	-90°	-5.71 ± 0.32	-3.11 ± 0.25
1.136	$+90^\circ$	5.67 ± 0.35	3.18 ± 0.25
1.169	-40°	-2.92 ± 0.29	-1.42 ± 0.22
1.169	$+40^\circ$	4.75 ± 0.31	2.76 ± 0.25
1.474	0°	1.29 ± 0.19	0.64 ± 0.17
1.474	-40°	-2.26 ± 0.20	-0.88 ± 0.18
1.474	$+40^\circ$	4.03 ± 0.24	2.11 ± 0.21
1.474	-90°	-4.64 ± 0.47	-2.92 ± 0.50
1.474	$+90^\circ$	5.07 ± 0.49	2.14 ± 0.43

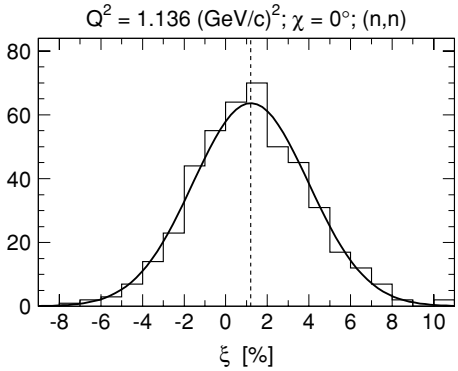

FIG. 18. Histogram of the $Q^2 = 1.136$ (GeV/c)^2 $\chi = 0^\circ$ (n, n) asymmetries. The solid curve is a Gaussian fit, and the vertical dashed line denotes the mean value for the asymmetry given in Table V.

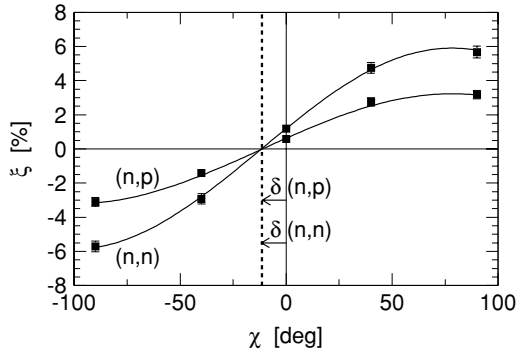

FIG. 19. Sinusoidal fits of the $Q^2 = 1.136/1.169$ (GeV/c)^2 (n, n) and (n, p) asymmetries as a function of the precession angle.

neglecting nuclear physics corrections for FSI, MEC, and IC. To do so, we fitted the asymmetries as a function of the precession angle to the functional form $\xi(\chi) \propto \sin(\chi + \delta)$, where the phase-shift parameter $\delta = \tan^{-1}(P_t^{(h)}/P_\ell^{(h)})$ was defined in terms of form factors and kinematics in Eq. (4). To illustrate the quality of these fits, our $Q^2 = 1.136/1.169$ (GeV/c)^2 (n, n) and (n, p) asymmetry data are plotted as a function of the precession angle in Fig. 19. These data are fitted well by sinusoids with excellent agreement seen between the independent fits to the (n, n) and (n, p) asymmetry data. We could not fit the $Q^2 = 0.447$ (GeV/c)^2 asymmetries to a sinusoid as asymmetry data were taken only at two precession angles.

The values for G_{En}/G_{Mn} we derived from our values for δ using the nominal (central) values for the kinematics listed in Table II are summarized in Table VI.

I. Simulation programs

We developed two independent simulation programs, GENGEN and the ACCEPTANCE program, to extract acceptance-averaged and nuclear physics-corrected values for G_{En}/G_{Mn} from our measured experimental asymmetries. The GENGEN simulation program, a pure Monte Carlo simulation program, included realistic models for the primary $^2\mathrm{H}(\vec{e}, e'\vec{n})^1\mathrm{H}$ reaction in the target, the HMS acceptance, neutron spin precession in the Charybdis dipole field, spin-dependent neutron scattering in the lead curtain, elastic and quasielastic np scattering in the front and rear arrays of NPOL, tracking of the incident neutron and recoil proton from the front array to the rear array, and the detector response of the polarimeter to np interactions in the front and rear array. The ACCEPTANCE program was not a Monte Carlo simulation program, but was, instead, designed to extract the corrections for the finite experimental acceptance and nuclear physics effects directly from our experimental data.

1. GENGEN simulation program

a. Event sampling technique. A uniform sampling scheme was employed in which events were generated uniformly over the available kinematic phase space, with an event weight computed according to a model cross section. The vertex position for the primary $^2\mathrm{H}(\vec{e}, e'\vec{n})^1\mathrm{H}$ interaction in the extended target was sampled uniformly within the raster pattern, and the scattered electron's kinematics were sampled uniformly over specified ranges. The physical acceptance of the HMS was enforced via inclusion of an HMS transport model taken from the SIMC simulation code [73]. In-plane and out-of-plane scattering angles for the recoil neutron were sampled uniformly over specified ranges, permitting computation of the magnitude of the neutron's momentum according to Eq. (17). Complete specification of the electron and neutron kinematics permitted computation of those variables of particular interest for the quasielastic $^2\mathrm{H}(e, e'n)^1\mathrm{H}$ reaction, such as $\Theta_{np}^{\mathrm{c.m.}}$, $\mathbf{p}_{\mathrm{miss}}$, and so on.

b. Cross section and recoil polarization. We employed the Arenhövel formalism [19,20] for computation of the $^2\mathrm{H}(\vec{e}, e'\vec{n})^1\mathrm{H}$ differential cross section and recoil polarization. These calculations modeled the deuteron as a nonrelativistic n-p system and employed the Bonn R-space NN potential [74] for the deuteron wave function and the inclusion of FSI; further, leading-order relativistic contributions (RC) to the

TABLE VI. Values of $\delta = \tan^{-1}(P_t^{(h)}/P_\ell^{(h)})$ and the uncorrected results for G_{En}/G_{Mn} at each of the Q^2 points.

Central Q^2 [(GeV/c)^2]	δ [deg]		G_{En}/G_{Mn}		G_{En}/G_{Mn} combined[a]
	(n, n)	(n, p)	(n, n)	(n, p)	
0.447	8.2 ± 1.5	12.0 ± 1.9	-0.0580 ± 0.0106	-0.0854 ± 0.0138	-0.0681 ± 0.0084
1.136/1.169[b]	11.7 ± 1.2	11.2 ± 1.7	-0.124 ± 0.013	-0.118 ± 0.019	-0.122 ± 0.011
1.474	14.0 ± 1.6	16.9 ± 2.9	-0.166 ± 0.020	-0.203 ± 0.037	-0.174 ± 0.017

[a]Weighted average of G_{En}/G_{Mn} from (n, n) and (n, p) events.
[b]Result obtained via averaging of the nominal (central) electron kinematics for the two Q^2 points.

wave functions and one-body current were added via inclusion of the most important kinematic part of the wave function boost. In the current operator, explicit MEC contributions beyond the Siegert operators (essentially from π and ρ exchange) and IC were included. The treatment of IC permitted consideration of kinematic regions away from the quasielastic ridge and excitations up to the Δ region.

Acceptance-averaging of those calculations performed within the Born approximation (hereafter, termed the PWBA model) permitted extraction of the corrections for the finite experimental acceptance (over the pointlike results discussed in Sec. VH), whereas averaging of the full calculations that included FSI, MEC, IC, and RC (hereafter, termed the FSI+MEC+IC+RC model) permitted application of corrections for nuclear physics effects. To implement the Arenhövel formalism within GENGEN, lookup tables for the structure functions for the $^2\mathrm{H}(\vec{e}, e'\vec{n})^1\mathrm{H}$ reaction were constructed over a sufficiently dense kinematic grid indexed by $(E_{e'}, \theta_{e'}, \Theta_{np}^{\mathrm{c.m.}})$, and tricubic spline interpolation among the grid elements was used to compute the cross section and recoil polarization for the kinematics of each simulated event according to the formalism outlined in Appendix A.

c. Nucleon form factors. All of the structure function calculations assumed the dipole parametrization for G_{Mn}, G_{Ep}, and G_{Mp}. For the form factor of interest, G_{En}, the structure function calculations were first performed for various multiplicative factors of the standard Galster parametrization, $G_{En} = -S\mu_n\tau G_D/(1 + 5.6\tau)$, where the scale factor $S \in \{0.50, 0.75, 1.00, 1.25, 1.50\}$. To investigate the influence of a different Q^2 dependence for G_{En}, structure function calculations were performed also for multiplicative factors of a modified Galster parametrization, $G_{En} = -Sa\mu_n\tau G_D/(1 + b\tau)$, with $a = 0.894$, $b = 3.55$ (which choice will be explained later), and the same set of S factors.

d. Charybdis field transport. The recoil polarization was transported point by point through a grid of the Charybdis field, with the time derivative of the spin vector computed at each grid point according to standard relativistic electrodynamics. The precession angle was computed from information on the initial and final spatial orientations of the spin vector.

e. Lead curtain interactions. Neutron interactions in the lead curtain were simulated with a spin-dependent multiple-scattering algorithm that employed quasifree scattering from a lead nucleus modeled as a Fermi gas, with the Fermi momentum for ^{208}Pb taken to be 265 MeV/c [2]. The probability for an interaction of the neutron with a lead nucleus was determined via interpolation (or extrapolation) of existing data on total n + Pb cross sections [75]. A polar scattering angle was sampled from cumulative probability distributions for the polar scattering angle as a function of neutron energy, and an azimuthal scattering angle was chosen via an acceptance-rejection algorithm for the spatial scattering asymmetry resulting from nonzero analyzing power. Pauli blocking was enforced. For those neutrons suffering an interaction, the scattered neutron's and recoil nucleon's polarization components were constructed via computation of the depolarization and polarization-transfer tensors for *NN* scattering using helicity amplitude routines obtained from SAID [70].

f. Polarimeter interactions. Finally, following (successful) transport of the neutron through the steel collimator into the front array, interactions in NPOL were simulated. A scattering vertex was chosen randomly assuming a fixed value for the mean free path of neutrons in the plastic scintillator, and both the elastic (scattering from free protons) and quasielastic (scattering from protons bound in carbon nuclei) channels were simulated. The scattering angles in the polarimeter were determined using the same algorithms employed for *NN* scattering in the lead curtain. We employed a rather simple model for the propagation of the recoil proton, with the energy deposition and range (assuming a straight-line trajectory) computed according to the Cecil, Anderson, and Madey [76] range-energy formulas for protons in the hydrocarbon scintillator.

2. GENGEN performance

A rigorous and reliable extraction of the corrections for the finite experimental acceptance and nuclear physics effects from simulated data is feasible if the simulated acceptance reasonably matches the experimental acceptance; therefore, we now document the performance of GENGEN by comparing (1) simulated distributions of important kinematic quantities with those derived from experimental data and (2) the behavior of the acceptance-averaged simulated polarizations and the experimental asymmetries as a function of the cut on some kinematic variable (here, taken to be the invariant mass W).

a. Kinematic distributions. Sample comparisons of experimental and simulated kinematic distributions of two important kinematic variables, W and $|\mathbf{p}_{\mathrm{miss}}|$, are shown in Figs. 20 and 21. Reasonable agreement is seen between the GENGEN distributions and those extracted from experimental data. Although not shown here, reasonable agreement was also obtained between simulated and experimental distributions of variables related to *np* scattering in NPOL (e.g., scattering angles, velocity spectra, etc.).

b. Experimental asymmetries and simulated polarizations. A sample comparison of the behavior of the experimental asymmetries and acceptance-averaged simulated polarizations following transport through the Charybdis dipole field is shown in Fig. 22. There, we plot the ratio of the experimental asymmetries to the simulated polarizations as a function of the upper cut on W for (n, p) events and $\chi = -40^\circ$ precession at our $Q^2 = 1.169$ (GeV/c)^2 point. Within statistical errors, the experimental asymmetries and simulated polarizations are seen to scale similarly with the cut on W. Similar results were observed for our other Q^2 points and precession angles.

It should be noted that in this figure the simulated acceptance-averaged polarizations were computed assuming some certain parametrization for G_{En} (here, the Galster parametrization); therefore, the ratios of the asymmetries to the simulated polarizations shown in this figure are not equivalent to the polarimeter's analyzing power.

3. ACCEPTANCE program

The ACCEPTANCE program was developed as an alternative to the GENGEN Monte Carlo simulation program. This program used the kinematics of the reconstructed quasielastic events from the actual experimental data to compute, on an

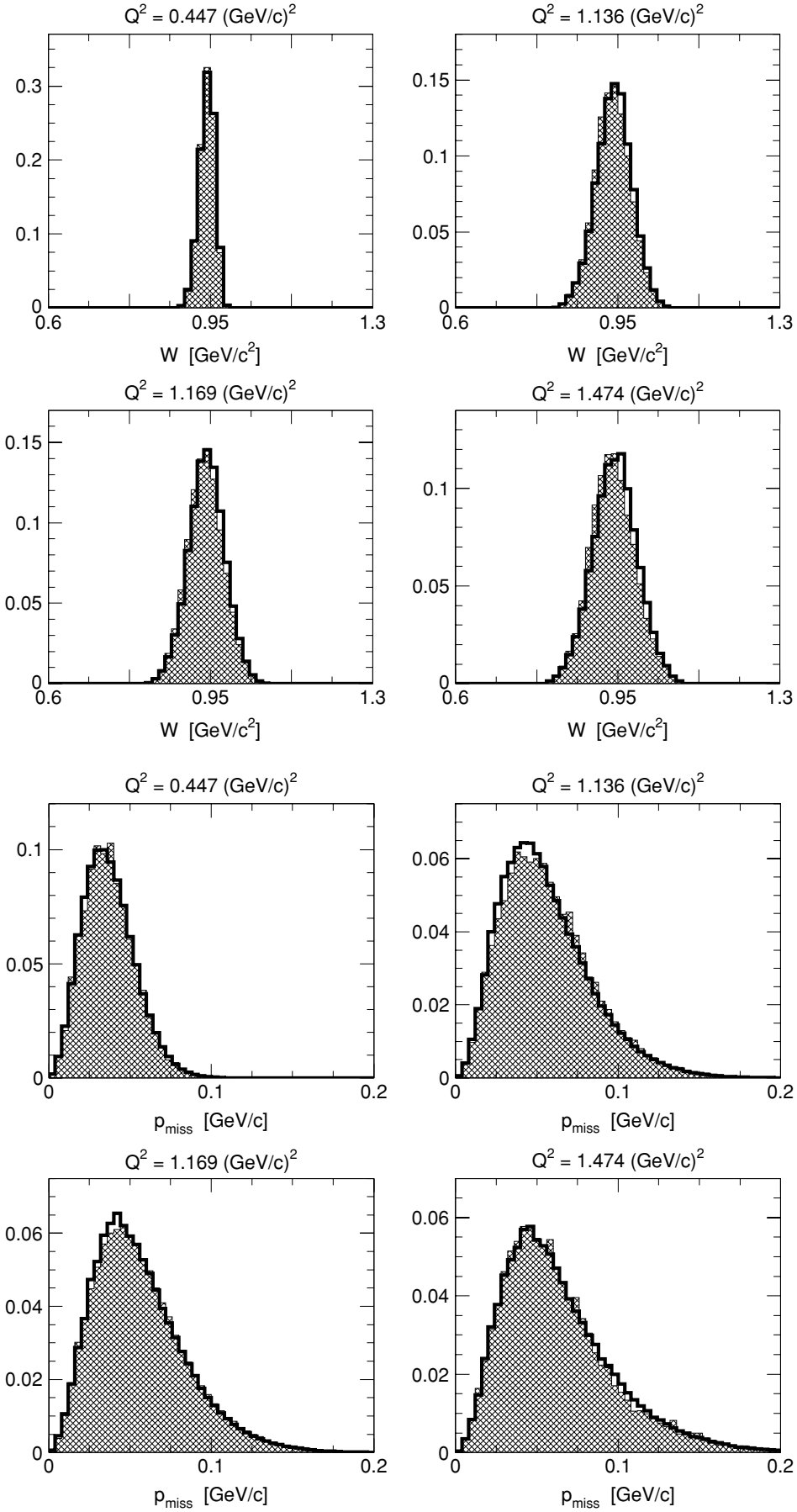

FIG. 20. Comparison of GENGEN simulated (unfilled histograms with thick solid line borders) and experimental (cross-hatched filled histograms) distributions of W for the four central Q^2 points. Identical cuts were applied to both the simulated and experimental data. The simulated results shown here employed the FSI+MEC+IC+RC model and the Galster parametrization for G_{En}.

FIG. 21. Comparison of GENGEN simulated (unfilled histograms with thick solid line borders) and experimental (cross-hatched filled histograms) distributions of $|\mathbf{p}_{\rm miss}|$ for the four central Q^2 points. Identical cuts were applied to both the simulated and experimental data. The simulated results shown here employed the FSI+MEC+IC+RC model and the Galster parametrization for G_{En}.

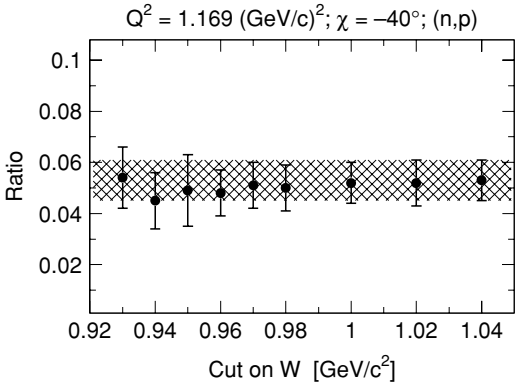

FIG. 22. Ratio of the asymmetries extracted from the experimental data to the GENGEN simulated polarizations as a function of the cut on W for (n, p) events and $\chi = -40^\circ$ precession at our $Q^2 = 1.169\ (\mathrm{GeV}/c)^2$ point. The shaded band indicates the statistical error on the ratio for the nominal cut on W of $<1.04\ \mathrm{GeV}/c^2$. The simulated results shown here employed the FSI+MEC+IC+RC model and the Galster parametrization for G_{En}.

event-by-event basis, the recoil polarization presented to the polarimeter for each event employed in our final data analysis (i.e., for those events satisfying all final analysis cuts). The ACCEPTANCE program used the same $^2\mathrm{H}(\vec{e}, e'\vec{n})^1\mathrm{H}$ interpolation and Charybdis spin transport algorithms developed for GENGEN. Although the ACCEPTANCE program was, technically, not a true Monte Carlo simulation, a significant advantage of this method was that it did not require a model for the experimental acceptance; however, the disadvantage of this method was that the reconstruction of the event-by-event kinematics is, of course, subject to measurement uncertainties, leading to uncertainties in the computation of the recoil polarization.

VI. FINAL RESULTS FOR G_{En}/G_{Mn} AND G_{En}

A. Distributions of $\Theta_{np}^{\mathrm{c.m.}}$

Distributions of $\Theta_{np}^{\mathrm{c.m.}}$ for those events surviving all analysis cuts at our lowest Q^2 point are shown in Fig. 23. The majority of the accepted events are seen to fall within $\sim$10–15° of perfect quasifree emission. The distributions of $\Theta_{np}^{\mathrm{c.m.}}$ at our other Q^2 points are similar but are restricted to somewhat smaller ranges, $170^\circ < \Theta_{np}^{\mathrm{c.m.}} < 180^\circ$.

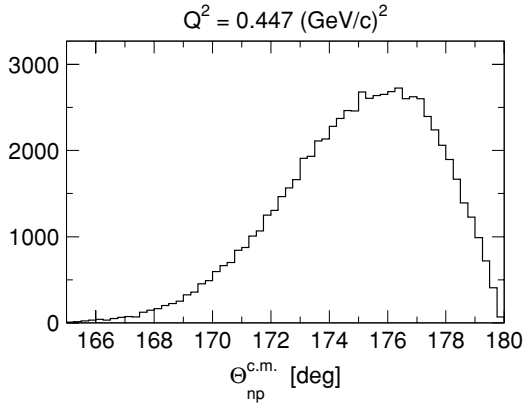

FIG. 23. Distributions of $\Theta_{np}^{\mathrm{c.m.}}$ after application of the final set of analysis cuts at $Q^2 = 0.447\ (\mathrm{GeV}/c)^2$.

Even for perfect quasifree emission, $\Theta_{np}^{\mathrm{c.m.}} = 180^\circ$, the PWBA and FSI+MEC+IC+RC calculations of the $P_t^{(h)}/P_\ell^{(h)}$ polarization ratio differ by 4.2% for the central kinematics of our lowest $Q^2 = 0.447\ (\mathrm{GeV}/c)^2$ point and 1.6% at our highest $Q^2 = 1.474\ (\mathrm{GeV}/c)^2$ point. As the differences between the PWBA and FSI+MEC+IC+RC calculations increase away from $\Theta_{np}^{\mathrm{c.m.}} = 180^\circ$, these numbers provide essentially lower bounds for the expected magnitude of corrections for nuclear physics effects.

B. Extraction of acceptance-averaged and nuclear physics-corrected values for G_{En}/G_{Mn}

1. Overview of acceptance-averaging analysis procedure

The recoil polarization component we were interested in was the projection of the polarization vector on the polarimeter momentum basis $\hat{S}$ axis following transport through the Charybdis field and the lead curtain. We denote this polarization component as P'_S, where the prime denotes transport through the dipole field and lead curtain. Acceptance-averaged and nuclear physics-corrected values for G_{En}/G_{Mn} were extracted from our experimental asymmetries and simulations at each Q^2 point via the following procedure:

(i) Acceptance-averaged polarizations $\langle P'_S \rangle$ computed according to the PWBA and FSI+MEC+IC+RC models were extracted from simulated data for each precession angle at each Q^2 point and for each scale factor S of the Galster parametrization (see Sec. VI1).

(ii) In our "pairwise analysis method," for each S factor, we compared the ratio of the experimental asymmetries to the ratio of the simulated polarizations for the different precession angle combinations (i.e., $\chi = 0^\circ, \pm 90^\circ$ and $\chi = \pm 40^\circ$) and then computed a χ^2 value for each precession angle combination and each event type [i.e., (n, n) or (n, p) events] according to

$$\chi^2 = \frac{(\eta_{\mathrm{sim}} - \eta_{\mathrm{exp}})^2}{(\Delta\eta_{\mathrm{sim}})^2 + (\Delta\eta_{\mathrm{exp}})^2}, \tag{24}$$

where $\eta_{\mathrm{sim}} = \langle P'_S(0^\circ) \rangle / \langle P'_S(\pm 90^\circ) \rangle$ for the $\chi = 0^\circ$, $\pm 90^\circ$ precession angle combination and $\langle P'_S(-40^\circ) \rangle / \langle P'_S(+40^\circ) \rangle$ for the $\chi = \pm 40^\circ$ precession angle combination. The expressions for η_{exp} are identical, with the acceptance-averaged polarizations replaced by the experimental asymmetries. $\Delta\eta_{\mathrm{sim}}$ and $\Delta\eta_{\mathrm{exp}}$ denote the statistical errors. The resulting χ^2 values were fitted as a function of the scale factor S to a parabolic function, with the optimal value of S defined by the zero of the parabolic fitting function.

(iii) In our "global analysis method," we compared the experimental asymmetries with the simulated polarizations via minimization of a global χ^2 value computed according to

$$\chi^2\left(A_y^{(n,n)}, A_y^{(n,p)}\right) = \sum \frac{\left(\xi - A_y^{(n,n),(n,p)} \langle P'_S \rangle\right)^2}{(\Delta\xi)^2 + (\Delta\langle P'_S \rangle)^2}. \tag{25}$$

Here, the sum runs over all 10 asymmetries, ξ, and simulated polarizations, $\langle P'_S \rangle$, for each Q^2 point [i.e., five different precession angles, and (n, n) and (n, p) events], and $A_y^{(n,n)}$ and $A_y^{(n,p)}$ denote the polarimeter's analyzing power for (n, n) and (n, p) events. $\Delta\xi$ and $\Delta\langle P'_S \rangle$ denote the statistical errors. In this analysis, the analyzing powers and scale factor S were treated as free parameters, with the optimal values extracted from the minimal χ^2 value.

We note that the simulation statistical errors were generally an order of magnitude smaller than the experimental statistical errors.

2. Acceptance-averaged values of Q^2

The acceptance-averaged values of Q^2, denoted $\langle Q^2 \rangle$, were determined to be $\langle Q^2 \rangle = 0.447$, 1.126, 1.158, and 1.450 $(\mathrm{GeV}/c)^2$ for the central $Q^2 = 0.447$, 1.136, 1.169, and 1.474 $(\mathrm{GeV}/c)^2$ points, respectively. The distribution of Q^2 values for the $\langle Q^2 \rangle = 0.447\,(\mathrm{GeV}/c)^2$ point was sharply peaked around the central value of $0.447\,(\mathrm{GeV}/c)^2$, whereas the distributions of Q^2 values for the $\langle Q^2 \rangle = 1.126/1.158$ and $1.450\,(\mathrm{GeV}/c)^2$ points were integrated from $\sim$1.0 to $\sim 1.3\,(\mathrm{GeV}/c)^2$ and from $\sim$1.2 to $\sim 1.7\,(\mathrm{GeV}/c)^2$, respectively.

Henceforth, we use $\langle Q^2 \rangle = 1.132\,(\mathrm{GeV}/c)^2$ to denote the sample-size weighted average of the $\langle Q^2 \rangle = 1.126$ and $1.158\,(\mathrm{GeV}/c)^2$ data sets.

3. Acceptance-averaging analysis iterations

We performed two iterations of the above-described analysis procedure with both the ACCEPTANCE and GENGEN simulation programs.

In the first iteration, the simulations were conducted with the PWBA and FSI+MEC+IC+RC calculations that assumed different multiplicative factors of the standard Galster parametrization for the Q^2 dependence of G_{En}. The optimal values for the scale factors S were then used to compute the optimal values for G_{En}/G_{Mn} according to $G_{En}/G_{Mn} = -S_{\mathrm{optimal}} \times \langle\tau\rangle/(1 + 5.6\langle\tau\rangle)$, where $\langle\tau\rangle = \langle Q^2\rangle/4m_n^2$. Values for G_{En} were then extracted from our optimal values for G_{En}/G_{Mn} using the best-fit values for G_{Mn} taken from the parametrization of Kelly [49]. Then we fitted our first-iteration results for G_{En} together with the then-available world data on G_{En} (as of early 2003) to the modified Galster parametrization described previously in Sec. VI1; the best-fit parameters we found at that time were $a = 0.894 \pm 0.023$ and $b = 3.55 \pm 0.37$. This fit included the then-available data on G_{En} extracted from measurements using polarization degrees of freedom [23,34,39,41,43,48] and an analysis of the deuteron quadrupole form factor [10], and also data on the slope of G_{En} as measured via low-energy neutron scattering from electrons in heavy atoms [77]. Since the conclusion of this analysis, new data on G_{En} have been published [50,51], and a new modified Galster parametrization has been published [78].

In our second analysis iteration, a second set of the PWBA and FSI+MEC+IC+RC calculations were performed that assumed this modified Galster parametrization for the Q^2 dependence of G_{En}. The ACCEPTANCE and GENGEN simulations were both repeated using these new calculations, and the procedure for the extraction of the optimal G_{En}/G_{Mn} values was identical to that of the first iteration.

TABLE VII. Analyzing powers for (n, n) and (n, p) events at each of our Q^2 points. The errors are statistical.

Event type	$\langle Q^2 \rangle$ [$(\mathrm{GeV}/c)^2$]		
	0.447	1.132	1.450
(n, n)	0.141 ± 0.004	0.137 ± 0.010	0.144 ± 0.013
(n, p)	0.103 ± 0.005	0.075 ± 0.007	0.071 ± 0.011

The differences between the first and second analysis iterations were negligible. This result is not surprising, because (1) both parametrizations have small second derivatives in the vicinity of our Q^2 points and (2) the acceptance was fairly symmetric about the acceptance-averaged values of Q^2.

4. Acceptance-averaging analysis results

The pairwise analysis method was employed for the extraction of our G_{En}/G_{Mn} values at $\langle Q^2 \rangle = 0.447\ (\mathrm{GeV}/c)^2$ (only two precession angles), whereas the global analysis method was employed for the analysis of our $\langle Q^2 \rangle = 1.132$ and 1.450 $(\mathrm{GeV}/c)^2$ data sets. The final acceptance-averaged and nuclear physics-corrected values for G_{En}/G_{Mn} we obtained with the ACCEPTANCE program and GENGEN agreed to better than 1% at $\langle Q^2 \rangle = 0.447$ and 1.132 $(\mathrm{GeV}/c)^2$ and 2% at $\langle Q^2 \rangle = 1.450\ (\mathrm{GeV}/c)^2$, well within the statistical errors; therefore, the values for G_{En}/G_{Mn} we report later in Table IX are the average of the central values obtained with our two simulation programs. The analyzing powers we extracted from our acceptance-averaging analysis procedures are summarized in Table VII.

C. Systematic uncertainties

An itemized summary of estimates for the magnitudes of our relative systematic uncertainties in G_{En}/G_{Mn} appears in Table VIII. Our final values for the total relative systematic uncertainties, 2–3%, are much smaller than our relative statistical uncertainties. Brief discussions of each itemized systematic uncertainty (and others deemed negligibly small) appear below.

TABLE VIII. Compilation of our estimated relative systematic uncertainties in G_{En}/G_{Mn} [%]. The total systematic error that is quoted for each Q^2 point and precession angle combination is the quadrature sum of the itemized systematic uncertainties.

Source	$\langle Q^2 \rangle$ [$(\mathrm{GeV}/c)^2$]				
	0.447[a]	1.132[a]	1.132[b]	1.450[a]	1.450[b]
Beam polarization	1.6	0.7	0.4	1.2	0.3
Charge-exchange	<0.1	<0.1	0.1	<0.1	0.2
Depolarization	<0.1	0.1	<0.1	<0.1	0.6
Positioning/traceback	0.2	0.3	0.3	0.4	0.4
Precession angle	1.1	0.3	0.1	0.5	0.1
Radiative corrections	0.7	0.1	0.1	0.1	0.1
Timing calibration	2.0	2.0	2.0	2.0	2.0
Total	2.9	2.2	2.1	2.4	2.2

[a] $\chi = \pm 40^\circ$ precession.
[b] $\chi = 0^\circ, \pm 90^\circ$ precession.

1. Beam polarization

The beam polarization cancels in the form factor ratio only if it does not vary during sequential measurements of the scattering asymmetries. Consequently, fluctuations in the beam polarization measurements introduce a systematic uncertainty. We estimated the temporal uncertainty in the beam polarization via the following procedure. First, polarization measurements conducted under similar conditions at the polarized source were grouped into clusters. Second, the mean value of the polarization for each cluster was computed and then recentered about the nominal 80% polarization. Next, the statistical error for the entire data set (i.e., all identified clusters) was computed, and the overall uncertainty was then increased by the square root of χ^2 (to account for the observed fluctuations). Finally, our total estimated uncertainty in the polarization was propagated through the expression for the form factor ratio, Eq. (4).

2. Charge-exchange in the lead curtain

Estimates of the contamination levels from the two-step $^2\mathrm{H}(\vec{e}, e'\vec{p}) + \mathrm{Pb}(\vec{p}, \vec{n})$ charge-exchange reaction were given previously in Sec. VG2. To estimate the systematic uncertainty in G_{En}/G_{Mn} because of contamination from this background process, we computed values for the recoil proton's polarization using values for G_{Ep} and G_{Mp} taken from the parametrization of Ref. [79]. These polarization components were then transported through the Charybdis dipole field using estimates for the proton spin precession angles. As there are very few data on the lead polarization transfer coefficient, D_{SS}^{Pb}, we calculated the correction to the asymmetries (using information on the analyzing powers extracted from our acceptance-averaging analysis and the values for, and the uncertainties in, the charge-exchange contamination levels) for various (reasonable) choices of D_{SS}^{Pb}. Spreads in the resulting values of G_{En}/G_{Mn} were then defined to be the systematic uncertainties.

3. Neutron depolarization in the lead curtain

The total n+Pb cross section is fairly flat at ~3 barns over the range of neutron kinetic energies in our experiment (slow rise with energy) [75]. For our 10.16-cm-thick lead curtain, our GENGEN simulations indicated a 30.8%, 42.5%, 43.0%, and 46.7% interaction probability for the neutron energies at our $\langle Q^2\rangle = 0.447$, 1.126, 1.158, and 1.450 $(\mathrm{GeV}/c)^2$ points, respectively. We found that the contamination levels within our $[-1, 1]$ ns cTOF window from neutrons suffering one or more interactions in the lead curtain were 0.04%, 3.8%, 4.2%, and 9.3% at $\langle Q^2\rangle = 0.447$, 1.126, 1.158, and 1.450 $(\mathrm{GeV}/c)^2$, respectively. The fact that our simulations predicted a much more rapid increase in the contamination levels with energy as compared to the interaction probabilities is because the angular distributions for *nn* and *np* scattering peak at large (small) scattering angles for the neutron kinetic energies at our lowest (highest) Q^2 point (as computed by SAID [70]). Further, our simulations suggested that interactions in the lead curtain may have been partly responsible for the small tail observed on the slow side of our experimental cTOF distributions at our highest Q^2 point (see Fig. 15).

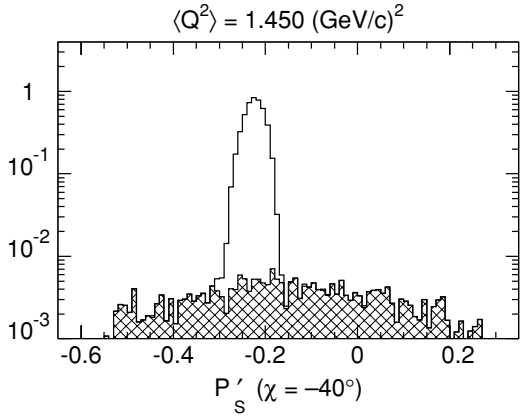

FIG. 24. Sample GENGEN simulated $\langle P_S'\rangle$ spectrum for $\chi = -40^\circ$ precession at $\langle Q^2\rangle = 1.450$ $(\mathrm{GeV}/c)^2$. The unfilled histogram is summed over all simulated events, whereas the cross-hatched histogram is summed over those events suffering one or more interactions in the lead curtain. The units of the ordinate are arbitrary.

The quantity of interest was the spectrum of the polarization presented to the polarimeter front array for neutrons that did and did not interact with the lead curtain. A sample result comparing polarization spectra for these two types of events for $\chi = -40^\circ$ precession at $\langle Q^2\rangle = 1.450\,(\mathrm{GeV}/c)^2$ is shown in Fig. 24. Our simulations indicated that the distribution of polarizations for neutrons suffering an interaction in the lead curtain is a broad continuum, yielding a depolarization of the neutron flux presented to the polarimeter. Similar results were observed at our other Q^2 points. We found, though, that the effects of depolarization in the lead curtain tend to cancel in the polarization ratio, leading to small systematic uncertainties in the G_{En}/G_{Mn} ratio. The magnitudes of the residual noncancellations were taken to be the uncertainties listed in Table VIII.

4. Positioning and traceback

Two contributions to an uncertainty in the electron scattering angle were considered: positioning (offset in the scattering angle from the nominal value) and traceback (reconstruction from the focal plane to the target). For the purposes of this analysis, we assumed the uncertainties in the electron scattering angle, $\Delta\theta_{e'}$, were $\Delta\theta_{e'} = 1.2$ and 1.3 mrad for the positioning and traceback uncertainties, respectively; these values were derived from a systematic analysis of kinematic data taken during this experiment. The systematic uncertainties in G_{En}/G_{Mn} were obtained via propagation of these values for $\Delta\theta_{e'}$ through Eq. (4) for the form factor ratio.

5. Precession angle

Uncertainties in the neutron spin precession angle were estimated [64] via a calculational scheme that employed the reconstructed kinematics from the experimental data as the source of the neutron momentum vectors incident on the Charybdis dipole field. Spin vectors were transported through the field using the same magnetic spin transport algorithms developed for our two simulation programs. This technique

TABLE IX. Summary of our final results for G_{En}/G_{Mn} and G_{En}. The first (second) set of errors is statistical (systematic). The results reported here are the weighted average of (n, n) and (n, p) events in the polarimeter.

Analysis	Quantity	$\langle Q^2 \rangle$ [(GeV/c)^2]		
		0.447	1.132	1.450
$n(\vec{e}, e'\vec{n})$	G_{En}/G_{Mn}	$-0.0681 \pm 0.0084 \pm 0.0020$	$-0.122 \pm 0.011 \pm 0.003$	$-0.174 \pm 0.017 \pm 0.004$
^{2}H$(\vec{e}, e'\vec{n})^1$H PWBA	G_{En}/G_{Mn}	$-0.0713 \pm 0.0086 \pm 0.0021$	$-0.126 \pm 0.010 \pm 0.003$	$-0.183 \pm 0.018 \pm 0.004$
^{2}H$(\vec{e}, e'\vec{n})^1$H FSI+MEC+IC+RC	G_{En}/G_{Mn}	$-0.0755 \pm 0.0089 \pm 0.0022$	$-0.131 \pm 0.011 \pm 0.003$	$-0.189 \pm 0.018 \pm 0.004$
Values from Ref. [78]	$G_{Mn}/\mu_n G_D$	1.003 ± 0.005	1.067 ± 0.012	1.064 ± 0.016
$n(\vec{e}, e'\vec{n})$	G_{En}	$0.0492 \pm 0.0061 \pm 0.0015$	$0.0370 \pm 0.0032 \pm 0.0009$	$0.0383 \pm 0.0038 \pm 0.0011$
^{2}H$(\vec{e}, e'\vec{n})^1$H PWBA	G_{En}	$0.0515 \pm 0.0062 \pm 0.0015$	$0.0381 \pm 0.0032 \pm 0.0009$	$0.0403 \pm 0.0039 \pm 0.0011$
^{2}H$(\vec{e}, e'\vec{n})^1$H FSI+MEC+IC+RC	G_{En}	$0.0545 \pm 0.0064 \pm 0.0016$	$0.0396 \pm 0.0032 \pm 0.0010$	$0.0415 \pm 0.0039 \pm 0.0011$

provided a measure of the sensitivity of the precession angle to details of the field map. The uncertainties in the mean values of the precession angles derived from these studies (at the level of $\pm 0.2^\circ$) were combined in quadrature with two other sources of uncertainty. First, as discussed in Sec. IV C, we observed small differences between the measured field integrals for opposite magnet polarities and also between the field integrals derived from our measured maps and the calculated TOSCA maps. These uncertainties were estimated to be on the level of $\pm 0.3^\circ$. Second, as also discussed in Sec. IV C, the field was mapped only along the central axis; therefore, we assigned further uncertainties (at the level of $\pm 0.2^\circ$) for incomplete knowledge of the field beyond the central axis. Our best estimates of the total uncertainties in the precession angle were then propagated through the form factor ratio, Eq. (4).

6. Radiative corrections

Radiative corrections were calculated specifically for the kinematics of this experiment by Afanasev *et al*. [80]. The primary effect of radiative corrections on the recoil polarization components $P_t^{(h)}$ and $P_\ell^{(h)}$ was found to be depolarization of the electron such that both components of the recoil polarization should be increased by $\sim$1.9% $\sim$3.7%, and $\sim$4.4% at $\langle Q^2 \rangle =$ 0.447, 1.132, and 1.450 (GeV/c)^2, respectively; however, these corrections nearly cancel in the form factor ratio such that the net effect is small at $\langle Q^2 \rangle = 0.447$ (GeV/c)^2 and negligible at the two higher Q^2 points. The residual noncancellations of the corrections in the form factor ratio were taken to be the systematic uncertainties we quote in Table VIII.

7. Timing calibration of the polarimeter

The timing calibrations we deemed suitable for certain running conditions (e.g., periods in between changes to the high-voltages for the PMTs) were obtained using a subset of the data for that particular running period. To assess the dependence of our results for the scattering asymmetries on the choice of the subset of data employed for the timing calibration, various calibrations were generated from different subsets of the available data. Excellent agreement was always found between the results for the scattering asymmetries obtained from analyses using these different calibrations; however, we did find a $\sim$2% sensitivity of our results to the choice of the subset of data employed for the timing calibration.

8. Other uncertainties

We deemed two other possible sources of systematic uncertainties to be negligible. First, we demonstrated quantitatively that our scattering asymmetries were insensitive (within statistical errors) to a possible geometric asymmetry in the polarimeter (i.e., a spin-averaged "top-bottom" asymmetry) by varying our software energy thresholds on the top (bottom) rear array while maintaining a constant threshold on the bottom (top) rear array. Second, analysis of our data taken with the "dummy targets" (see Sec. IIIE) showed that the level of contamination within our $[-1, 1]$ ns cTOF window from scattering in the target cell windows was negligible ($<$0.05%).

D. Summary of final G_{En}/G_{Mn} and G_{En} results

Our final results for G_{En}/G_{Mn} and G_{En} extracted from three different analyses are tabulated in Table IX and compared in Fig. 25. The three analyses are for: (1) elastic $n(\vec{e}, e'\vec{n})$ scattering and infinitesimal HMS and NPOL point

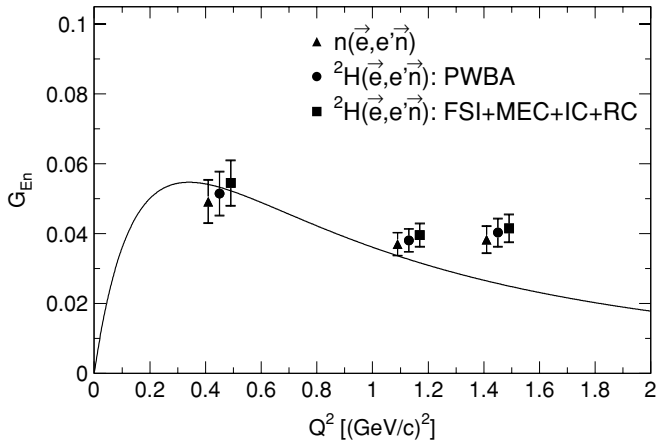

FIG. 25. Comparison of our results for G_{En} at $\langle Q^2 \rangle = 0.447$, 1.132, and 1.450 (GeV/$c$)^2 extracted from the various analyses summarized in Table IX. The data points shown for the three analyses at each $\langle Q^2 \rangle$ point have been slightly displaced about the actual $\langle Q^2 \rangle$ value for clarity. The solid curve is the Galster parametrization [37].

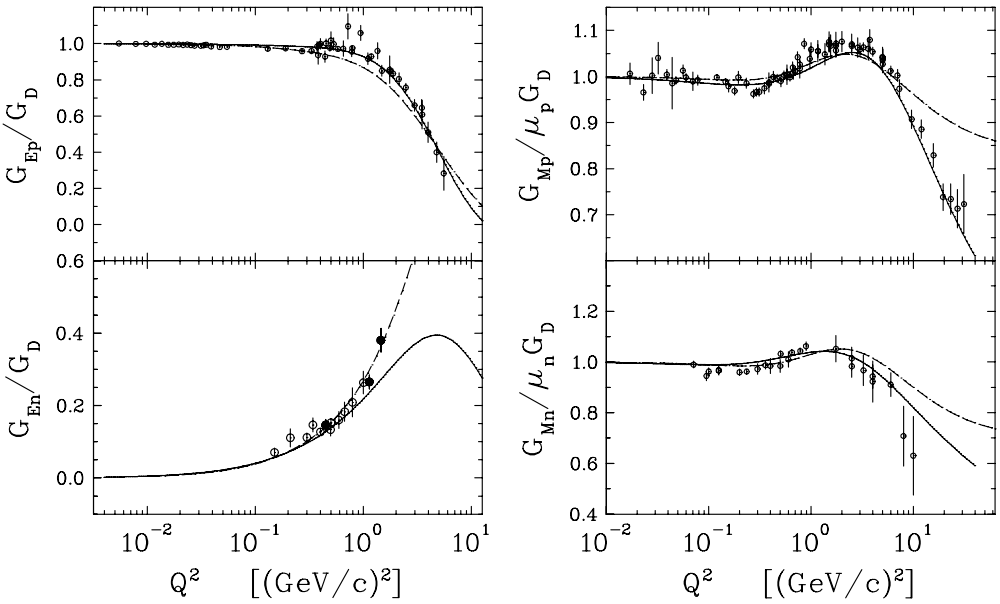

FIG. 26. Comparison of representative VMD models with nucleon form factor data (G_{Ep} from Refs. [81,82]; G_{Ep}/G_{Mp} from Refs. [83–86]; G_{Mp} from Refs. [47,79]; G_{En} from Refs. [23,39,41,43,48,50,51]; G_{Mn} from Refs. [8,44,46,87,88]). (Dashed curve) Bijker and Iachello [92]; (solid curve) version GKex(02S) of Lomon [94].

acceptances; (2) quasielastic $^2\mathrm{H}(\vec{e}, e'\vec{n})^1\mathrm{H}$ scattering and acceptance-averaging of the PWBA model; and (3) quasielastic $^2\mathrm{H}(\vec{e}, e'\vec{n})^1\mathrm{H}$ scattering and acceptance-averaging of the FSI+MEC+IC+RC model.

We note that in our first publication [12] we used values for G_{Mn} taken from Ref. [49]; here we use slightly different values for G_{Mn} taken from Ref. [78]. The total systematic errors we quote for G_{En} are the quadrature sum of the experimental sytematic errors and the relative uncertainties in G_{Mn}.

E. Comparison of nucleon form factor data with selected theoretical model calculations

The availability of precise new data on nucleon form factors has stimulated much more theoretical work in the last few years than we can review here; our selection of models is not intended to be complete. Although the present experiment is limited to G_{En}, we believe that comparison with models must consider all four Sachs form factors. In this section, we compare representative models with selected data. The data from this experiment are shown as filled circles in Figs. 26–29, whereas data from other experiments are shown as open circles. We selected [81,82] for G_{Ep}, [83–86] for G_{Ep}/G_{Mp}, [47,79] for G_{Mp}, [23,39,41,43,48,50,51] for G_{En}, and [8,44, 46,87,88] for G_{Mn}.

1. Models based on vector meson dominance

Models based on vector meson dominance (VMD) postulate that the virtual photon couples either directly to an intrinsic nucleon core or through the mediation of a neutral vector meson, initially limited to the lowest ω, ρ, and ϕ mesons. The earliest versions assumed that the core is a structureless Dirac particle. Iachello *et al.* [89] assigned the core a form factor and employed a model of the ρ width. Gari and Krümpelmann [90,91] then permitted different Dirac and Pauli intrinsic form factors and introduced modifications that ensured consistency with pQCD scaling at large Q^2 and logarithmic running of the strong coupling constant. Bijker and Iachello [92] adopted the Gari and Krümpelmann (GK) pQCD prescriptions and refit their model to modern data, still using a common intrinsic form factor. This fit, using a total of six free parameters, is compared with the data in Fig. 26. Finally, Lomon [93,94] produced a more flexible set of fits using a model described as "GK extended"; the GKex(02S) version is also shown in Fig. 26. The Lomon model uses two intrinsic form factors, the GK prescription for the pQCD limit, and includes $\rho'(1450)$ and $\omega'(1419)$ couplings in addition to the customary ρ, ω, and ϕ couplings. The ρ width is included but the ρ' and ω' structures are not. The fit achieved by this extended model, with 13 free parameters, is clearly superior, especially at large Q^2. The Bijker and Iachello model describes the qualitative behavior of G_{Ep}, but its transition between $G_{Ep}/G_D \approx 1$ at low Q^2 and the nearly linear decrease for $1 < Q^2 < 6$ (GeV/c)^2 is too gradual. Nor does it reproduce the slope in $G_{Mp}/\mu_p G_D$ for $Q^2 > 10$ (GeV/c)^2. Both of these features are fit well by the Lomon model. Unfortunately, the neutron data do not discriminate between these models very strongly. The Bijker and Iachello model provides a slightly better fit to the present G_{En} data, but the Lomon fit was performed before these data became available; it is likely that only a slight parameter adjustment would be needed to achieve a comparable fit without sacrificing the fits to the other form factors. It will be interesting to see whether the rather large values for G_{En}/G_D for $Q^2 > 2$ (GeV/c)^2 predicted by the Bijker and Iachello model are confirmed by upcoming experiments [95,96] that will probe G_{En} to $Q^2 = 4.3$ (GeV/c)^2. Note, however, that the Bijker and Iachello fit is systematically above the G_{Mn} data for the same kinematics, $Q^2 > 2$ (GeV/c)^2.

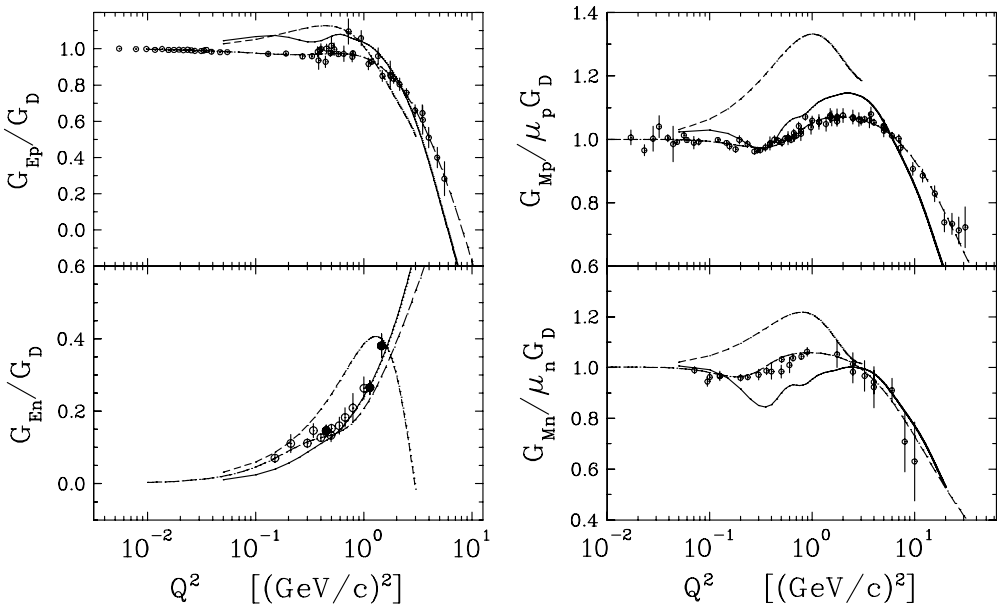

FIG. 27. Comparison of representative pion cloud models with nucleon form factor data (G_{Ep} from Refs. [81,82]; G_{Ep}/G_{Mp} from Refs. [83–86]; G_{Mp} from Refs. [47,79]; G_{En} from Refs. [23,39,41,43,48,50,51]; G_{Mn} from Refs. [8,44,46,87,88]). (Short-dashed curve) QMC model [97]; (solid curve) LFCBM [103]; (long-dashed curve) Friedrich and Walcher parametrization [52].

2. Models emphasizing the pion cloud

The role of the pion in mediation of the long-range nucleon-nucleon interaction clearly demonstrates its importance in understanding form factors for low Q^2. Typical pion cloud models describe nucleon form factors using diagrams in which the virtual photon couples to either a bare nucleon core or to the nucleon or the pion loop in a single-pion loop. Some models also permit excitation of the intermediate state and include additional contact terms. A relatively simple example is the Adelaide version [97] of the cloudy bag model (CBM) in which the core is based on the bag model, intermediate excitation is neglected, and relativistic corrections are made using a simple ansatz for Lorentz contraction [98]. Predictions from Lu *et al*. [97] using a bag radius of 0.8 fm are compared with the data in Fig. 27. Although density-dependent extensions of this model, described as the quark-meson coupling (QMC) model, have been used to study the sensitivity of recoil polarization in nucleon electromagnetic knockout to medium modifications of the nucleon form factors [99–102], its description of free form factors is rather poor and one must hope that the density dependence of G_E/G_M ratios is more accurate.

Alternatively, the light front cloudy bag model (LFCBM) of Miller [103] maintains Poincaré invariance by formulating wave functions using the light-front approach. This version should then be applicable to higher Q^2. There are only four adjustable parameters and the results for Set 1 are compared with data in Fig. 27. A previous version of this model [104] provided one of the earliest predictions of the sharp slope in G_{Ep}/G_{Mp} for $Q^2 > 1$ (GeV/c)^2, but the agreement with recent recoil-polarization data is only qualitative. The LFCBM calculation for G_{Mp}/G_D also decreases too rapidly at large Q^2. Calculations using this model agree relatively well with the G_{En} data for $Q^2 \gtrsim 1$ (GeV/c)^2 but are too small at lower Q^2. Interestingly, this model predicts much stronger values for G_{En}/G_D at large Q^2 than the Lomon parametrization. However, the LFCBM calculations for three of the four form factors show complicated and rather implausible shapes for $Q^2 < 1$ (GeV/c)^2 that disagree strongly with data.

Chiral effective field theory [105,106] provides a more systematic procedure that includes intermediate excitation and can be extended to two pion loops [107]. Alternatively, two-loop contributions can be evaluated in dispersion theory [108]. Recently it has become possible also to include both pion loops and vector meson diagrams in a consistent manner [109]; however, we do not show curves here because this approach remains limited to $Q^2 \lesssim 0.4$ (GeV/c)^2.

Friedrich and Walcher [52] performed a phenomenological analysis of the nucleon electromagnetic form factors using a parametrization motivated by pion cloud models. The core form factor is represented by two dipole form factors with different ranges, whereas the pion cloud contribution, represented as a "bump" at low Q^2, is described by two Gaussians. These fits, with five free parameters for G_{En} and six for each of the other form factors, are also compared with data in Fig. 27. The quality of these fits is generally satisfactory, but it is not clear that the postulated oscillation in G_{En}/G_D is warranted by the available data; considerably better experimental precision at $Q^2 \sim 0.3$ (GeV/c)^2 would be needed to justify such a structure.

A closer look at the G_{En} data is given in Fig. 28. The original Friedrich and Walcher fit (short-dashed curve) used a very preliminary version of the data from the present experiment and falls systematically below the final data for this and other more recent experiments for $Q^2 > 0.5$ (GeV/c)^2. A reanalysis using final data for this experiment plus new data [43,50,51] was made by Glazier *et al*. [51] and is shown as the long-dashed curve featuring a bump for $Q^2 \sim 0.3$ (GeV/c)^2 superimposed upon a much flatter core form factor. With five parameters

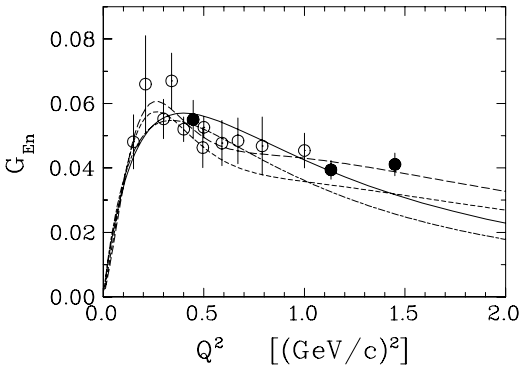

FIG. 28. Closer look at comparison of representative pion cloud models with data on G_{En} (data from Refs. [23,39,41,43,48,50,51]). (Solid curve) A fit based on the pion cloud model of Kaskulov and Grabmayr [110]. (Short-dashed curve) Parametrization of Friedrich and Walcher [52]. (Long-dashed curve) Reanalysis by Glazier *et al*. [51] using the Friedrich and Walcher model. The dash-dotted curve is the original Galster parametrization [37].

it is obviously possible to fit the data very well, perhaps too well—the simple two-parameter fit of Kelly [78] based on the Galster parametrization already provides $\chi^2_\nu = 0.8$ without distinguishing between soft and hard structures. The data presently available do not require this complication. Data at higher Q^2 should test whether such a hard core is needed but significantly more precise data for low Q^2 would be needed to establish the soft pion cloud contribution to G_{En}.

Finally, Kaskulov and Grabmayr [110] used a chiral quark model (χQM) to derive a relationship

$$G_{En} = \bar{S}(1 - F_\pi)G_C, \tag{26}$$

between G_{En}, the pion form factor F_π, and the core form factor G_C for the three-quark component of the nucleon. The coefficient $\bar{S}$ is a weighted average over spectroscopic factors for N and Δ intermediate states in the one-pion loop contribution to the self-energy but is treated as an adjustable parameter. If one stipulates a monopole for $F_\pi = (1 + Q^2/\Lambda_\pi^2)^{-1}$ and a dipole for $G_C = (1 + Q^2/\Lambda_C^2)^{-2}$, the neutron electric form factor

$$G_{En} = \bar{S}\frac{b\tau}{1 + b\tau}G_C, \tag{27}$$

with $b = 4m_N^2/\Lambda_\pi^2$ reduces to a Galster-like form with up to three free parameters ($\bar{S}$, Λ_π, Λ_C); however, $\bar{S}$ is largely determined by the neutron radius

$$\langle r^2\rangle_n = -6\left(\frac{\partial G_{En}}{\partial Q^2}\right)_{Q^2\to 0} = -\frac{3\bar{S}b}{2m_N^2}. \tag{28}$$

If we further assume that Λ_π within a loop is the same as that for pion electroproduction, only Λ_C remains to be fit to data for G_{En}. Thus, using fixed parameters $\bar{S} = 0.26$ and $b = 6.65$ suggested by Kaskulov and Grabmayr, we fit $\Lambda_C^2 = 1.00 \pm 0.03$ (GeV/c)^2 to the current G_{En} data. The value given in Ref. [110] for Λ_C is slightly smaller because they used the same preliminary data as [52] that are smaller than the final results. Our fit is shown in Fig. 28 and is practically indistinguishable from the two-parameter Galster fit given in Ref. [78]. The Kaskulov and Grabmayr model has the same physical basis as that of Friedrich and Walcher, but is much more constrained; nevertheless, it fits the G_{En} data quite well. This result suggests that the radius of the $3q$ nucleon core is

$$\langle r^2\rangle_{3q}^{1/2} = \frac{\sqrt{12}}{\Lambda_C} = (0.68 \pm 0.01)\ \text{fm}. \tag{29}$$

3. *Quark models*

The predictions of several recent relativistic constituent quark models are compared with the data in Fig. 29. All

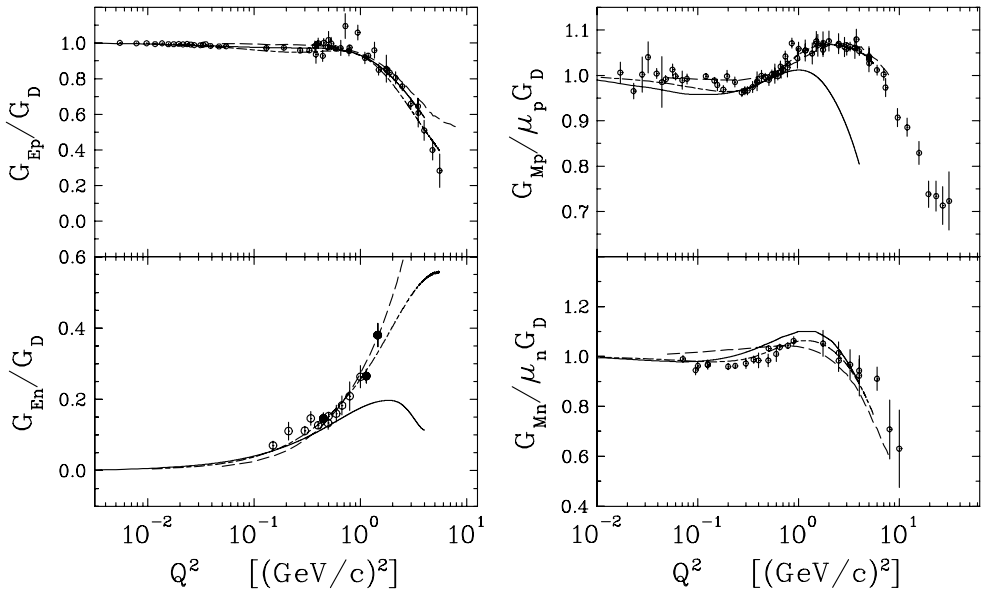

FIG. 29. Comparison of representative quark models with nucleon form factor data (G_{Ep} from Refs. [81,82]; G_{Ep}/G_{Mp} from Refs. [83–86]; G_{Mp} from Refs. [47,79]; G_{En} from Refs. [23,39,41,43,48,50,51]; G_{Mn} from Refs. [8,44,46,87,88]). (Solid curve) PFSA using pointlike constituents [111]. (Long-dashed curve) Light-front using OGE interaction and constituent-quark form factors [112,113]. (Dash-dotted curve) hCQM with constituent-quark form factors [114].

employ a linear confining potential. The solid curves show calculations of the Pavia-Graz collaboration [111] that used the point-form spectator approximation (PFSA) for pointlike constituent quarks and a Goldstone boson exchange interaction fitted to spectroscopic data. No additional parameters were adjusted to fit the form factors. The data for G_{Ep}/G_D are reproduced very well and the data for magnetic form factors are also described relatively well for $Q^2 \lesssim 1$ (GeV/c)^2, but the calculated value of $G_{Mp}/\mu_p G_D$ decreases too rapidly for larger Q^2. The prediction for G_{En}/G_D lies well below the data for $Q^2 > 1$ (GeV/c)^2. The long-dashed curves show calculations of Simula [112], based on the model of Cardarelli *et al*. [113], that used the light-front approach and the one-gluon exchange (OGE) interaction. Here, constituent-quark form factors were fitted to data for $Q^2 < 1$ (GeV/c)^2 and the calculations were extrapolated to larger Q^2. This approach provides good fits up to about 4 (GeV/c)^2. Finally, the dash-dotted curves show the results for a semirelativistic hypercentral constituent quark model (hCQM) [114] where the constituent-quark form factors, chosen as linear combinations of monopole and dipole forms, were also fitted to recent data. Of the selected quark model calculations, their results clearly achieve the best overall agreement with the data.

Finally, the most recent lattice QCD calculations of nucleon form factors were reported by the QCDSF collaboration [115] using nonperturbatively improved Wilson fermions in the quenched approximation. Unfortunately, straightforward chiral extrapolation [116] does not provide adequate agreement with data for $Q^2 < 1.5$ (GeV/c)^2. Matevosyan *et al*. [117] proposed a model-dependent extrapolation procedure based on the LFCBM. This extrapolation is quite severe because the lattice calculations remain limited to quark masses that correspond to $m_\pi \geqslant 0.5$ GeV, lattice spacings with $a \geqslant 0.05$ fm, and volumes that might not fully contain the pion cloud; therefore, comparison with data is probably premature.

VII. SUMMARY AND CONCLUSIONS

We reported values for the neutron electric to magnetic form factor ratio, G_{En}/G_{Mn}, deduced from measurements of the neutron's recoil polarization in quasielastic $^2\mathrm{H}(\vec{e}, e'\vec{n})^1\mathrm{H}$ kinematics at three acceptance-averaged Q^2 values of 0.45, 1.13, and 1.45 (GeV/c)^2. In the one-photon exchange approximation for elastic scattering from a free neutron, the polarization vector of the recoil neutron is confined to the scattering plane and consists of a longitudinal component, $P_\ell^{(h)} \propto G_{Mn}^2$, and a transverse component, $P_t^{(h)} \propto G_{En} G_{Mn}$. The use of a deuteron target to access the neutron form factor ratio via the quasielastic $^2\mathrm{H}(\vec{e}, e'\vec{n})^1\mathrm{H}$ reaction has the advantage, as established by Arenhövel *et al*. [19,20], that both $P_t^{(h)}$ and $P_\ell^{(h)}$ are relatively insensitive to final-state interactions (FSI), meson-exchange currents (MEC), isobar configurations (IC), and theoretical models of deuteron structure.

A high-luminosity neutron polarimeter designed specifically for our experiment, Jefferson Laboratory E93-038, was used to measure neutron polarization-dependent scattering asymmetries proportional to the projection of the polarization vector on the transverse axis. A dipole magnet located upstream of the polarimeter was used to precess the neutron polarization vector in the transverse-longitudinal plane, thereby permitting access to the ratio $P_t^{(h)}/P_\ell^{(h)} \propto G_{En}/G_{Mn}$. Values for the scattering asymmetries were extracted from neutron time-of-flight measurements in our polarimeter via the cross ratio technique. The merit of the cross ratio technique is that the scattering asymmetries are independent of the luminosities for the two electron beam helicity states and independent of the efficiencies and acceptances of the top and bottom halves of the polarimeter. Systematic uncertainties in our results are minimal as the analyzing power of the polarimeter and the polarization of the electron beam cancel in the form factor ratio. Further, other sources of uncertainty, such as radiative corrections and neutron depolarization by lead shielding, are small as they nearly cancel in the ratio.

To account for the finite experimental acceptance and nuclear physics effects (i.e., FSI, MEC, and IC), we used two independent simulation programs to average theoretical $^2\mathrm{H}(\vec{e}, e'\vec{n})^1\mathrm{H}$ recoil polarization calculations computed according to the model of Arenhövel *et al*. [19,20] over the acceptance. The results from these two simulation programs agreed to better than 1% at our two lower Q^2 points and 2% at our highest Q^2 point. Further, by averaging two different sets of theoretical calculations assuming different parametrizations for G_{En}, our acceptance-averaged and nuclear physics-corrected values for G_{En} were found to be insensitive to the choice of the Q^2 dependence of G_{En}.

Our results for G_{En} and data on the nucleon form factors were compared with selected theoretical model calculations. All of the model calculations based on vector meson dominance and those emphasizing the pion cloud presented here provide qualitative agreement with some of the four nucleon form factors, but no model achieves simultaneous agreement with all four form factors. The predictions of several recent relativistic quark models also achieve qualitative agreement with the data, with the most successful models utilizing form factors for the constituents; the results from a chosen model assuming pointlike constituents are not as successful. Although a comparison between data and the results of lattice QCD calculations is probably premature, the recent precise data obtained from experiments employing polarization degrees of freedom will no doubt serve as a future challenging test of QCD as formulated on the lattice.

In conclusion, our results at $Q^2 = 1.13$ and 1.45 (GeV/c)^2 are the first direct measurements of G_{En} using polarization degrees of freedom in the $Q^2 > 1$ (GeV/c)^2 region and are the most precise determinations of G_{En} over all ranges of Q^2. The achievement of relative statistical uncertainties in the form factor ratio G_{En}/G_{Mn} of 8.4% and 9.5%, respectively, at these two Q^2 points, together with relative systematic uncertainties on the level of 2%, was a triumph for our high figure-of-merit and high luminosity neutron polarimeter.

ACKNOWLEDGMENTS

This work was supported in part by grants from the U.S. National Science Foundation, the U.S. Department of Energy, and the Deutsche Forschungsgemeinschaft. Two of

us (R.M. and T.E.) acknowledge support during the planning phase of E93-038 from the Nuclear and High Energy Physics Center at Hampton University. The Southeastern Universities Research Association operates the Thomas Jefferson National Accelerator Facility under the U.S. Department of Energy contract no. DE-AC05-84ER40150. We thank the Jefferson Laboratory accelerator division staff for delivering the high-quality polarized electron beam to our experiment. Finally, we thank the Jefferson Laboratory Hall C engineering and technical staff for their skillful assistance during our experiment.

APPENDIX A: FORMALISM FOR THE QUASIELASTIC ^{2}H($\vec{e}$, $e'\vec{n}$)^{1}H REACTION

Our notation for the kinematics and nucleon recoil polarization for the quasielastic $^2\mathrm{H}(\vec{e}, e'\vec{n})^1\mathrm{H}$ reaction follows that of Arenhövel *et al.* (e.g., [118]). For ease of notation, all kinematic quantities in the center-of-mass (c.m.) frame of the recoiling neutron-proton (n-p) system will carry a superscript c.m.; however, kinematic quantities referred to the laboratory frame will not be adorned with a superscript lab.

1. Kinematic notation

A schematic diagram of the kinematics for the electrodisintegration of the deuteron in the one-photon exchange approximation is shown in Fig. 30. Our notation for the electron kinematics is as usual, and we assume the electron scatters from a deuteron with initial four-momentum $(m_d, \mathbf{0})$. Following the breakup of the deuteron, the proton and neutron exit with three-momenta $\mathbf{p}_p$ and $\mathbf{p}_n$, respectively. As is customary, we use θ_{pq} (θ_{nq}) to denote the polar angle between $\mathbf{p}_p$ ($\mathbf{p}_n$) and $\mathbf{q}$ in the laboratory frame, and a reaction plane is defined by any two of $\mathbf{q}$, $\mathbf{p}_p$, and $\mathbf{p}_n$. As is shown in Fig. 30, the reaction plane is tilted at a dihedral angle ϕ with respect to the scattering plane. It should be noted that in the n-p c.m. frame, this dihedral angle, $\phi_{np}^{\mathrm{c.m.}}$, is, obviously, just equal to ϕ.

The n-p c.m. frame is reached via a boost along $\mathbf{q}$. In the laboratory frame, the n-p final state has an invariant mass, W_{np}, of $W_{np} = \sqrt{E_{np}^2 - \mathbf{q}^2}$, where the relative n-p energy in the laboratory frame, E_{np}, is $E_{np} = \omega + m_d$. With these definitions, it is clear that the Lorentz factor for the boost from the laboratory frame to the n-p c.m. frame is

$$\gamma = \frac{E_{np}}{W_{np}} = \frac{\omega + m_d}{\sqrt{(\omega + m_d)^2 - \mathbf{q}^2}}. \tag{A1}$$

We denote the polar angle between the relative n-p motion in the c.m. frame, $\mathbf{p}_{np}^{\mathrm{c.m.}} = \frac{1}{2}(\mathbf{p}_p^{\mathrm{c.m.}} - \mathbf{p}_n^{\mathrm{c.m.}}) = \mathbf{p}_p^{\mathrm{c.m.}}$ (assuming equal nucleon masses), and $\mathbf{q}^{\mathrm{c.m.}}$ as $\Theta_{np}^{\mathrm{c.m.}}$. As can be shown easily, this angle can be written solely in terms of the laboratory frame observables $E_n = \sqrt{\mathbf{p}_n^2 + m_n^2}$, $|\mathbf{p}_n|$, θ_{nq}, and ω as

$$\cos\Theta_{np}^{\mathrm{c.m.}} = -\frac{|\mathbf{p}_n|\cos\theta_{nq} - |\mathbf{q}|E_n/E_{np}}{\sqrt{A + B}}, \tag{A2}$$

where

$$A = \mathbf{p}_n^2 \sin^2\theta_{nq}\left(1 - \frac{\mathbf{q}^2}{E_{np}^2}\right), \tag{A3a}$$

$$B = \left(|\mathbf{p}_n|\cos\theta_{nq} - \frac{|\mathbf{q}|E_n}{E_{np}}\right)^2. \tag{A3b}$$

Clearly, $\Theta_{np}^{\mathrm{c.m.}} = 0^\circ$ (180°) corresponds to perfect quasifree emission of the proton (neutron); however, it should be noted that there is vanishing phase space for perfect quasifree emission.

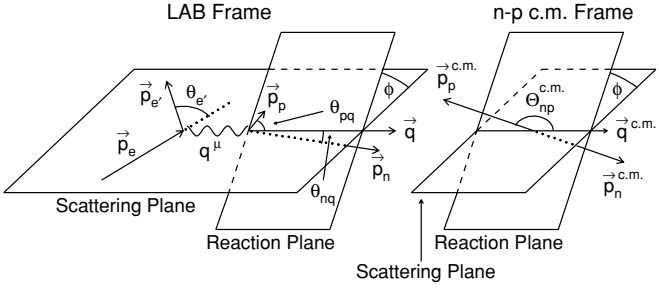

FIG. 30. Schematic diagram of the kinematics for the electrodisintegration of the deuteron in the one-photon exchange approximation as viewed from the laboratory frame and the recoiling n-p c.m. frame.

2. Recoil polarization

The fivefold differential coincidence cross section for the electrodisintegration of the deuteron in polarized-electron, unpolarized-deuteron scattering is of the simple form [20]

$$\sigma(h,0,0) \equiv \frac{d^5\sigma}{dE_{e'}d\Omega_{e'}d\Omega_{np}^{\mathrm{c.m.}}} = \sigma_0(1 + hP_eA_e), \tag{A4}$$

as the electron asymmetry, A_e, is the only polarized contribution to the cross section. As usual, σ_0 denotes the unpolarized cross section. The above expression for the cross section can also be written in terms of structure functions as [20]

$$\begin{aligned}\sigma(h,0,0) = C\big(&\rho_L f_L + \rho_T f_T + \rho_{LT} f_{LT}\cos\phi_{np}^{\mathrm{c.m.}} \\ &+ \rho_{TT} f_{TT}\cos 2\phi_{np}^{\mathrm{c.m.}} + hP_e\rho'_{LT} f'_{LT}\sin\phi_{np}^{\mathrm{c.m.}}\big),\end{aligned} \tag{A5}$$

where the f_i structure functions are evaluated in the n-p c.m. frame, the ρ_i are elements of the virtual photon density matrix and functions of kinematics, and C is a function of kinematics. It should be noted that the above expression for the cross section is differential in $E_{e'}$, $\Omega_{e'}$, and $\Omega_{np}^{\mathrm{c.m.}}$. The Jacobian, $\mathcal{J} = \partial\Omega_{np}^{\mathrm{c.m.}}/\partial\Omega_n$, which transforms $\Omega_{np}^{\mathrm{c.m.}} \to \Omega_n$ is given by [118]

$$\mathcal{J} = \frac{1}{\gamma}\left(\frac{\beta_n\gamma_n}{\beta_n^{\mathrm{c.m.}}\gamma_n^{\mathrm{c.m.}}}\right)^3\left[1 + \frac{\beta}{\beta_n^{\mathrm{c.m.}}}\cos\left(\pi - \Theta_{np}^{\mathrm{c.m.}}\right)\right]^{-1}. \tag{A6}$$

Here, γ is as given in Eq. (A1), $\gamma_n^{\mathrm{c.m.}}$ is the Lorentz factor for the boost that takes the neutron from its rest frame to the n-p CM frame,

$$\gamma_n^{\mathrm{c.m.}} = \frac{W_{np}}{2m_n}, \tag{A7}$$

and γ_n is the Lorentz factor for the boost that takes the neutron from its rest frame to the laboratory frame,

$$\gamma_n = \gamma\gamma_n^{\text{c.m.}}\left[1 + \beta\beta_n^{\text{c.m.}}\cos\left(\pi - \Theta_{np}^{\text{c.m.}}\right)\right], \tag{A8}$$

where β, $\beta_n^{\text{c.m.}}$, and β_n are the velocities (in units of c) associated with γ, $\gamma_n^{\text{c.m.}}$, and γ_n, respectively.

The nucleon recoil polarization in the n-p c.m. frame, $\mathbf{P}^{\text{c.m.}}$, is of the form [20]

$$\frac{d^5\sigma}{dE_{e'}d\Omega_{e'}d\Omega_{np}^{\text{c.m.}}}(\mathbf{P}^{\text{c.m.}}) = \sigma_0[(\mathbf{P}^{(0)})^{\text{c.m.}} + hP_e(\mathbf{P}^{(h)})^{\text{c.m.}}], \tag{A9}$$

where $\mathbf{P}^{(0)}$ and $\mathbf{P}^{(h)}$ denote, respectively, the helicity-independent and helicity-dependent recoil polarization. Written in terms of $g_i^{t,n,\ell}$ structure functions, the helicity-independent polarization components are as follows:

$$\left(P_t^{(0)}\right)^{\text{c.m.}} = \frac{C}{\sigma_0}\left(\rho_{LT}g_{LT}^t\sin\phi_{np}^{\text{c.m.}} + \rho_{TT}g_{TT}^t\sin\phi_{np}^{\text{c.m.}}\right), \tag{A10a}$$

$$\left(P_n^{(0)}\right)^{\text{c.m.}} = \frac{C}{\sigma_0}\left(\rho_L g_L^n + \rho_T g_T^n + \rho_{LT}g_{LT}^n\cos\phi_{np}^{\text{c.m.}} + \rho_{TT}g_{TT}^n\cos 2\phi_{np}^{\text{c.m.}}\right), \tag{A10b}$$

$$\left(P_\ell^{(0)}\right)^{\text{c.m.}} = \frac{C}{\sigma_0}\left(\rho_{LT}g_{LT}^\ell\sin\phi_{np}^{\text{c.m.}} + \rho_{TT}g_{TT}^\ell\sin 2\phi_{np}^{\text{c.m.}}\right), \tag{A10c}$$

and the helicity-dependent polarization components are as follows:

$$\left(P_t^{(h)}\right)^{\text{c.m.}} = \frac{C}{\sigma_0}\left(\rho'_{LT}g_{LT}^{\prime t}\cos\phi_{np}^{\text{c.m.}} + \rho'_T g_T^{\prime t}\right), \tag{A11a}$$

$$\left(P_n^{(h)}\right)^{\text{c.m.}} = \frac{C}{\sigma_0}\rho'_{LT}g_{LT}^{\prime n}\sin\phi_{np}^{\text{c.m.}}, \tag{A11b}$$

$$\left(P_\ell^{(h)}\right)^{\text{c.m.}} = \frac{C}{\sigma_0}\left(\rho'_{LT}g_{LT}^{\prime\ell}\cos\phi_{np}^{\text{c.m.}} + \rho'_T g_T^{\prime\ell}\right). \tag{A11c}$$

The boost from the laboratory frame to the n-p c.m. frame is along $\mathbf{q}$, which is not, in general, parallel to either nucleon's momentum vector; therefore, the recoil polarization components in the laboratory frame are related to the recoil polarization components in the n-p c.m. frame via a relativistic Wigner spin rotation. As the nucleons' momenta span the $\hat{t}$-$\hat{\ell}$ plane, the $\hat{n}$ component is unchanged, whereas the $\hat{t}$- and $\hat{\ell}$-components mix according to the following:

$$P_i = \mathcal{R}_{ij}\left(\theta_n^W\right)P_j^{\text{c.m.}}, \tag{A12}$$

where $i, j \in \{t, n, \ell\}$, $\mathcal{R}_{ij}(\theta_n^W)$ denotes a matrix element of the Wigner rotation matrix,

$$\mathcal{R}\left(\theta_n^W\right) = \begin{pmatrix} \cos\theta_n^W & 0 & \sin\theta_n^W \\ 0 & 1 & 0 \\ -\sin\theta_n^W & 0 & \cos\theta_n^W \end{pmatrix}, \tag{A13}$$

and θ_n^W, the Wigner rotation angle for the neutron, is expressed in terms of kinematics as [118,119]

$$\theta_n^W = \sin^{-1}\left[\frac{1+\gamma}{\gamma_n^{\text{c.m.}} + \gamma_n}\sin\left(\theta_n^{\text{c.m.}} - \theta_n\right)\right]. \tag{A14}$$

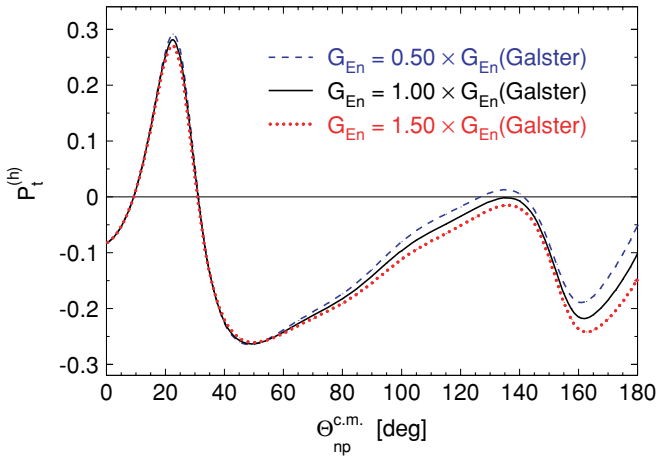

FIG. 31. (Color online) Sensitivity of FSI+MEC+IC+RC calculations of $P_t^{(h)}$ to the value of G_{En} for the central kinematics of our $Q^2 = 1.136\,(\text{GeV}/c)^2$ point. The results shown are for $\phi_{np}^{\text{c.m.}} = 0^\circ$ and the Bonn potential.

Here, $\theta_n^{\text{c.m.}}(= \pi - \Theta_{np}^{\text{c.m.}})$ and θ_n denote, respectively, the polar angle of the neutron's momentum vector relative to $\mathbf{q}$ in the n-p c.m. frame and the laboratory frame. For nonrelativistic

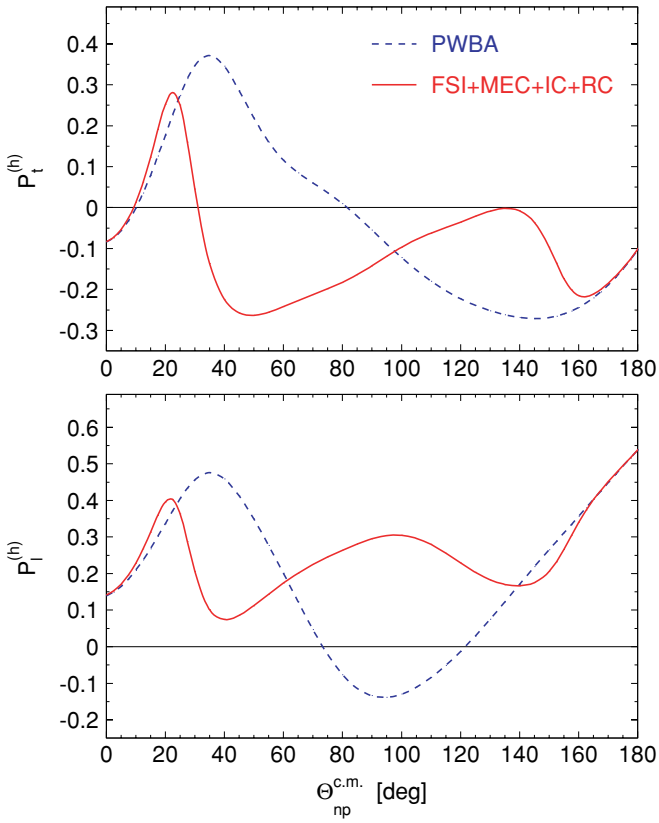

FIG. 32. (Color online) Comparison of PWBA and FSI+MEC+IC+RC calculations of $P_t^{(h)}$ (top panel) and $P_\ell^{(h)}$ (bottom panel) for the central kinematics of our $Q^2 = 1.136\,(\text{GeV}/c)^2$ point. The results shown are for $\phi_{np}^{\text{c.m.}} = 0^\circ$ and the Bonn potential.

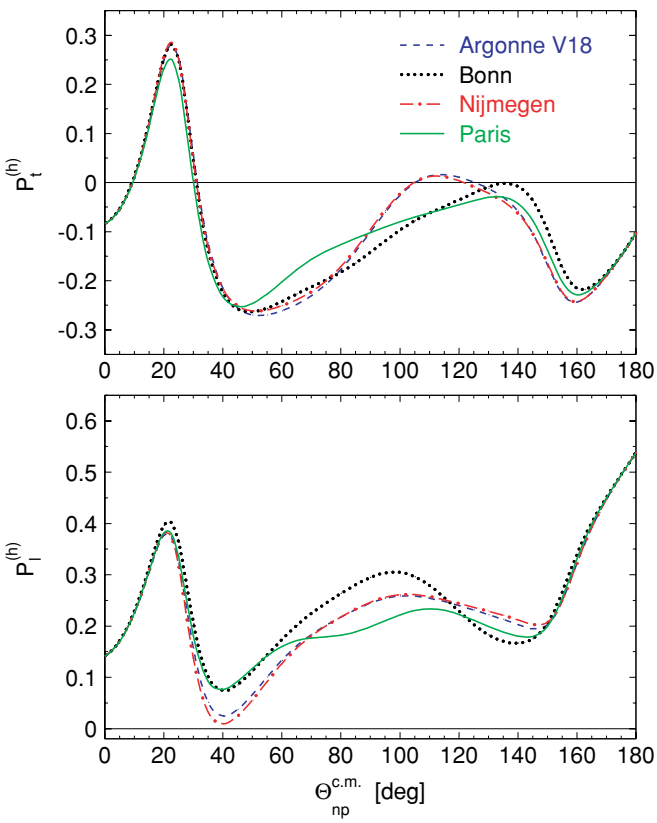

FIG. 33. (Color online) Comparison of FSI+MEC+IC+RC calculations of $P_t^{(h)}$ (top panel) and $P_\ell^{(h)}$ (bottom panel) for the Argonne V18, Bonn, Nijmegen, and Paris potentials. The results shown are for the central kinematics of our $Q^2 = 1.136$ (GeV/c)^2 point and $\phi_{np}^{c.m.} = 0^\circ$.

boosts (i.e., γ, $\gamma_n^{c.m.}$, and γ_n all $\sim$1), it is clear that we recover the nonrelativistic result, $\theta_n^W \to \theta_n^{c.m.} - \theta_n$. Also, it is obvious that for perfect quasifree emission (i.e., $\Theta_{np}^{c.m.} = 0$ or π), the recoil polarization components in the n-p c.m. frame are identical to those in the laboratory frame.

APPENDIX B: SENSITIVITY TO NUCLEAR PHYSICS EFFECTS AND DEUTERON STRUCTURE

To demonstrate the sensitivity of $P_t^{(h)}$ to the value of G_{En} and the insensitivity of $P_t^{(h)}$ and $P_\ell^{(h)}$ to FSI, MEC, IC, and the choice of the *NN* potential, we present several examples of ^{2}H$(\vec{e}, e'\vec{n})^1$H recoil polarization calculations performed within the PWBA and FSI+MEC+IC+RC models of Arenhövel *et al.* [19,20,120] in Figs. 31, 32, and 33. We have (arbitrarily) chosen to show examples of these calculations for the central kinematics of our $Q^2 = 1.136$ (GeV/c)^2 point (i.e., $E_e = 2.326$ GeV, $E_{e'} = 1.718$ GeV, $\theta_{e'} = 30.93^\circ$).

First, FSI+MEC+IC+RC calculations of $P_t^{(h)}$ are shown in Fig. 31 as a function of $\Theta_{np}^{c.m.}$ for three values of G_{En} scaled by the Galster parametrization: 0.5, 1.0, and 1.5. A strong (nearly linear) sensitivity of $P_t^{(h)}$ to the value of G_{En} is seen at and near quasifree emission. Second, the insensitivity of $P_t^{(h)}$ and $P_\ell^{(h)}$ to FSI, MEC, and IC for quasifree emission is shown in Fig. 32, where little difference between the PWBA and FSI+MEC+IC+RC calculations is observed at and near quasifree emission. Finally, we compare FSI+MEC+IC+RC calculations of $P_t^{(h)}$ and $P_\ell^{(h)}$ for the Argonne V18 [121], Bonn [74], Nijmegen [122], and Paris [123] NN potentials in Fig. 33. Again, at and near quasifree emission, there is little model dependence.

[1] D. R. Yennie, M. M. Lévy, and D. G. Ravenhall, Rev. Mod. Phys. **29**, 144 (1957); F. J. Ernst, R. G. Sachs, and K. C. Wali, Phys. Rev. **119**, 1105 (1960); R. G. Sachs, *ibid.* **126**, 2256 (1962); L. N. Hand, D. G. Miller, and R. Wilson, Rev. Mod. Phys. **35**, 335 (1963).
[2] S. Frullani and J. Mougey, Adv. Nucl. Phys. **14**, 1 (1984).
[3] D. Drechsel and M. M. Giannini, Rep. Prog. Phys. **52**, 1083 (1989).
[4] I. Sick, Prog. Part. Nucl. Phys. **47**, 245 (2001).
[5] A. W. Thomas and W. Weise, *The Structure of the Nucleon* (Wiley-VCH, Berlin, 2001).
[6] H. Gao, Int. J. Mod. Phys. E **12**, 1 (2003); **12**, 567 (2003).
[7] C. E. Hyde-Wright and K. de Jager, Annu. Rev. Nucl. Part. Sci. **54**, 217 (2004).
[8] A. Lung *et al.*, Phys. Rev. Lett. **70**, 718 (1993).
[9] S. Platchkov *et al.*, Nucl. Phys. **A510**, 740 (1990).
[10] R. Schiavilla and I. Sick, Phys. Rev. C **64**, 041002(R) (2001).
[11] R. Madey and T. Eden, Fizika B (Zagreb) **8**, 35 (1999); Jefferson Laboratory experiment 93-038, R. Madey and S. Kowalski, spokespersons.
[12] R. Madey *et al.*, Phys. Rev. Lett. **91**, 122002 (2003).
[13] B. Plaster, Ph.D. thesis, Massachusetts Institute of Technology (2003); S. Tajima, Ph.D. thesis, Duke University (2003); W. Tireman, Ph.D. thesis, Kent State University (2003); G. MacLachlan, Ph.D. thesis, Ohio University (2004); A. Aghalaryan, Ph.D. thesis, Yerevan Physics Institute (in preparation); E. Crouse, Ph.D. thesis, The College of William and Mary (in preparation).
[14] A. I. Akhiezer, L. N. Rozentsveig, and I. M. Shmushkevich, Sov. Phys. JETP **6**, 588 (1958).
[15] N. Dombey, Rev. Mod. Phys. **41**, 236 (1969).
[16] A. I. Akhiezer and M. P. Rekalo, Sov. J. Part. Nuclei **4**, 277 (1974).
[17] R. G. Arnold, C. E. Carlson, and F. Gross, Phys. Rev. C **23**, 363 (1981).
[18] M. Ostrick *et al.*, Phys. Rev. Lett. **83**, 276 (1999).
[19] H. Arenhövel, Phys. Lett. **B199**, 13 (1987).
[20] H. Arenhövel, W. Leidemann, and E. L. Tomusiak, Z. Phys. A **331**, 123 (1988); **334**, 363 (1989).
[21] M. P. Rekalo, G. I. Gakh, and A. P. Rekalo, J. Phys. G **15**, 1223 (1989).
[22] J. M. Laget, Phys. Lett. **B273**, 367 (1991).
[23] C. Herberg *et al.*, Eur. Phys. J. A **5**, 131 (1999).
[24] T. W. Donnelly and A. S. Raskin, Ann. Phys. **169**, 247 (1986); A. S. Raskin and T. W. Donnelly, *ibid.* **191**, 78 (1989).
[25] C. Y. Cheung and R. M. Woloshyn, Phys. Lett. **B127**, 147 (1983).
[26] E. L. Tomusiak and H. Arenhövel, Phys. Lett. **B206**, 187 (1988).

[27] H. Arenhövel, W. Leidemann, and E. L. Tomusiak, Phys. Rev. C **46**, 455 (1992); **52**, 1232 (1995).
[28] W. Leidemann, E. L. Tomusiak, and H. Arenhövel, Phys. Rev. C **43**, 1022 (1991).
[29] B. Blankleider and R. M. Woloshyn, Phys. Rev. C **29**, 538 (1984).
[30] C. Ciofi degli Atti, E. Pace, and G. Salmè, Phys. Rev. C **46**, R1591 (1992).
[31] R.-W. Schulze and P. U. Sauer, Phys. Rev. C **48**, 38 (1993).
[32] C. E. Jones-Woodward *et al*., Phys. Rev. C **44**, R571 (1991).
[33] A. K. Thompson *et al*., Phys. Rev. Lett. **68**, 2901 (1992).
[34] T. Eden *et al*., Phys. Rev. C **50**, R1749 (1994).
[35] P. Markowitz *et al*., Phys. Rev. C **48**, R5 (1993).
[36] H. Gao *et al*., Phys. Rev. C **50**, R546 (1994); H. Gao, Nucl. Phys. **A631**, 170c (1998).
[37] S. Galster *et al*., Nucl. Phys. **B32**, 221 (1971).
[38] M. Meyerhoff *et al*., Phys. Lett. **B327**, 201 (1994).
[39] J. Becker *et al*., Eur. Phys. J. A **6**, 329 (1999).
[40] J. Golak, G. Ziemer, H. Kamada, H. Witala, W. Glockle, Phys. Rev. C **63**, 034006 (2001).
[41] I. Passchier *et al*., Phys. Rev. Lett. **82**, 4988 (1999).
[42] D. Rohe *et al*., Phys. Rev. Lett. **83**, 4257 (1999).
[43] J. Bermuth *et al*., Phys. Lett. **B564**, 199 (2003).
[44] G. Kubon *et al*., Phys. Lett. **B524**, 26 (2002).
[45] J. Golak, W. Glockle, H. Kamada, H. Witala, R. Skibinski, A. Nogga, Phys. Rev. C **65**, 044002 (2002).
[46] W. Xu *et al*., Phys. Rev. Lett. **85**, 2900 (2000); W. Xu *et al*., Phys. Rev. C **67**, 012201(R) (2003).
[47] G. Höhler *et al*., Nucl. Phys. **B114**, 505 (1976).
[48] H. Zhu *et al*., Phys. Rev. Lett. **87**, 081801 (2001).
[49] J. J. Kelly, Phys. Rev. C **66**, 065203 (2002).
[50] G. Warren *et al*., Phys. Rev. Lett. **92**, 042301 (2004).
[51] D. I. Glazier *et al*., Eur. Phys. J. A **24**, 101 (2005).
[52] J. Friedrich and Th. Walcher, Eur. Phys. J. A **17**, 607 (2003).
[53] C. W. Leemann, D. R. Douglas, and G. A. Krafft, Annu. Rev. Nucl. Part. Sci. **51**, 413 (2001).
[54] R. Madey, A. Lai, and T. Eden, AIP Conf. Proc. **339**, 47 (1995); I. Niculescu *et al*., IEEE Trans. Nucl. Sci. **45**, 68 (1998); A. Yu. Semenov *et al*., Nucl. Instrum. Methods Phys. Res. A **557**, 585 (2006).
[55] M. Poelker *et al*., AIP Conf. Proc. **570**, 943 (2001).
[56] M. Poelker and J. Hansknecht, *Proceedings of the IEEE Particle Accelerator Conference (PAC 2001)*, 95 (2001).
[57] C. Yan *et al*., Nucl. Instrum. Methods Phys. Res. A **365**, 261 (1995).
[58] M. Hauger *et al*., Nucl. Instrum. Methods Phys. Res. A **462**, 382 (2001).
[59] J. Alcorn *et al*., Nucl. Instrum. Methods Phys. Res. A **522**, 294 (2004).
[60] C. Yan *et al*., Nucl. Instrum. Methods Phys. Res. A **365**, 46 (1995); R. Wojcik and C. Yan, *ibid*. **484**, 690 (2002).
[61] O. K. Baker *et al*., Nucl. Instrum. Methods Phys. Res. A **367**, 92 (1995).
[62] L. Wolfenstein, Phys. Rev. **75**, 1664 (1949); **85**, 947 (1952).
[63] J. Simkin and C. W. Trowbridge, Rutherford Laboratory Report 79-097 (unpublished).
[64] S. Taylor, E93-038 technical reports (unpublished): http://www.jlab.org/∼plaster/reports/charybdis1.ps; http:www.jlab.org/∼plaster/reports/charybdis2.ps; http:www.jlab.org/∼plaster/reports/charybdis3.ps.
[65] R. Madey *et al*., Nucl. Instrum. Methods Phys. Res. **214**, 401 (1983).
[66] J. W. Watson *et al*., Nucl. Instrum. Methods Phys. Res. A **272**, 750 (1988); R. Madey *et al*., IEEE Trans. Nucl. Sci. **36**, 231 (1989); T. Eden *et al*., Nucl. Instrum. Methods Phys. Res. A **338**, 432 (1994).
[67] http://coda.jlab.org
[68] J. Arrington, Ph.D. thesis, California Institute of Technology (1998).
[69] R. Madey *et al*., Nucl. Instrum. Methods Phys. Res. **151**, 445 (1978).
[70] R. A. Arndt, I. I. Strakovsky, and R. L. Workman, Int. J. Mod. Phys. A **18**, 449 (2003).
[71] G. G. Ohlsen and P. W. Keaton Jr., Nucl. Instrum. Methods Phys. Res. **109**, 41 (1973).
[72] D. L. Prout *et al*., Phys. Rev. C **63**, 014603 (2000).
[73] J. Arrington, SIMC computer code, http://www.jlab.org/∼johna/SIMC_documents/simc.ps.
[74] R. Machleidt, K. Holinde, and Ch. Elster, Phys. Rep. **149**, 1 (1987).
[75] R. W. Finlay, W. P. Abfalterer, G. Fink, E. Montei, T. Adami, P. W. Lisowski, G. L. Morgan, and R. C. Haight, Phys. Rev. C **47**, 237 (1993).
[76] R. A. Cecil, B. D. Anderson, and R. Madey, Nucl. Instrum. Methods Phys. Res. **161**, 439 (1979).
[77] S. Kopecky, P. Riehs, J. A. Harvey, and N. W. Hill, Phys. Rev. Lett. **74**, 2427 (1995); S. Kopecky, J. A. Harvey, N. W. Hill, M. Krenn, M. Pernicka, P. Riehs, and S. Steiner, Phys. Rev. C **56**, 2229 (1997).
[78] J. J. Kelly, Phys. Rev. C **70**, 068202 (2004).
[79] E. J. Brash, A. Kozlov, Sh. Li, and G. M. Huber, Phys. Rev. C **65**, 051001(R) (2002).
[80] A. Afanasev, I. Akushevich, and N. Merenkov, Phys. Rev. D **64**, 113009 (2001).
[81] G. G. Simon, C. Schmitt, F. Borkowski, and V. H. Walther, Nucl. Phys. **A333**, 381 (1980).
[82] L. E. Price *et al*., Phys. Rev. D **4**, 45 (1971).
[83] M. K. Jones *et al*., Phys. Rev. Lett. **84**, 1398 (2000); O. Gayou *et al*., Phys. Rev. C **64**, 038202 (2001); V. Punjabi *et al*., *ibid*. **71**, 055202 (2005).
[84] O. Gayou *et al*., Phys. Rev. Lett. **88**, 092301 (2002).
[85] T. Pospischil *et al*., Eur. Phys. J. A **12**, 125 (2001).
[86] B. D. Milbrath *et al*., Phys. Rev. Lett. **82**, 2221 (1999).
[87] H. Anklin *et al*., Phys. Lett. **B336**, 313 (1994).
[88] H. Anklin *et al*., Phys. Lett. **B428**, 248 (1998).
[89] F. Iachello, A. D. Jackson, and A. Lande, Phys. Lett. **B43**, 191 (1973).
[90] M. F. Gari and W. Krümpelmann, Z. Phys. A **322**, 689 (1985).
[91] M. F. Gari and W. Krümpelmann, Phys. Lett. **B274**, 159 (1992).
[92] R. Bijker and F. Iachello, Phys. Rev. C **69**, 068201 (2004).
[93] E. L. Lomon, Phys. Rev. C **64**, 035204 (2001).
[94] E. L. Lomon, Phys. Rev. C **66**, 045501 (2002).
[95] Jefferson Laboratory experiment 02-013, G. Cates, K. McCormick, B. Reitz, and B. Wojtsekhowski, spokespersons.
[96] Jefferson Laboratory experiment 04-110, B. Anderson, J. Kelly, S. Kowalski, R. Madey, and A. Semenov, spokespersons.
[97] D. H. Lu, A. W. Thomas, and A. G. Williams, Phys. Rev. C **57**, 2628 (1998).
[98] A. L. Licht and A. Pagnamenta, Phys. Rev. D **2**, 1150 (1970).
[99] D. H. Lu, K. Tsushima, A. W. Thomas, and A. G. Williams, Nucl. Phys. **A634**, 443 (1998).
[100] D. H. Lu, K. Tsushima, A. W. Thomas, A. G. Williams, and K. Saito, Phys. Rev. C **60**, 068201 (1999).

[101] S. Dieterich *et al*., Phys. Lett. **B500**, 47 (2001).
[102] S. Strauch *et al*., Phys. Rev. Lett. **91**, 052301 (2003).
[103] G. A. Miller and M. R. Frank, Phys. Rev. C **65**, 065205 (2002); G. A. Miller, *ibid*. **66**, 032201(R) (2002).
[104] M. R. Frank, B. K. Jennings, and G. A. Miller, Phys. Rev. C **54**, 920 (1996).
[105] B. Kubis and U.-G. Meissner, Nucl. Phys. **A679**, 698 (2001).
[106] T. Fuchs, J. Gegelia, and S. Scherer, J. Phys. G **30**, 1407 (2004).
[107] M. R. Schindler, J. Gegelia, and S. Scherer, Nucl. Phys. **B682**, 367 (2004).
[108] H.-W. Hammer, D. Drechsel, and U.-G. Meissner, Phys. Lett. **B586**, 291 (2004).
[109] M. R. Schindler, J. Gegelia, and S. Scherer, Eur. Phys. J. A **26**, 1 (2005).
[110] M. M. Kaskulov and P. Grabmayr, Phys. Rev. C **69**, 028201 (2004); Eur. Phys. J. A **19**, 157 (2004).
[111] R. F. Wagenbrunn, S. Boffi, W. Klink, W. Plessas, and M. Radici, Phys. Lett. **B511**, 33 (2001); S. Boffi, L. Ya. Glozman, W. Klink, W. Plessas, M. Radici, and R. F. Wagenbrunn, Eur. Phys. J. A **14**, 17 (2002).
[112] S. Simula, arXiv:nucl-th/0105024.
[113] F. Cardarelli, E. Pace, G. Salmè, and S. Simula, Phys. Lett. **B357**, 267 (1995).
[114] M. De Sanctis, M. M. Giannini, E. Santopinto, and A. Vassallo, arXiv:nucl-th/0506033.
[115] M. Göckeler, T. R. Hemmert, R. Horseley, D. Pleiter, P. E. L. Rakow, A. Schafer, and G. Schierholz, Phys. Rev. D **71**, 034508 (2005).
[116] J. D. Ashley, D. B. Leinweber, A. W. Thomas, and R. D. Young, Eur. Phys. J. A **19**, 9 (2004).
[117] H. H. Matevosyan, G. A. Miller, and A. W. Thomas, Phys. Rev. C **71**, 055204 (2005).
[118] H. Arenhövel, W. Leidemann, and E. L. Tomusiak, Eur. Phys. J. A **23**, 147 (2005).
[119] D. R. Giebink, Phys. Rev. C **32**, 502 (1985).
[120] H. Arenhövel, private communication (2001, 2002, 2003).
[121] R. B. Wiringa, V. G. J. Stoks, and R. Schiavilla, Phys. Rev. C **51**, 38 (1995).
[122] M. M. Nagels, T. A. Rijken, and J. J. de Swart, Phys. Rev. D **17**, 768 (1978).
[123] M. Lacombe *et al*., Phys. Lett. **B101**, 139 (1981).